CHEMICALLY INDUCED GRAIN BOUNDARY MIGRATION IN ALLOY SYSTEMS

By

© KELVIN M. TASHIRO

A Thesis

Submitted to the School of Graduate Studies

in partial fulfilment of the requirements

for the Degree

Doctor of Philosophy

McMaster University

Oct 1986

CHEMICALLY INDUCED GRAIN BOUNDARY MIGRATION

Dedicated to my Wife

DOCTOR OF PHILOSOPHY (1986)
(MATERIAL SCIENCE)

McMASTER UNIVERSITY
Hamilton, Ontario

TITLE: Chemically Induced Grain Boundary Migration in Alloy Systems

AUTHOR: Kelvin M. Tashiro, B.Sc. (McMaster University 1981)

SUPERVISOR: Dr. G. R. Purdy

NUMBER OF PAGES: xix, 214

ABSTRACT

This thesis describes the phenomenon of chemically induced grain boundary migration, a process in which a grain boundary migrates in response to a chemical driving force. The migration characteristics from various binary alloy systems are documented, especially in the aluminum-zinc system where extensive measurements have been made in both static and dynamic situations. The dynamics of chemically induced grain boundary migration ARE also studied in conjunction with the growth of a second phase, a situation referred to as discontinuous precipitation.

It is suggested that the force which is responsible for moving the boundary reveals different facets of itself for different cases. The facets are extremes in the chemical force levels; one is at a low level and is suggested to be derived from coherency strains when solute penetration into the bulk is significant. The other force is a high level force and which originates from large concentration differences which exist across the boundary at low volume penetration levels. It is uncertain whether the transition between the two chemical driving force levels is continuous or discontinuous since the transition ranges are small.

Elastic anisotropy is suggested to be responsible for the initiation of migration due to an unbalanced coherent strain energy present across the boundary. The migration process has been modelled

macroscopically and computer simulated. At this time, current models of grain boundary structure are suggested to be inadequate to account for the coupling of a chemical force to grain boundary structural components.

ACKNOWLEDGEMENTS

The author is indebted to his supervisor, Dr. G. R. Purdy for his suggestions into the research topic studied here, his guidance and encouragement throughout the course of this work. A sincere note of gratitude is extended to Dr. J. A. Morrison and Dr. W. W. Smeltzer for serving on the Ph.D. supervisory committee.

Thanks are extended to the technical staff of both the Metallurgy Department and the Institute of Materials Research for their assistance during the course of this work.

The Natural Sciences and Engineering Research Council of Canada is gratefully acknowledged for their financial support of the research topic and the author.

CHEMICALLY INDUCED GRAIN BOUNDARY MIGRATION

(CIGM)

TABLE OF CONTENTS

LIST OF ILLUSTRATIONS

Figure

Figure

Figure

CHAPTER 1

INTRODUCTION AND SCOPE

Chemically induced grain boundary migration (CIGM) is a solid state phase transformation which possesses its own unique set of characteristics. The migrating boundary results in the growth of one crystal at the expense of another. Fast solute diffusion along the grain boundary is also a necessary requirement of the process. As the boundary migrates, the growing grain exhibits a compositional change. Using these basic characteristics as a definition, then a similiar process can be found in discontinuous precipitation. Such a phenomenon exists between the supersaturated alpha matrix and the solute depleted alpha phase of the discontinuous product.

The present knowledge of boundary structure and behavior is reviewed in order to determine whether the existing knowledge base concerning the possible processes at a moving boundary is developed sufficiently to model these interfacially controlled transformations adequately. In particular, one adds the question: How is the chemical force coupled to the structural components within the grain boundary which are responsible for migration?

The present work is intended to examine CIGM in detail in a number of systems but mainly in the aluminum-zinc system and to consider the importance of a chemical driving force in driving solid state phase transformations such as CIGM and the alpha interface in discontinuous

precipitation. Various sinks for the chemical energy are considered such as capillarity and elastic energy. The importance of elastic anisotropy is also considered; it is suggested that elastic anisotropy is responsible for the initiation of boundary migration.

CHAPTER 2

LITERATURE REVIEW

A comprehensive review of a number of subject areas is required in order to realise fully the complex situation created by the migration of a grain boundary, especially when accompanied by diffusion along the grain boundary.

2.1.1 Grain Boundary Structure

A grain boundary is a complex feature whose possible structure has been the subject of study by many investigators (A1,A2,A3,A4,A5,A6,A7,A8,A9,A11). The formal review of these possible structures must begin by reviewing the geometrical concepts that are employed in this field of study.

2.1.1.1 Geometric Aspects

In order to simplify the geometry of the situation, the following assumptions are made: (1) The boundary is planar; (2) The two crystals forming the boundary are identical, perfect and elastically strained only at the boundary. The layer of atoms which comprise the boundary is known as the core layer and this layer possesses its own unique geometry. The geometrical constructs used to describe the core layer are <A> the Coincidence Site Lattice (CSL), <B> Bollman's O-Lattice and <C> the Displace-Shift-Complete Lattice (DSC Lattice). These constructs do not allow atoms to relax near their positions (They

are therefore "rigid atom" descriptions).

<A> Coincidence Site Lattice

This lattice is used to describe the basic symmetry of the core layer. The lattice is produced in the following manner; Allow two crystal lattices to interpenetrate with a specific misorientation. By a small translation vector allow one lattice point to be coincident in both lattices. This procedure will bring other lattice points into coincidence forming a larger three dimensional lattice known as the coincidence site lattice as shown in Figure 2.1. The quantity Σ describes the number of atoms related to the coincidence site. Thus, if $\Sigma = 1$, then the coincidence sites would match the lattice sites. The boundary plane can then be placed into the interpenetrating lattices and the redundant lattice sites from each crystal can be removed. Usually when using this construct, the boundary plane passes through a number of CSL points which results in one atom site of good atomic fit between both lattices; therefore, the boundary would possess a periodic structure. Only a few special misorientations between the crystals do yield perfect coincidence site lattices, therefore, the CSL spacing is discontinuous with respect to misorientation.

<B> Bollman's O-Lattice

Bollman (A41) realised that atom sites are not the only sites which possess symmetry. Interior cell sites may also act as coincidence sites; therefore, the O-lattice describes the sites of best matching. The method of construction as shown in Figure 2.2 is identical to the CSL contruct. The O-lattice construction possesses certain interesting geometric properties. Firstly, a grain boundary plane passing through

O-lattice sites contains a periodic structure but at the stated CSL periodicity and not the O-lattice periodicity. Secondly, whereas the CSL spacing is discontinuous with misorientation, the O-lattice is continuous. Thirdly, each O-lattice site can be used as a site for further rotation to a different lattice. Therefore, each O-lattice site is an "origin" for other rotational transformations.

<c> DSC Lattice

Consider a set of vectors which describes displacements for two interpenetrating lattices with respect to each other. The pattern produced by both lattices is conserved when any lattice is displaced by any of the vectors from the original displacement set. These vectors form a lattice as shown in Figure 2.3 and is known as the DSC lattice. The boundary plane is produced by the method given by the CSL method. It can be seen in the figure that as the CSL spacing increases, the DSC lattice vectors decrease. Such a set of vectors are of considerable importance as they can describe the possible displacements within the boundary and yet maintain the original boundary structure, a necessary requirement for the Burgers vector of grain boundary dislocations.

2.1.1.2 Dislocation Model of Grain Boundary Structure

An array of discrete lattice dislocations has been established as the description for a low angle grain boundary as shown in Figure 2.4. The spacing between the dislocations d is related to the misorientation angle (a) and the Burgers vector (b) by:

$$d = b/2 \text{ Sin } (a/2) \qquad (2.1)$$

The energy of a low angle boundary of this form is a combination of the strain energy of the dislocation array and the individual dislocation

core energies. The actual value of the core energies is difficult to estimate accurately, leading to a finite error in the energies of low angle boundaries. As the misorientation angle increases, the external strain field decreases and the core energies dominate the boundary energy.

The lattice dislocations that comprise a low angle boundary are referred to as primary dislocations and the process by which they form their array is known as primary relaxation. As the misorientation increases, the spacing between the lattice dislocations decreases to the point where their cores overlap as shown in Figure 2.5. The dislocations at high misorientations do not resemble their parent lattice counterparts as the structure now resembles dislocation cores only and long range stress fields do not exist. The periodicity of the boundary still exists as indicated by diffraction from boundaries with high misorientations.

As stated previously, there are certain misorientations and boundary plane orientations which represent high coincidence across the boundaries. These CSL orientations possess relatively short periodicities and low energy. Therefore, at small deviations from the CSL orientation, the boundary energetically favours the low energy CSL structure. The deviation from the CSL orientation is accommodated by a network of grain boundary dislocations. This process is known as secondary relaxation and the dislocations are referred to as a secondary dislocation array. The dislocations possess a long range stress field and can be observed easily as shown in Figure 2.6.

Since boundary structure knowledge is heavily dependent upon a

knowledge of the core structure, many investigators have modelled the core structure through computer simulations. For a given misorientation, the lattices are brought together usually at a CSL orientation. The atoms in the core region are allowed to relax to their minimum energy configuration. A rigid body translation may be required in order to minimise the energy. The relaxed core structure is calculated by the method of molecular statics by such investigators as Vitek et. al. (A7,A31,A34,A35,A39) and Weins (A30) and by Monte Carlo methods by Chang (A33). The atoms are assumed to interact by any one of a number of pairwise potentials such as the Morse, Born-Mayer, psuedo or any other empirical potential. The final atom positions which represent the minimum energy for the boundary are calculated. The energy minimised is the potential energy only, no kinetic energy is present, therefore such calculations represent the boundary state at 0 K. Realistic boundary structures are thought to be produced despite the number of assumptions made.

The general results produced by all molecular static calculations are: The boundary is generally narrow, only a few atoms thick. The density of atoms in the core structure is generally large, less dense configurations are possible but possess higher energy as shown in Figure 2.7. The number of nearest neighbours of atoms in the boundary core is only slightly less than in the lattice. It is suggested that this is a result of the hard sphere behaviour of atoms at small separations. Calculations of boundaries which possess small deviations from CSL orientations predict structures which are observed experimentally. Calculations also predict that small deviations from CSL

orientations are accommodated by an array of boundary dislocations with the area between these dislocations having the CSL structure. Other molecular static calculations also predict the dissociation of lattice type dislocations in very small angle boundaries into partial dislocations with a stacking fault between them.

The calculations (A32) also indicate that high coincidence tilt boundaries consist of a uniform array of a single type of structural units. Such units as shown in Figure 2.7 are simple geometrical solids eg. tetrahedra. Boundaries of this form are termed favoured boundaries since they possess a uniform structure, which consists of long arrays of primary boundary dislocations that have no long range stress field. Other boundaries have been shown to consist of a combination of different structural units. It is therefore suggested that all boundaries possess some form of order. By determining the lowest energy configuration for various boundary orientations, it is possible to construct the variation of boundary energy with orientation as shown in Figure 2.8 for a [001] symmetric tilt boundaries in aluminum.

Another method of determining boundary structure is by molecular dynamics. This method is similiar to molecular static calculations except the atoms are allowed to possess kinetic energy. Therefore, the temperature of the simulation is not 0 K. The results of the calculation are similiar to molecular statics for temperatures well below the melting temperature. Near the melting temperature, boundary structure (A36) appears to be lost by the generation of numerous dislocations in the lattice and the boundary appears to emulate a liquid. Other results of the simulation are; the atoms vibrational frequency is lower than in

the lattice since the atoms are less tightly bound and the vibration is anisotropic, depending upon the atom position within the boundary.

2.1.1.3 Grain Boundary Defects

There are many forms of defects which have been observed or proposed to exist as part of the grain boundary structure. The main defect forms to be considered individually in this discussion are steps or ledges, dislocations and point defects.

Grain Boundary Steps (Ledges)

A pure boundary step lacks any dislocation character, possesses a zero Burgers vector and lacks any long range stress field. An example of a step is shown in Figure 2.9. Generally, not all steps are perfect as a secondary boundary dislocation (which will be considered in the next section) may exist in the riser portion to relieve differences in the misfit between the lattices in each side of the riser as shown in Figure 2.10. Such steps are observable and will therefore, exhibit diffraction contrast in an electron microscope. Steps of opposite misfit across the riser can reduce their elastic energy by combining to form steps which possess extremely large risers. Such steps are known as supersteps and have been observed experimentally.

Grain Boundary Dislocations

Grain boundary dislocations are not constrained to those which are a necessary component of boundary structure. Those dislocations which describe the main portion of boundary structure are referred to as primary boundary dislocations, however, other dislocations exist which are not a necessary part of the structure and which are known as secondary extrinsic dislocations. Secondary extrinsic dislocations can

be considered as perturbations in the network of structure defining primary dislocations. These dislocations are found randomly within the boundary and do not accommodate any crystal misorientation across the boundary in any form. Secondary dislocations can form from the intersection of a lattice dislocation with the boundary as shown in Figure 2.11. The lattice dislocation dissociates into two perfect grain boundary dislocations whose Burgers vectors are basis vectors of the DSC lattice.

The nature of the boundary dislocation depends greatly upon the orientation of its Burgers vector and its core structure. Consider the dislocation core as shown in Figure 2.12, a dislocation can have a step at the core or not depending on the conditions which exist at the boundary plane. Generally, a boundary dislocation will not have a step core, if the volume and area density of the CSL sites are equal. The step at the dislocation core differs from a dislocation at a step as shown in Figure 2.10, as the dislocation in Figure 2.10 is within a step of many atomic dimensions and the step in Figure 2.12 is a fraction of one atomic dimension. The effects of Burgers vector orientation for a 1/3 <310> edge dislocation is shown in Figure 2.13. The two possible extremes for orientation; parallel and perpendicular to the boundary plane are shown. An extra half plane is introduced into the lattice in both situations. The orientation of the half plane is perpendicular to the Burgers vector shown in the diagram.

As shown previously, primary dislocations in low angle tilt boundaries can dissociate to form partial primary dislocations. Secondary dislocations can also dissociate as shown in Figure 2.14. The

dissociation of the edge secondary dislocation is given by (A23):

$$1/3\ [111] = [0.22,0.22,0.22] + [0.11,0.11,0.11] \qquad (2.2)$$

As anticipated, the Burgers vectors of partial secondary dislocations are not part of the basis vectors of the DSC lattice. Partial dislocations have been suggested to exist at the corners of faceted boundaries. Faceted boundaries are boundaries which exhibit large planar areas joined together at corners. They are suggested to exist since the facet represents an extremely low energy configuration for the boundary. This lower energy is sufficient to offset the increase in boundary area.

Grain Boundary Point Defects

The effects of vacancies and interstitials upon grain boundary structure have been observed by electron microscopy (A13,A38) and modelled by molecular statics and dynamics (A17,A19,A37). The modelling procedure generally consisted of forming a perfect boundary and then removing an atom to form a vacancy or replacing it with an impurity atom. The system was then allowed to relax in the usual fashion. The interactions of the defect are considerably more complex since the irregular structure of the boundary makes defining the defect structure difficult. Generally, for vacancies, the vacancy is a vacancy in the core structure for short periodic boundaries and less in long periodic boundaries as shown in Figure 2.15.

Another important feature of boundary structure is that the boundary can act as a ready source and sink for defects. It was suggested by Balluffi (A11) that the secondary boundary dislocations are responsible for this behaviour. In order to be effective defect centres,

the secondary dislocation must exhibit the following:

(1) The dislocations must possess a step core and be sufficient in number.

(2) Relatively high rates of creation or destruction of defects are required.

(3) Fast transport to the defect centres is necessary.

The essential mechanism is the climb of the secondary dislocation by the step core. Secondary dislocation arrays produced by off-coincidence boundaries are also effective as a defect centres. Shown in Figure 2.16 are the atomic shuffles that take place as a secondary dislocation climbs. There is a conversion of crystal 2 material to crystal 1 indicating the boundary is purely migrating since the Burgers vector of the dislocation is perpendicular to the boundary plane. If the Burgers vector were not normal to the plane, then translation of the crystals would occur or boundary sliding. It can be seen that if the Burgers vector was not in the boundary plane, then any movement of a dislocation with a step core would require a net defect flux to it. The nature of the flux depends on the direction of dislocation climb.

This section has briefly reviewed the properties of boundary defects and their complex interactions with each other. The atomistic nature of the defects will now be considered collectively in order to model the macroscopic observations concerning boundary behaviour.

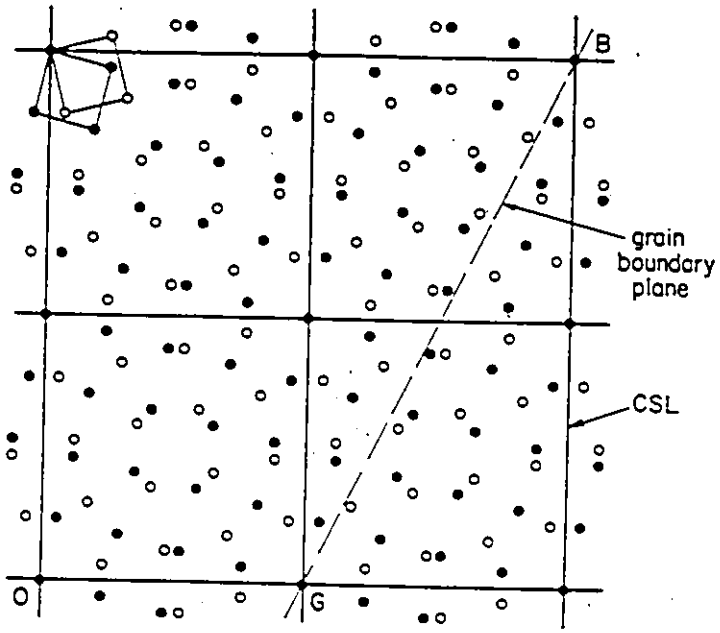

Figure 2.1 Schematic diagram of the coincidence site lattice (CSL) for a [001] twist boundary of 28.1 degrees. The square mesh indicates the CSL points. The dashed line is one possible grain boundary plane. (ref. A2)

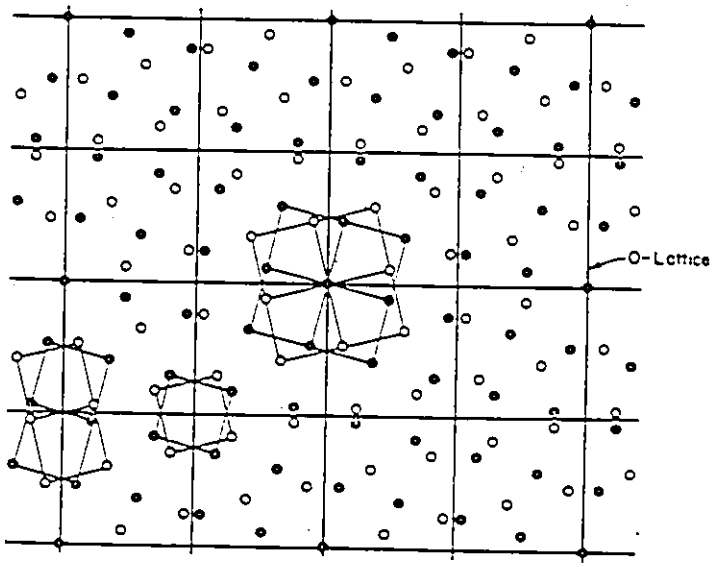

Figure 2.2 Schematic diagram of the Bollman O-Lattice for a [001] twist boundary of 28.1 degrees. The square mesh indicates the O-lattice points. (ref. A2)

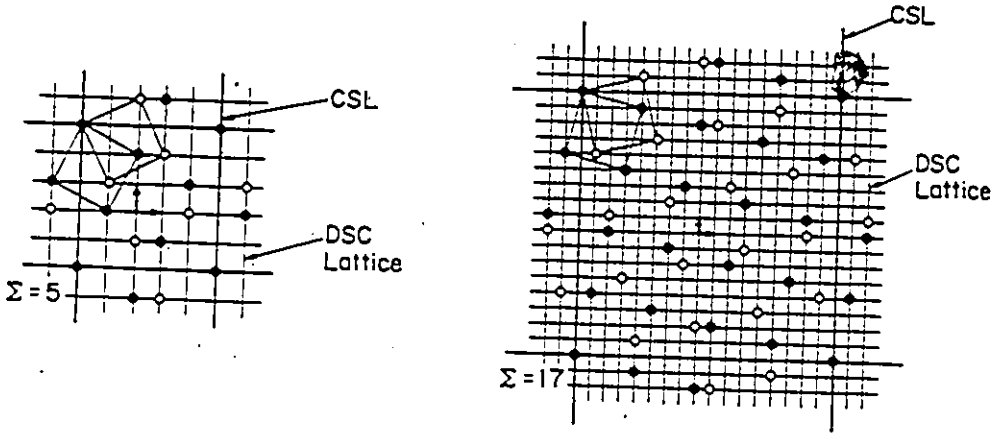

Figure 2.3 Schematic diagram of the Displace - Shift Complete (DSC) lattice for a [001] twist boundary of (a) 36.9 degrees and (b) 28.1 degrees. The smaller square mesh indicates the DSC lattice points in both cases. It can be seen as the CSL points become farther apart, the DSC spacing decreases. (ref. A2)

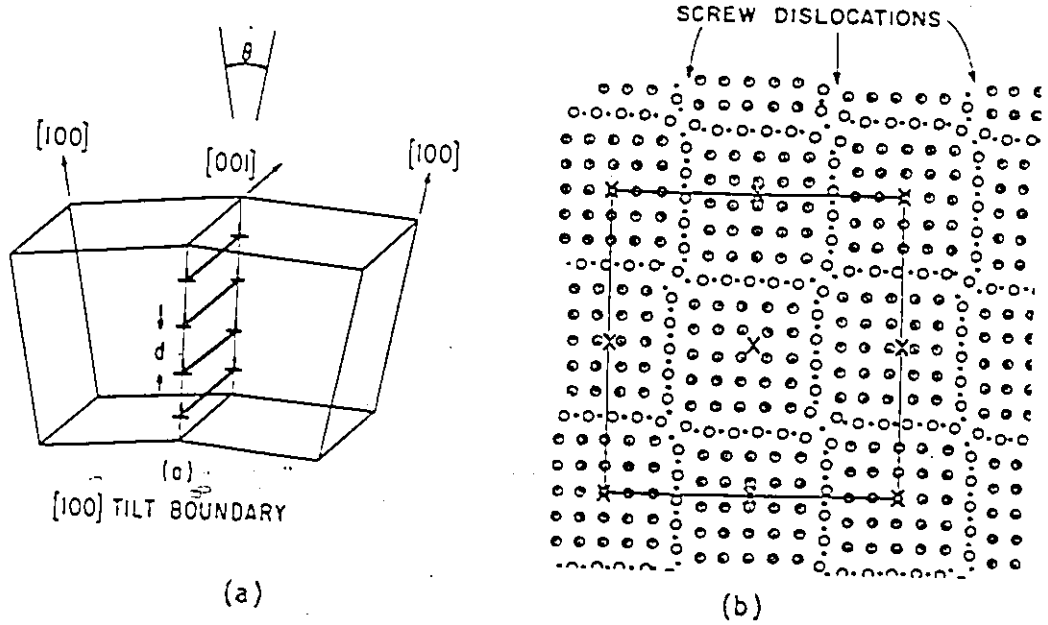

Figure 2.4 Schematic diagram illustrating the use of lattice dislocation arrays to describe low angle angle boundaries. (a) edge dislocations use to describe tilt boundaries (ref. A10) and (b) screw dislocations to to describe twist boundaries. (ref. A6)

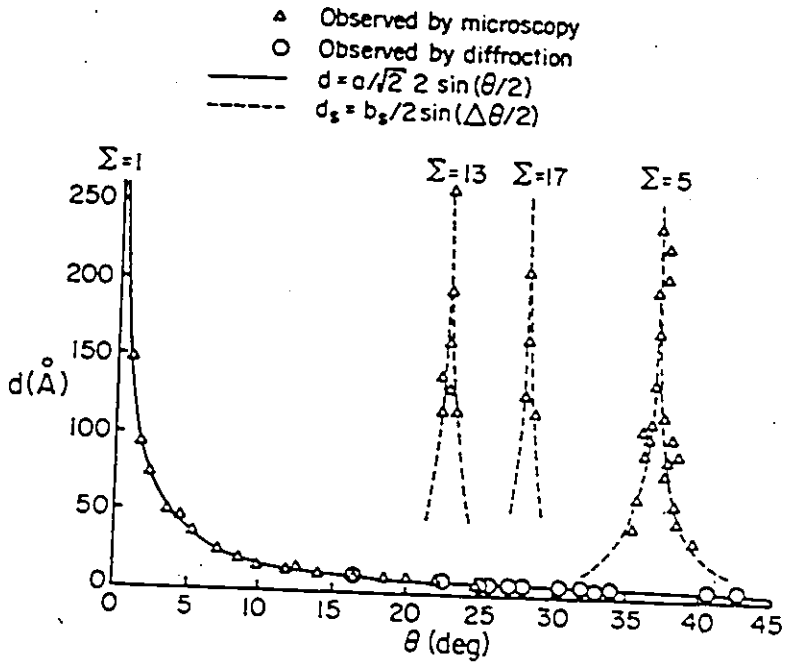

Figure 2.5 Observed primary relaxation spacing d and secondary relaxation d_s for [001] twist boundaries in gold. (ref. A2)

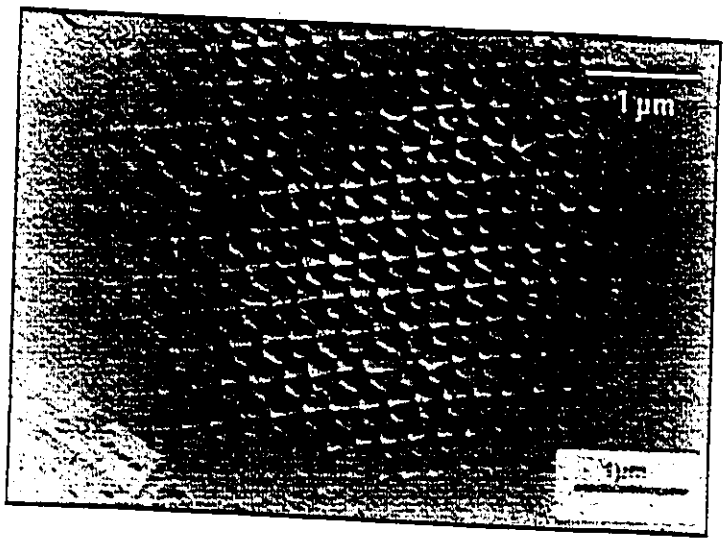

Figure 2.6 Electron micrograph of a secondary dislocation array in Ge. (ref. A4)

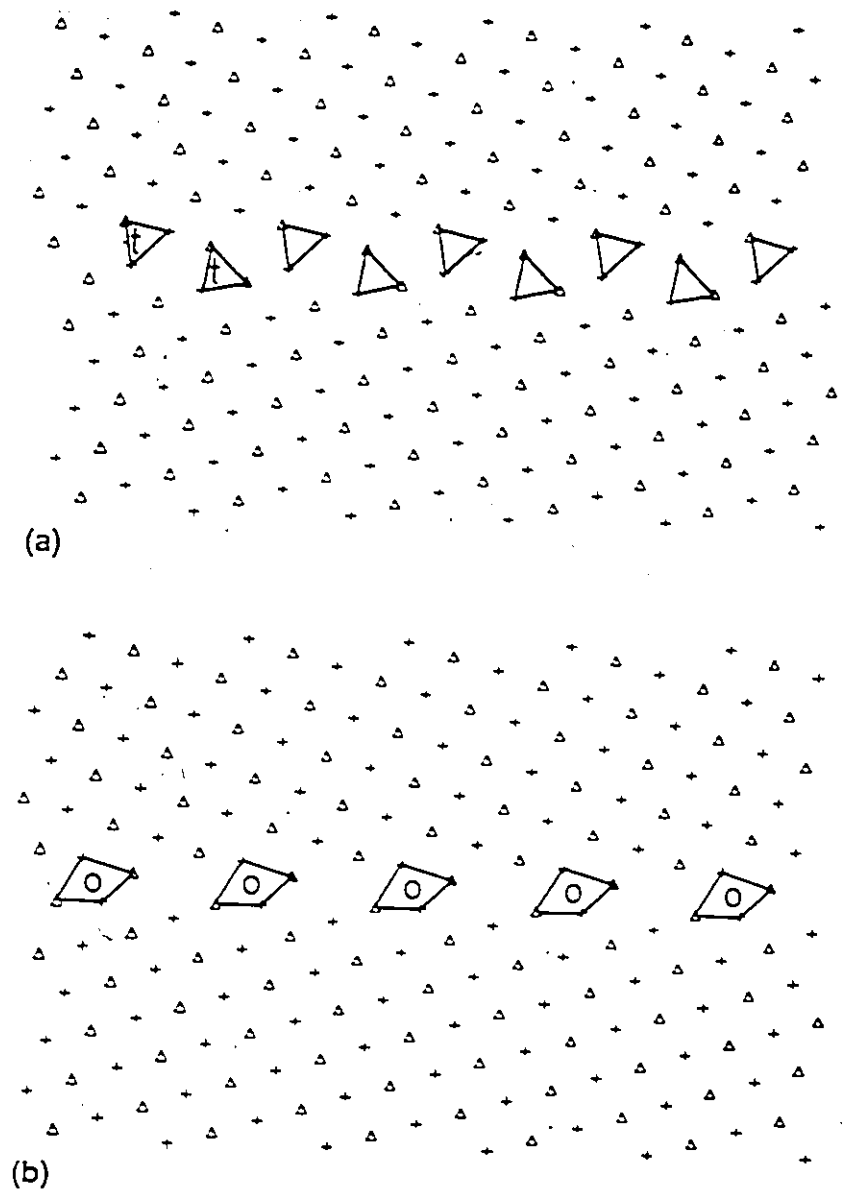

Figure 2.7 Relaxed configuration for a (2,-2,1)/[110] tilt boundary in aluminum. (a) is the lowest energy configuration with main structural components made of tetrahedras, (b) is a higher energy configuration comprised of octahedras, the higher energy configuration appears less dense in the core then the lowest energy configuration. (ref. A7)

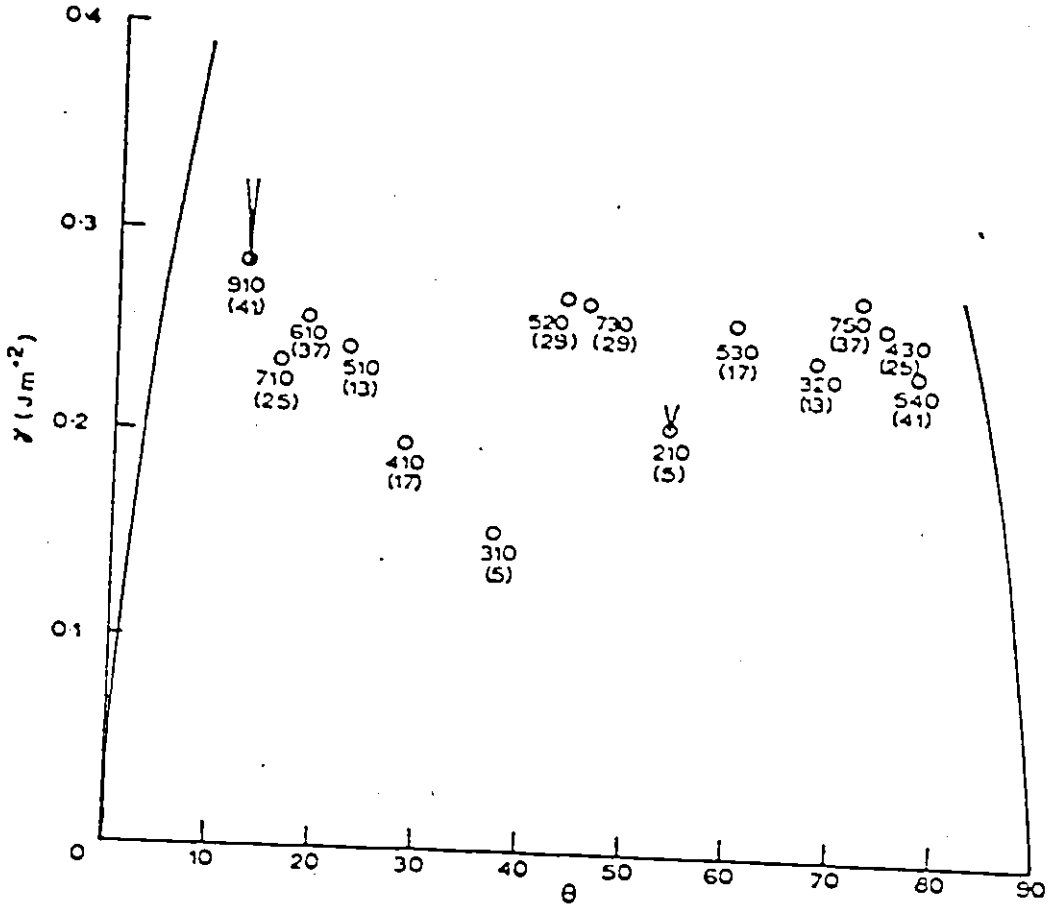

Figure 2.8 Grain boundary energy variation with orientation for a [001] symmetric tilt boundary in aluminum. The energies of low angle boundaries were included to illustrate the maximum possible energies. (ref. A34)

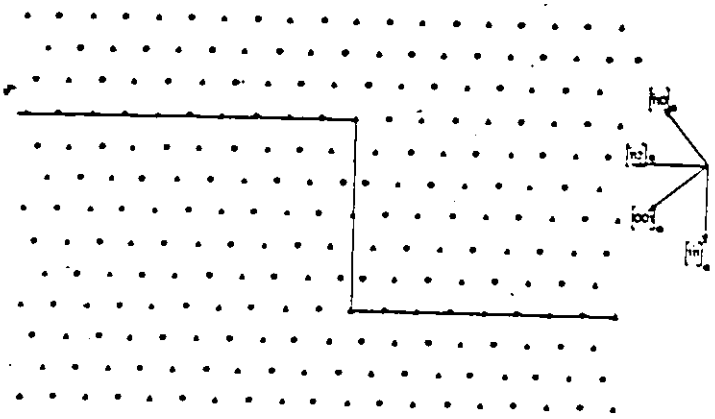

Figure 2.9 A perfect grain boundary step or ledge. The Burgers vector for such a defect is zero and the elastic stress field is zero. (ref. A12)

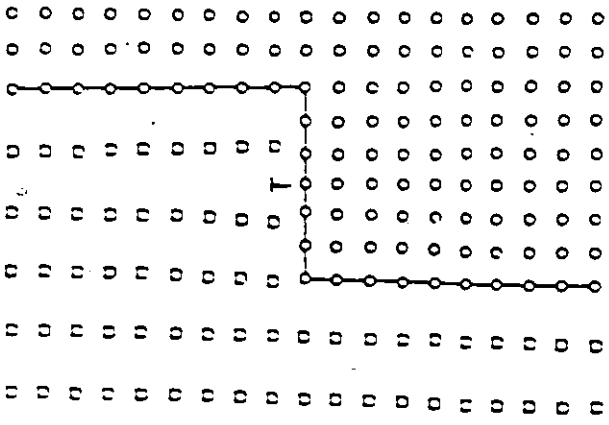

Figure 2.10 An imperfect grain boundary step. A dislocation which is present in the riser portion of the step results in a long range stress field. (ref. A12)

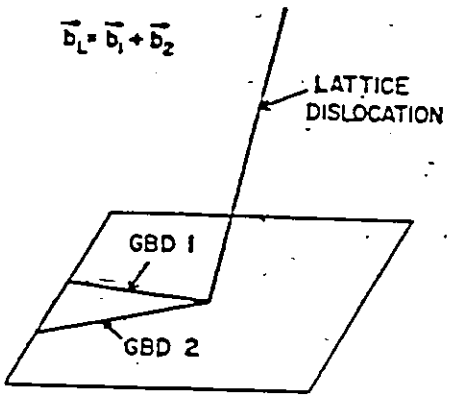

Figure 2.11 Formation of a grain boundary dislocation by the intersection of a lattice dislocation with the boundary. (ref. A15)

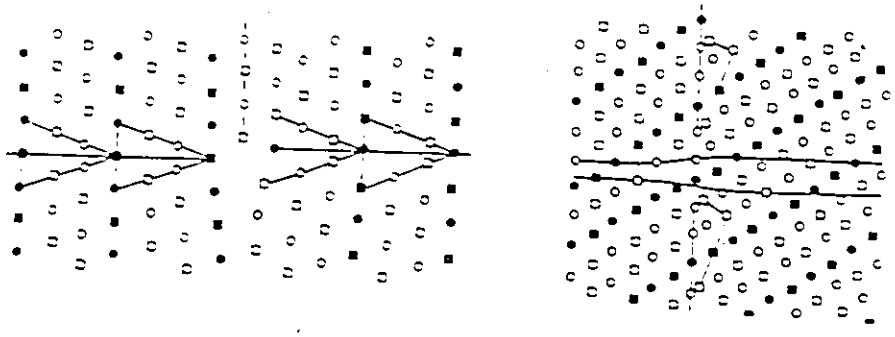

(a) (b)

Figure 2.12 Diagram of the different forms of grain boundary dislocations. (a) is a dislocation with a step core and (b) is a dislocation without a step core. (ref. A12)

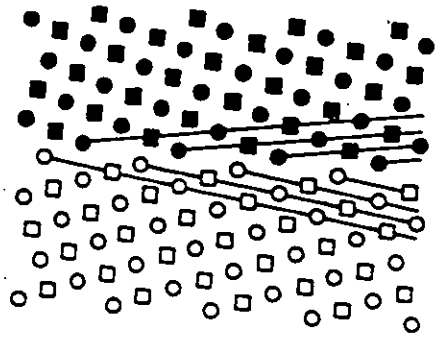

(a)

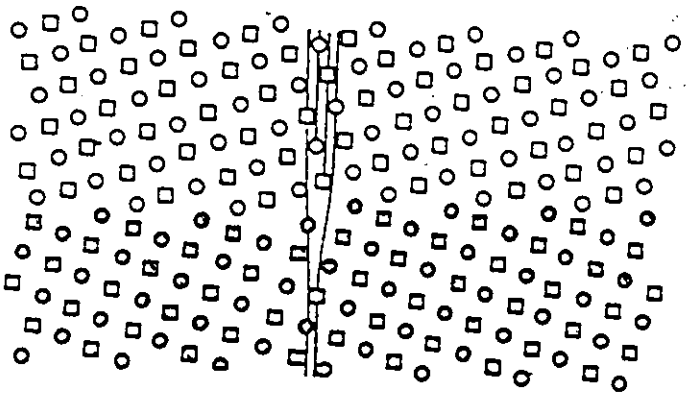

(b)

Figure 2.13 Diagram illustrating the different orientations possible for the Burgers vector of an edge secondary dislocation. (a) has the Burgers vector perpendicular to the boundary plane, b = 1/10 [3,-1,0] (b) has the vector parallel to the plane, b = 1/10 [1,3,0]. A step is associated with the core of this type of dislocation. (ref. A23)

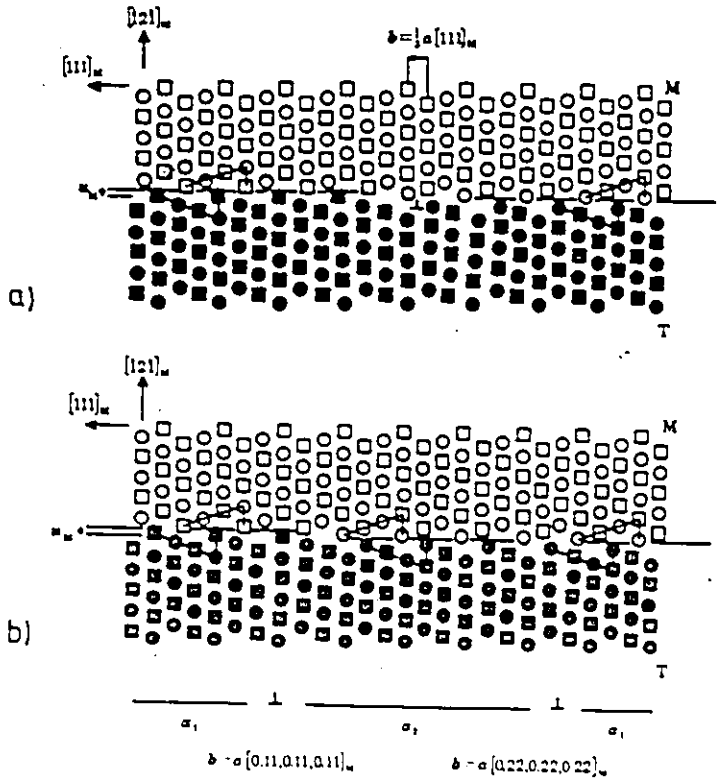

Figure 2.14 The dissociation of a 1/3[111] secondary edge dislocation (a) into two partial dislocations (b). The structure between the partial dislocations a faulted form of the main boundary structure. (ref.. A23)

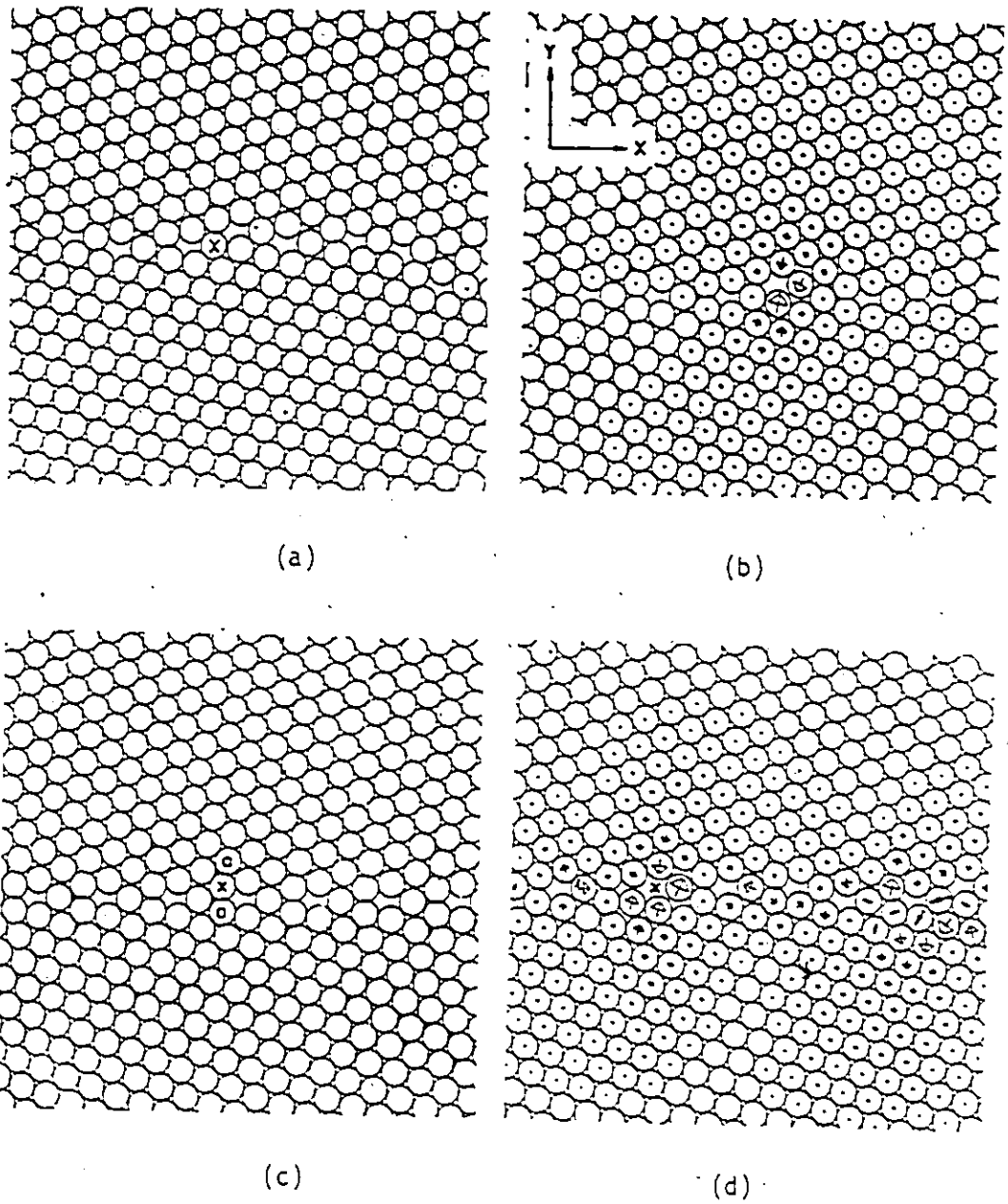

Figure 2.15 Vacancy structure in a grain boundary calculated by molecular statics. (a) is a short periodic boundary, (b) with atom X removed, the vacancy is confined to a small area. (c) is a long periodic boundary and (d) with atom X removed, the vacancy is confined to a larger area. (ref. A37)

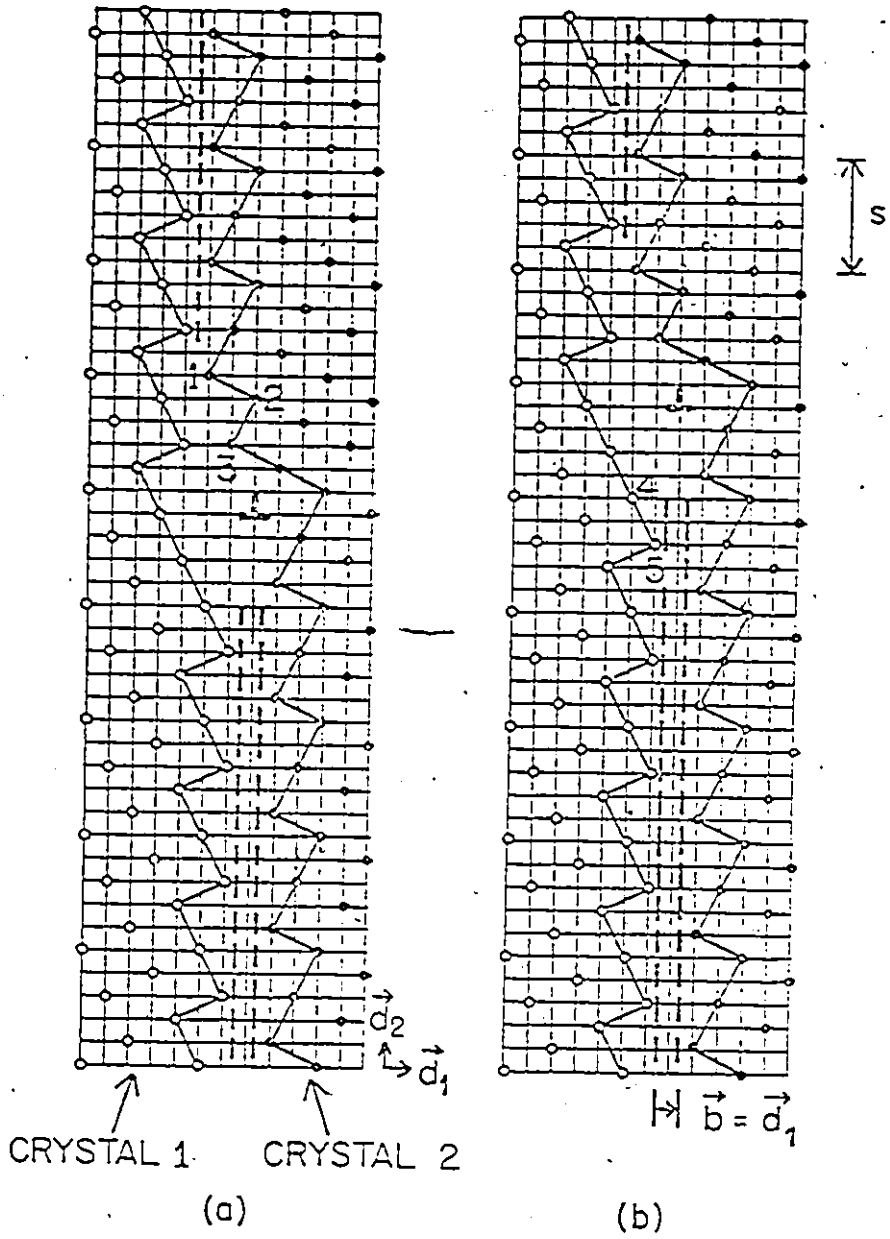

Figure 2.16 Diagram of the atomic shuffles necessary during the adsorption of a vacancy by a secondary dislocation with a step core structure. Atoms 1,2 and 3 from crystal 2 are removed, the vacancy is annihilated and atoms 4 and 5 add to crystal 1. (ref. A11)

2.1.2 Grain Boundary Diffusion

This section will review present theories of the characteristics and mechanisms of grain boundary diffusion. Various aspects of grain boundary diffusion behaviour will be considered which will lead to a discussion concerning the mechanisms of grain boundary diffusion.

Measurement of Boundary Diffusivity

There are various methods of determining the diffusivity of a grain boundary. In most methods, the value determined is the product of the boundary diffusivity, D_b, a distribution coefficient, k and the boundary width, δ. There are two main methods employed in measuring grain boundary diffusivity, the first is to measure the concentration profiles in the bulk as material leaves the boundary as shown in Figure 2.17 or by measuring the accumulated material on a surface which leaves an exposed boundary.

There are three features which can be measured using the bulk concentration profile technique for boundary diffusivity; (i) penetration depth of solute Y , (ii) the angle ϕ between the isoconcentration contour tangent and the boundary and (iii) the average concentration C_a present in thin slices of material perpendicular to the boundary. The first two methods are subject to considerable errors and therefore, the third method is preferred. All of these techniques rely on the solution of Fisher (A14) and Whipple (A21) for volume concentration profiles resulting from grain boundary diffusion.

The surface accumulation technique as shown schematically in Figure 2.18 does not rely on volume diffusion as the previous methods do. It relies on the assumptions that the solute capacity of the

boundary is much lower than the capacity of the surface. Therefore, a quasi- steady state is established in the boundary and the average surface concentration reflects the boundary diffusivity. Standard surface measurement techniques such as Auger electron spectroscopy are employed.

Given the diffusivity product $kD_b\delta$, a value of the boundary width δ is necessary in order to evaluate the boundary diffusivity. Fisher made the assumption that the width was on the order of 0.5 nm (A20), an estimate very close to measured values. The techniques employed to determine the width are:

(1) direct observation using field ion microscopy.

(2) diffraction techniques which employ scattering from the periodic nature of the grain boundary structure using X-rays or electrons.

(3) kinetic measurements from long term diffusion experiments where the kinetics rely heavily upon the boundary diffusivity.

Grain Boundary Diffusivity Anisotropy

The model of a low angle tilt grain boundary consists of an array of lattice dislocations. As anticipated, since the dislocation cores are areas of high disorder then, the diffusion of solute down the dislocation cores will be faster than between the cores. Therefore, for a simple tilt boundary as shown in Figure 2.19a, diffusion parallel to the cores will be greater than perpendicular to the cores and a high degree of diffusive anisotropy exists. As the misorientation angle increases, the anisotropy decreases smoothly as shown in Figure 2.19b but is still finite at the maximum tilt angle of 45 degrees. This suggests that a discontinuous shift in structure away from the model of

an array of lattice dislocations does not occur. In addition, the boundary at the maximum tilt angle must retain some form of structure to produce the residual anisotropy observed.

Orientation Effects upon Grain Boundary Diffusivity

The effects of orientation upon the boundary diffusivity are shown in Figure 2.20 for two different types of tilt boundaries. The diffusivity is expected to rise as the misorientation increases (as the dislocation core density increases). However, at particular orientations, deep cusps in diffusivity appear. These cusps correspond to the formation of high coincidence boundaries. Since the misfit at these orientations is small, the diffusivity is expected to decrease. It is interesting to notice that not all high coincidence boundary orientations produce cusps as shown by $\Sigma = 9$ boundaries as compared to $\Sigma = 3$ or $\Sigma = 11$ boundaries in Figure 2.20.

Boundary Diffusivity and Dislocation Type

When considering small misorientation boundaries, the two main forms are tilt and twist boundaries. Each is characterised by an array of lattice type dislocations; edge for tilt boundaries and screw for twist boundaries. Experimental evidence has indicated that edge dislocation cores provide a higher diffusivity path than screw dislocation cores; therefore, tilt boundaries possess a higher diffusivity than twist boundaries. In addition, these perfect dislocations may dissociate into an array of partial dislocations with a stacking fault present between them. Experimental evidence has shown that the diffusivities of such boundaries are less than that of the corresponding boundary constructed from perfect dislocations of the same

type. It is suggested that the stacking fault does not behave as a high diffusivity path and the core of the partial dislocations is less active in transporting atoms than their perfect counterpart.

Unfortunately, the arguments presented above do not apply when considering high angle grain boundaries since the core structures change considerably. When the cores are closely spaced, the dislocation cores lose their individual properties. The cores then must be described collectively in terms of structural units. It is the properties of the structural units which define the diffusivity of the boundary.

Boundary Diffusivity and Boundary Migration

It has been suggested (C1,A22) that the diffusivity of a migrating boundary is several orders of magnitude greater than that of the stationary counterpart. There is also experimental evidence (C11,C15) which suggests that boundary diffusivity is constant regardless of whether the boundary is migrating or stationary. A higher boundary diffusivity would initially suggest that the structure of stationary and migrating boundaries differ considerably. It was suggested (A22) that the change in structure resulted in extremely long atom jumps within the boundary.

Impurity Effects on Boundary Diffusivity

The effects of impurities on self diffusion in a grain boundary are variable and system dependent. The impurities can enhance or retard boundary diffusion. As shown in Figure 2.21, small amounts of Ta in Au results in a shift of the activation energy and pre-exponential factor. The impurity most likely interacts with the dislocation core structure of the boundary or other grain boundary defects.

Grain Boundary Diffusion Mechanisms

The most accepted mechanism for grain boundary diffusion is by atom jumping by a defect mechanism in the core of the grain boundary. The experimental evidence which substantiates this postulate (A15) is:

(1) Both creep and sintering studies have indicated that diffusion fluxes are established in the grain boundaries since radical shape changes occur during creep and during sintering experiments. Pores which exist between grains slowly shrink.

(2) Net fluxes of atoms along grain boundaries are produced during the processes of electromigration and thermomigration. Voids are usually present and grow thus indicating a vacancy flux has been established.

(3) The effects of hydrostatic pressure on boundary diffusivity has indicated that the activation volume for boundary diffusion is on the order of 1.1 atomic volumes. The activation volumes for self diffusion in the bulk occurring by a vacancy mechanism is usually 0.9 atomic volumes. This suggests that boundary diffusion may also occur by a vacancy mechanism.

The most accepted mechanism for boundary diffusion occurs by an exchange with a grain boundary vacancy. Interstitials can exist within the grain boundary core but are suggested to require considerably more energy to create than vacancies. In order to substantiate this mechanism, a number of molecular dynamic calculations (A17,A18,A19) have been performed and the results of the calculation are shown in Figure 2.22. A summary of the results of the calculation is as follows:

(1) The vacancy jumped mainly within the core structure of the grain boundary. Sites within the boundary which possessed higher binding

energy also had the highest jump frequencies.

(2) The jump occurred more along the tilt axis than perpendicular to it. This confirms that atoms jump along the dislocation cores in low angle boundaries and the anisotropy seen in boundary diffusion.

(3) The effective jump frequency of the vacancies followed a standard Arrhenius relationship.

(4) Atoms occasionally jumped into interstitial sites. If an atom was in an interstitial site, it was rendered immoble and could only move if annihilated by a vacancy in a neighbouring site. Therefore, diffusion by an interstital mechanism is unlikely.

(5) Occasionally, direct atom exchange was observed but was localised to a particular area and therefore should not contribute to boundary diffusion.

From these results and experimental observations, it can be suggested that for the majority of systems, boundary diffusion occurs by a vacancy mechanism.

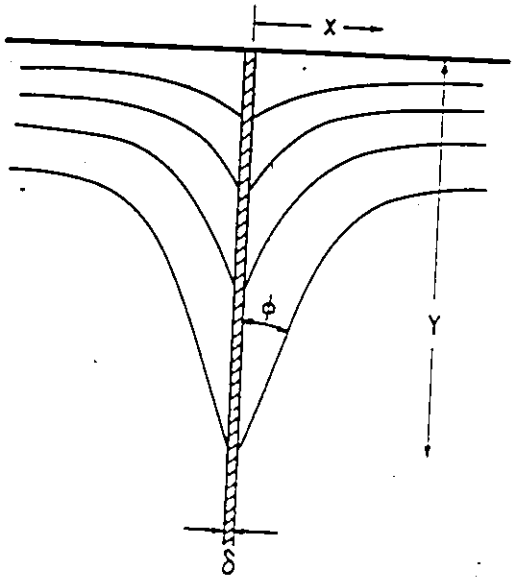

Figure 2.17 Isoconcentration contours for diffusion from a grain boundary of thickness δ into the bulk. The solute penetration depth Y, the angle between the boundary and the isoconcentration contour tangents ϕ and the average concentration C_a in a slice parallel to the surface are quantities measured to determine the boundary diffusivity. (ref. A10)

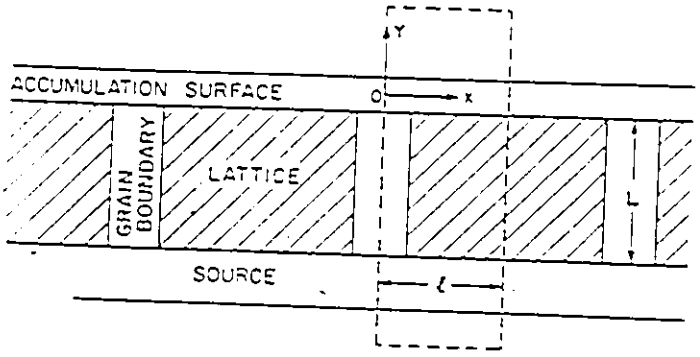

Figure 2.18 Diagram depicting the geometry of the surface accumulation technique in measuring boundary diffusivity. Diffusivity is deduced from the total amount of solute accumulated on the surface opposite the source. (ref. A16)

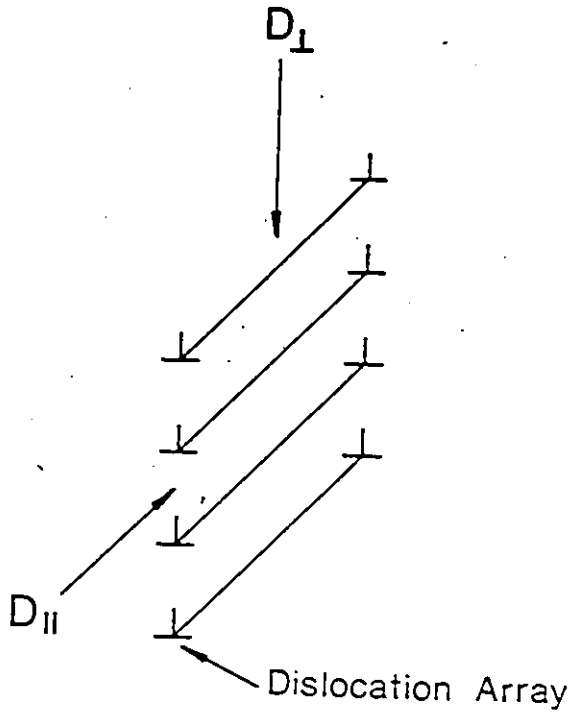

(a)

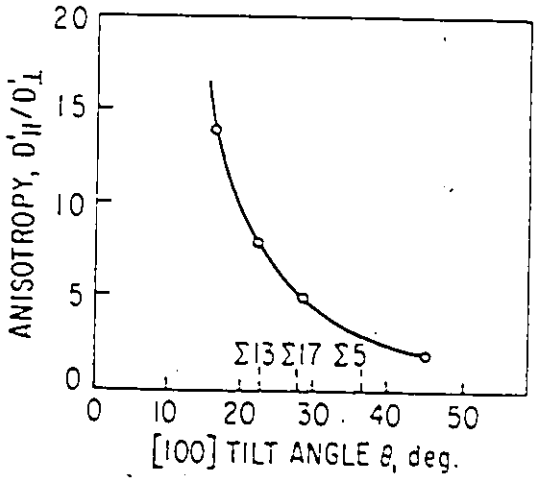

(b)

Figure 2.19 Anisotropy in grain boundary diffusivity for tilt boundaries. (a) shows a simple tilt boundary with preferred diffusion paths. (b) shows the dependence of anisotropy with misorientation for a [001] boundary. (ref. A10).

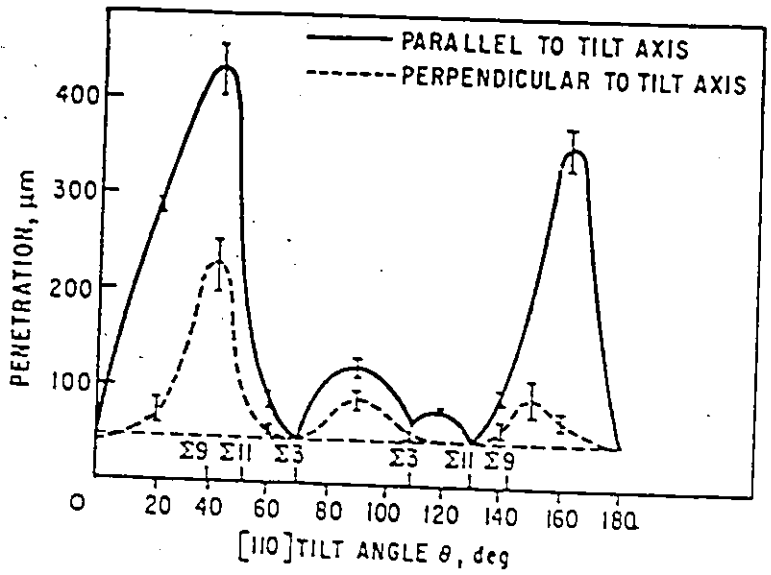

Figure 2.20 Penetration depth of zinc into [110] tilt boundaries in aluminum at 250°C. (ref. A10)

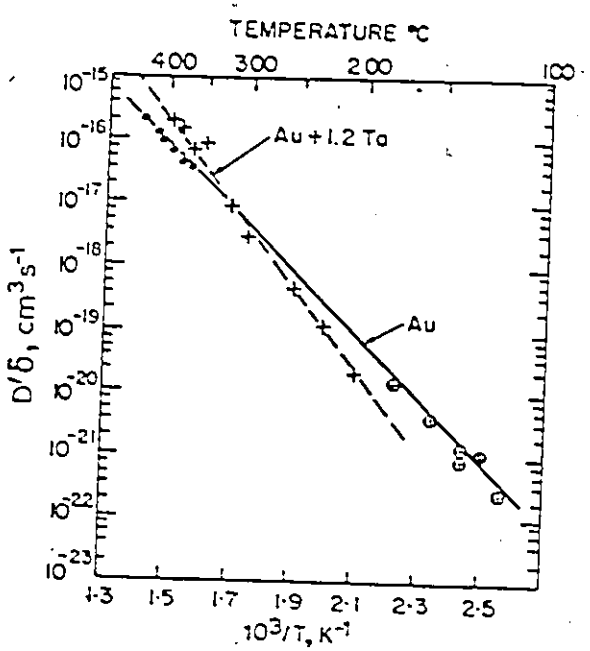

Figure 2.21 The effects of impurities on boundary diffusivity. The boundary self-diffusion of Au is modified by the presence of 1.2% Ta. (ref. A10)

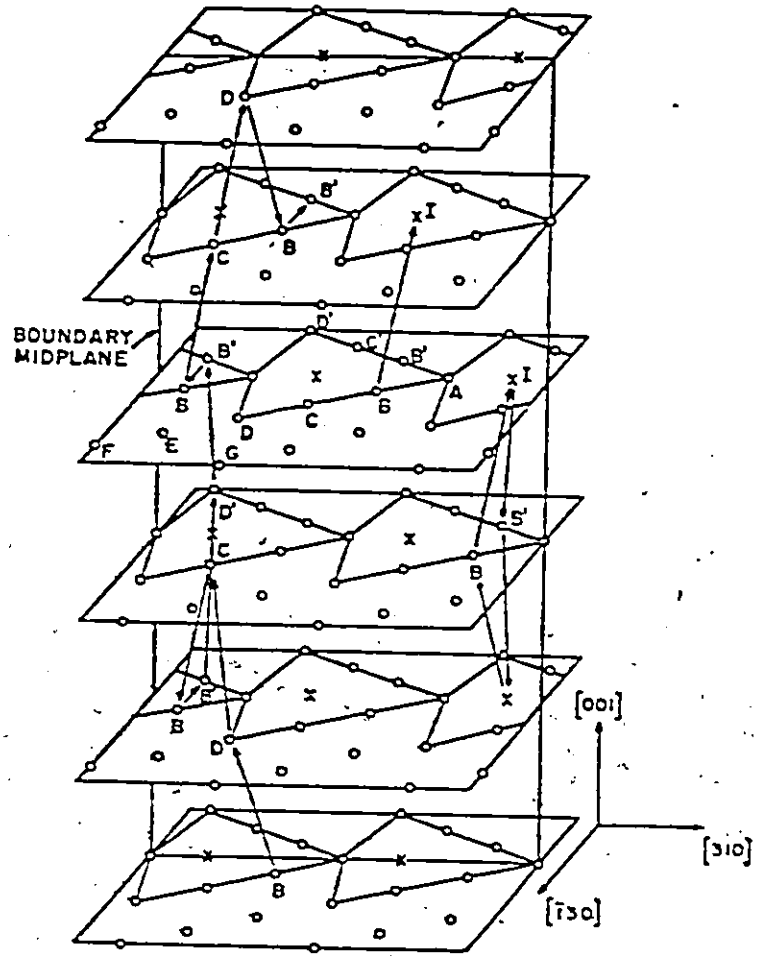

Figure 2.22 The results of a molecular dynamics study showing the trajectory of a vacancy in a portion of a [001] tilt boundary in bcc Fe at 1500K. The [001] scale is magnified for clarity. Note the preference of the vacancy to travel in the [001] direction which is consistent with a vacancy mechanism for boundary diffusion. Such a preference in direction corresponds to anisotropic diffusion behaviour. (ref. A18)

2.1.3 Grain Boundary Migration

This section will consider various aspects of grain boundary migration. It will illustrate the close relationship between grain boundary migration, grain boundary sliding and point defects within the boundary. General characteristics of boundary migration will be considered which will lead to an explanation of the mechanisms of boundary migration.

Grain Boundary Driving Forces

A grain boundary can migrate at speeds whose spectrum can cover several orders of magnitude. The range of driving forces for migration can also range over several orders of magnitude and can be very diverse in origin. The magnitudes and origins of a few sources are given in Table 2.1. It has not been determined whether a lower threshold level for driving forces exists below which migration cannot occur.

Table 2.1 Driving Forces for Boundary Migration

Source	Force (N/m^2)
Primary Recrystallization	10^8
Electromigration	10^2
Grain Growth	10^4
Discontinuous Precipitation	10^9
Tertiary Recrystallization	10^3

The general relationship between the driving force P and the boundary velocity V is:

$$V = M P^n \qquad (2.3)$$

where M is the boundary mobility and n is an experimentally determined factor which reflects process kinetics. The driving force can be related to the change in free energy per mole as:

$$P = \Delta G/V_m \qquad (2.4)$$

where V_m is the molar volume. The factor n can be assumed to be unity under special circumstances and this usually leads to the assumption that the mobility M is constant. This is usually true for dilute alloys undergoing recrystallization or grain growth. It is possible for n to have higher values if different growth mechanisms are operating (such as the growth spirals mechanism for crystal growth).

The mobility of the boundary (M) can be related to a diffusion process assuming that the boundary migrates by random jumps across the boundary through the Einstein equation:

$$M = DV_m/RTr \qquad (2.5)$$

where D is an effective diffusivity and r is the effective jump distance. The functional dependence of the mobility factor will determine the migration characteristics of the boundary. The main experimental features of the migration of grain boundaries are:

(1) Boundary orientation is critical in determining the mobility of the boundary. Certain misorientation have extremely high mobilities.

(2) Coherent twins and low angle grain boundaries usually have very low mobilities.

(3) High coincidence boundaries have greater mobility under conditions

of low driving force and high solute content. However, this advantage is lost if the opposite conditions exist.

Temperature Dependency of Boundary Migration

If the mobility of a grain boundary is related to a diffusion process as indicated by equation 2.5, then the diffusivity term will contain an activation energy in an Arrhenius type relationship. The activation energy usually found is half the value for diffusion in the bulk. However, in determining this energy, careful consideration must be given as to the conditions of measurement. The nature of the boundary, driving forces and solute interactions must be kept constant for a meaningful interpretation of the data. Even if these conditions are met, there still can be changes in other factors such as the pre-exponential factor as shown in Figure 2.23 even though the activation energy remains constant. The effect of impurities in the boundary is to increase the activation energy considerably but this effect is velocity dependent and will be considered in the next section.

Solute Effects on Boundary Migration

The effect of impurities upon the mobility of grain boundaries has been considered by many investigators. The main difficulty in quantifying the effects of solutes within the boundary is determining the interaction energies of the solute with the boundary structure and the overall boundary energy and energy profile of the boundary. The main experimental observations concerning the effects of solutes on boundary migration are:

(1) Generally, solutes inhibit easy movement of grain boundaries.

However, as the temperature rises, the effects of solute drag on boundaries are eliminated and the activation energy for movement decreases to that of boundary diffusion as shown in Figure 2.24.

(2) The boundary exhibits high and low mobility regimes which correspond to high and low driving forces respectively as shown in Figure 2.25. Generally, as the solute concentration rises, the mobility decreases (the activation energy for migration increases).

(3) Different solutes have differing effects on mobility for a given matrix. Faster moving solutes such as Au and Ag in Pb affect mobility more strongly than slower moving solutes such as Sn.

(4) High coincidence boundaries are less susceptible to the effects of solute upon migration than other (random) boundaries.

(5) It has been assumed that the solute is adsorbed into the boundary. Solutes which are actually repelled by the boundary core can also modify the mobility of the boundary.

There have been numerous attempts made in order to model the effects of solute upon boundary mobility. The models of Lucke and Stuwe (A24) assumed that the solute and boundary interacted according to a well defined energy profile. At equilbrium, the profile was symmetric and the force upon the solute atom due to the energy gradient was opposed by an equal but opposite force. If the boundary were stationary, the energy profile would be symmetric and the net force would be zero. An alternative formulation would employ the chemical potentials of the components. As the boundary migrates, the profile becomes asymmetric. The forces on each side of the profile are no longer equal. For low forces, the asymmetry of the profile would be small and the resulting

numerical calculation would require a large amount of precision. If the mean solute concentration were subtracted as performed by Cahn (A27) the calculation requires less precision. Hillert (A25) assumed that the force which acts upon the migrating boundary corresponds to the work done by moving the boundary. This work was identified as the Gibbs energy dissipated by the diffusional processes of boundary migration. A free energy profile must still be defined as well as diffusional fluxes for boundary migration.

Grain Boundary Migration Mechanisms

There are two main models used to describe the process of grain boundary migration. The first utilised a non-structural model of the boundary and assumes biased random jumps across the boundary. The second model is heavily based upon the actual or assumed structure of the boundary and assumes migration is due to the motion of grain boundary defects.

The random atom jump model (A20,A26) assumes atom jumps from one side of the boundary to the other are more frequent than the reverse jump rate as shown in Figure 2.26. The model assumes that a free energy barrier is present which an atom must jump over, if the thermal activation energy is sufficient. If the boundary is stationary, the atom jumps across the boundary in either direction are equal. Under a driving force, a free energy difference appears across the boundary biasing the atom flux and resulting in migration. In order to accommodate boundary structure into the model, Lucke et. al. (A26) modified the free energy profile as shown in Figure 2.27. It can be seen that if the boundary energy profile is narrow, the atom can add to the appropriate grain as

required. However, if the boundary energy profile is wide, the atom must first occupy a position resembling an interstitial site before jumping to the next grain or back again. Migration velocity then can be related to the diffusivity of atoms which can yield the familiar equations of thermally activated motion employing enthalpies and entropies of motion. If the atom jumps are vacancy assisted, then a correction for the enthalpies and entropies of vacancy formation within a grain boundary must be included. The model, as presented, is rather unspecific and cannot explain boundary structure effects and solute effects adequately. Specifically, if the atom motions are truly random, then the atoms jumps cannot maintain a given boundary structure easily over any length of time.

The structural model of boundary migration utilises all present knowledge concerning grain boundary structure and defects. The two main defects involved are grain boundary steps and dislocations. Migration by a step or ledge mechanism is a well known process especially in crystal growth between different phases. Atoms add to the edge of the step by jumping and the step moves one atomic position as shown in Figure 2.28. The net jump rate to the step is determined by thermodynamic factors as in the random atom jump model. This model is useful when the driving force is below some critical value and when migration is not accompanied by any form of boundary sliding or shear.

The dislocation model of migration is the most complex model and requires the movement of grain boundary dislocations. When these dislocations move, the resulting displacement of the boundary can be by sliding or by normal migration; and usually point defect emission or

adsorption occurs. Consider first the movement of an edge grain boundary dislocation as shown in Figure 2.29. As the dislocation moves the boundary exhibits both sliding and migration. A careful examination of the boundary core as shown in Figure 2.29 indicates the ratio of sliding to migration depends upon the orientation of the dislocation in the boundary plane. The most important feature is sliding or migration can occur without changing the boundary structure.

The climb or glide of a dislocation is accompanied by atomic shuffles which lead to migration. According to the geometry of the dislocation a number of diffusive jumps may be required. The number of jumps depends upon the the coincidence geometry of the boundary, the orientation of the Burgers vector of the boundary dislocation with the boundary plane and the dislocation core structure. The greatest number of jumps is required by a dislocation which has a Burgers vector perpendicular to the boundary plane with a large step at its core. Predicting the exact size of the core step is difficult, but it can be estimated through geometric means given very specific CSL orientations. Generally however, for random boundaries, the step size is not easily determined.

It is apparent that dislocation movement combines sliding and migration. It is possible to achieve pure sliding or migration by suitable dislocation configurations. Consider the following possible situations:

(1) A dislocation whose Burgers vector lies within the boundary plane. Such a dislocation can produce sliding without boundary migration. Core structure appears unimportant in this configuration.

(2) A dislocation with a large step core whose Burgers vector lies perpendicular to the boundary plane can move by climb and produce migration without a slide component. However, a source of defects is necessary.

Therefore, since these configurations are suggested to be rare, for a pure migration process, the sliding term must be eliminated or the sum of the Burgers vector components along the boundary plane must be zero. In addition long range diffusive fluxes cannot be established. A model which can accommodate these requirements for migration consists of three partial grain boundary dislocations as a spiral source in which the sliding term is eliminated. The requirement for the elimination of sliding component may be too restrictive as there are instances in which boundary migration has lead to the presence of boundary sliding also.

The effects of solute drag is suggested to result from the binding of solute to the dislocation cores. Under these circumstances, the solute is then required to diffuse along with the dislocation as it moves. In addition to diffusing along with the dislocation, the solute atom may inhibit the atomic shuffles required for movement.

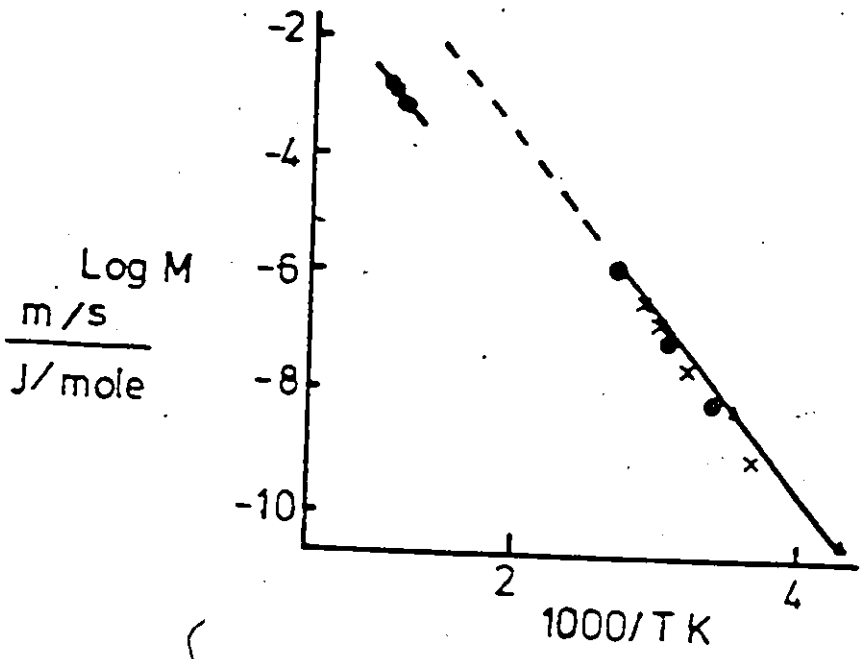

Figure 2.23 Mobility of zone refined aluminum as a function of temperature. Note the change in the pre-exponential factor even though the activation energy appears to remain constant. (ref. A12)

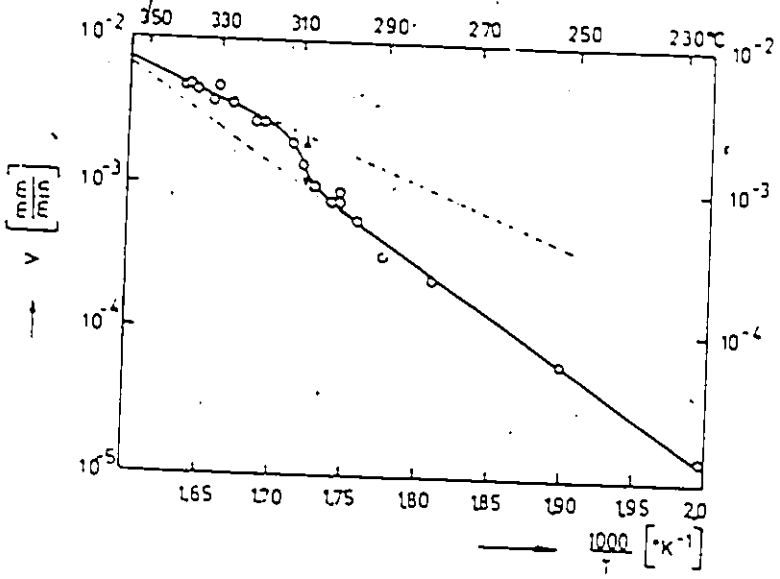

Figure 2.24 Effects of temperature on solute drag for 99.999% gold with iron additions. (ref. A26)

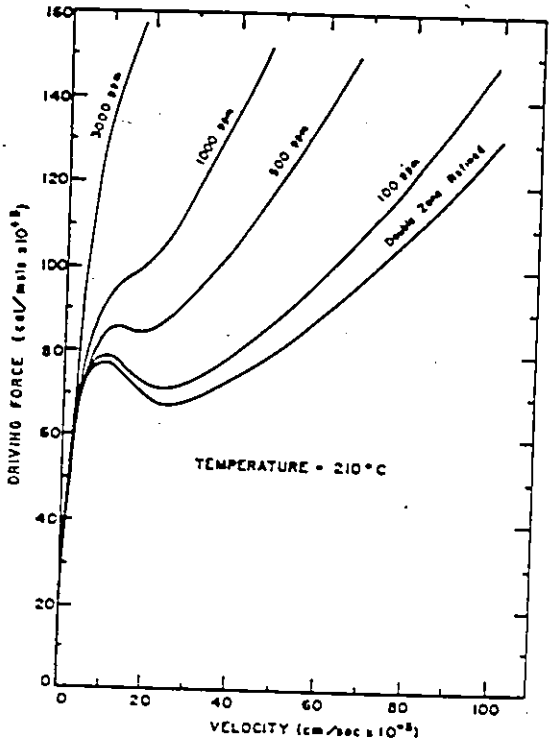

Figure 2.25 Velocity dependence upon driving force for varying tin additions to lead. (ref. A40)

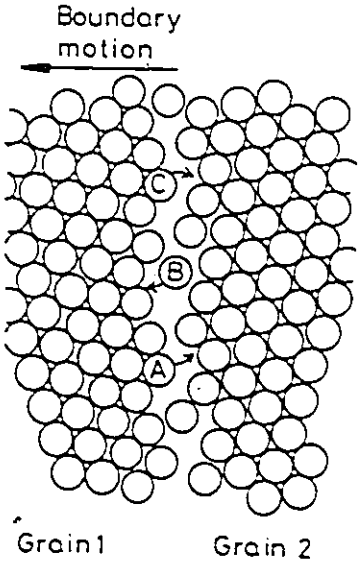

Figure 2.26 Biased atom jump model of grain boundary migration. Atom jumps from grain 1 to 2 are more frequent than from 2 to 1. The net result is the growth of grain 2 at the expense of grain 1. (ref. A29)

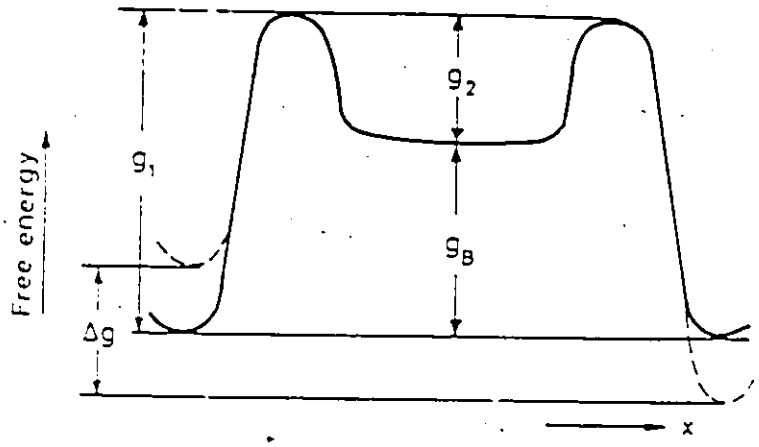

(a)

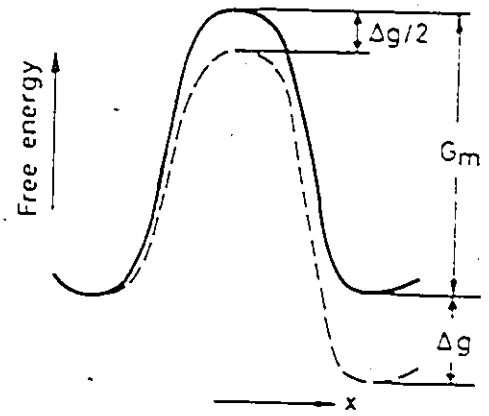

(b)

Figure 2.27 Modification of the free energy profile which can take into account grain boundary structure: (a) wide boundary (b) narrow boundary. (ref. A26)

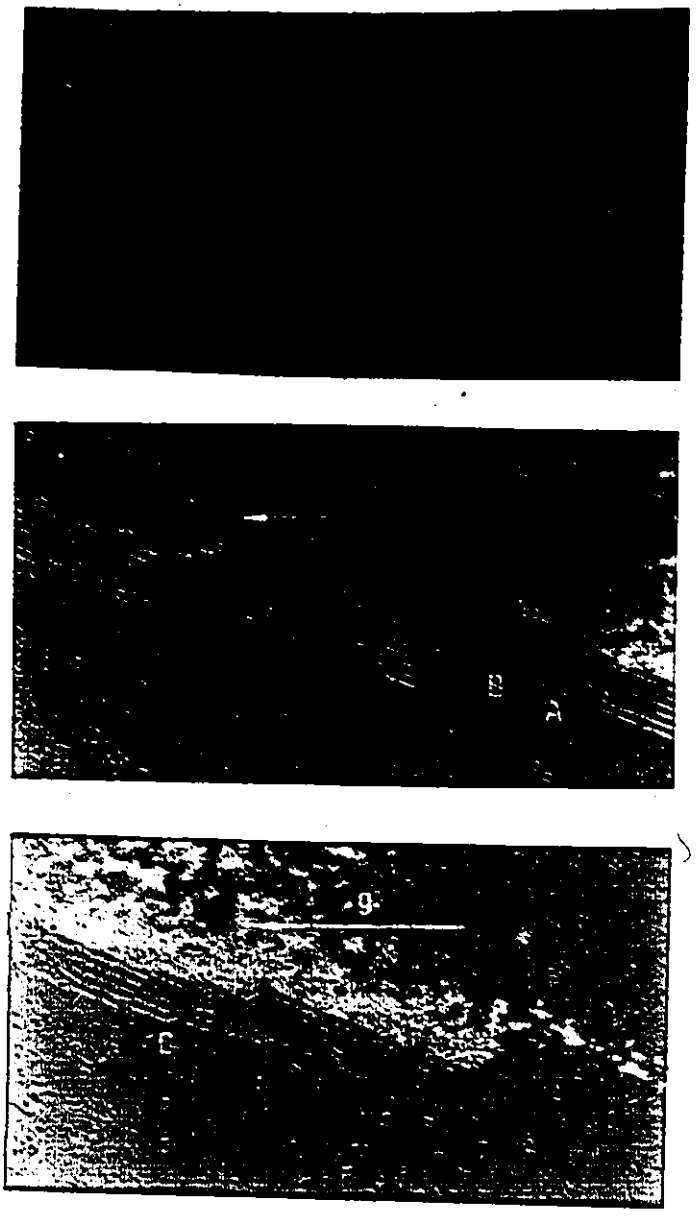

Figure 2.28 Growth of an annealing twin in aluminum by step motion. (ref. A12)

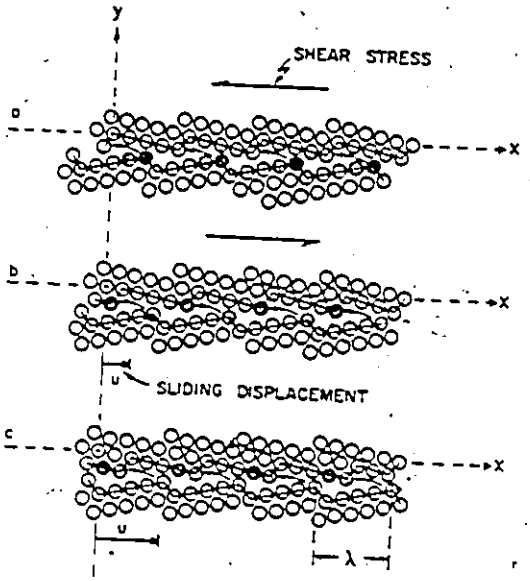

(1)

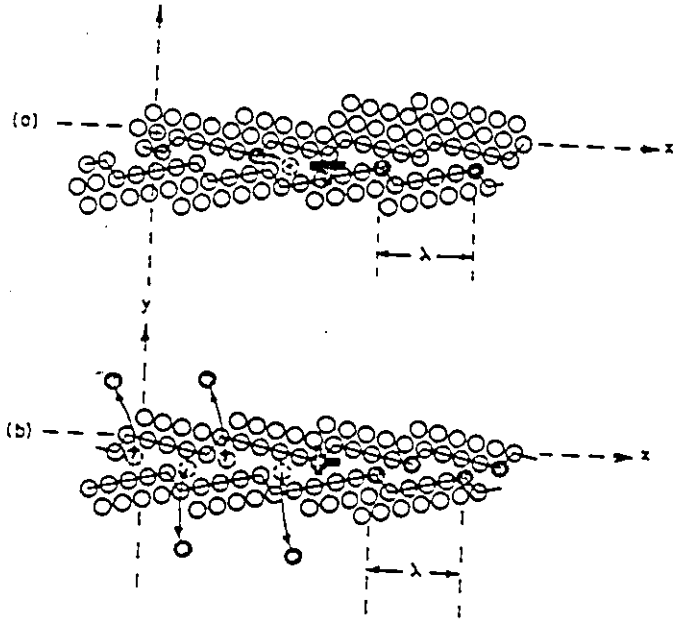

(2)

Figure 2.29 Grain boundary dislocation movement (1) resulting in migration and sliding. The process occurs at a grain boundary dislocation core as shown in (2) where in (a) if the dislocation glides sliding occurs and in (b) boundary migration occurs. (ref. A42)

2.2 Interface Controlled Solid Phase Transformations

Atomistic and structural properties of boundaries comprise the central focus in previous sections. This section will consider boundaries from a different perspective; the thermodynamic aspects of interface behavior in phase transformations and the role of a chemical driving force.

2.2.1 Boundary Behaviour

The model of a boundary as given by Hillert (B1) is not as structured as in previous considerations but boundary properties such as interfacial energy, diffusion and mobility are still of great importance. The boundary is regarded as a separate phase of limited thickness which possesses its own free energy description. Assuming it can possess a unique solute concentration like an alloy, it can then be considered in equilibrium with that alloy as shown in Figure 2.30a. If the bulk composition is X, then the boundary composition X_b is assumed to be linearly related by:

$$X_l^b = K X_l \qquad (2.6)$$

$$X_u^b = K X_u \qquad (2.7)$$

If material is transferred to the boundary, it will gain energy by the amount G_u and if tranferred to the next grain it will lose energy G_d. Therefore a net driving force does not exist as $G_u = G_d$.

Assuming that the boundary now moves with a low constant velocity, a concentration profile will be produced in the boundary phase and the shrinking grain phase as shown in Figure 2.30b. If a local equilibrium is still established on both sides of the grain, then the limiting upper concentration levels X_u^b and X_u will depend upon the

boundary diffusivity for their values. There are two free energy losses in this process which are the diffusion of solute in the concentration profiles in the boundary and shrinking grain, given as G_d and G_b. Since these are dissipative processes, they represent a drag upon the boundary, therefore, the suggested chemical driving force P that must be applied to overcome these drag forces is:

$$P = (G_u - G_l)/V_m = (\Delta G_d + \Delta G_b)/V_m \qquad (2.8)$$

where V_m is the molar volume. As the velocity increases, the concentration profiles increase in steepness until they reach a maximum as shown in Figure 2.30c where $X_u^b = X$ and $X_u = X/K$. In addition, the dissipation of free energy by diffusion has reached a maximum allowed still assuming local equilibrium. As the velocity increases further, the concentration profile become so narrow that they are mathematical features only. At this point, the interface can no longer be in local equibrium as shown in Figure 2.30d. Then, the free energy decrease (G_u-G_d) decreases to zero.

There are numerous transformations in which a chemical driving force is suggested to be acting upon a boundary or interface. One of these transformations is discontinuous precipitation which will be considered in the next section.

2.2.2 Discontinuous Precipitation

Discontinuous precipitation has been considered by many investigators (B1,B2,B3,B4,B5). Even though the nucleation event is still under consideration, the growth process has been well modelled. Many descriptions (B2,B3) considered the boundary diffusion problem as illustrated in Figure 2.31. The reaction is assumed to be controlled by

the boundary diffusion of solute away from the a - ao interface. Volume diffusion is usually neglected in most descriptions but it can be included for a more complete model. The problem assumes that the boundary flux divergence is balanced by the solute that is acquired by the boundary as it migrates. This flux divergence is controlled by the difference between the two alpha phases and the boundary velocity as given in Figure 2.31. The solution to the diffusion equation assumes a flat alpha interface and uses the alpha lamellae width (l) for boundary conditions.

The interface was also thought to migrate as a result of precipitate traction as shown in Figure 2.32. The precipitate interface is generally accepted as being driven by a chemical force. However, a convex alpha interface shape was observed indicating the alpha interface was also being driven. It was suggested by Hillert (B1) that the alpha interface was also being driven chemically.

In order to analyse the situation, Hillert (B1) and Sundquist (B7) assumed that chemical forces can act across a boundary as described in the previous section and had to balanced across the boundary in order to determine its final shape. The balance occurs between the chemical forces, capillarity and mobility terms in the form:

$$P - K = \gamma/r + v/M \qquad (2.9)$$

where, P is the chemical driving force, γ is the surface energy or the capillarity constant, r is the radius of curvature, v is the velocity, M is the boundary mobility and K is the free energy lost due to other processes.

The calculation of the driving forces for both the alpha and

beta interfaces can be illustrated using free energy diagrams. The driving force for the interfaces is illustrated in Figure 2.33. It can been seen that numerous energy sinks are available for reducing the chemical driving force for precipitation. They are volume diffusion, boundary diffusion, capillarity or surface effects, boundary mobility and the retained supersaturation present in the alpha lamellae.

The description given in this section is based on the macroscopic principles of thermodynamics which are applied to a boundary. The validity of such an argument in describing the reason for movement of the boundary is still a controversial subject.

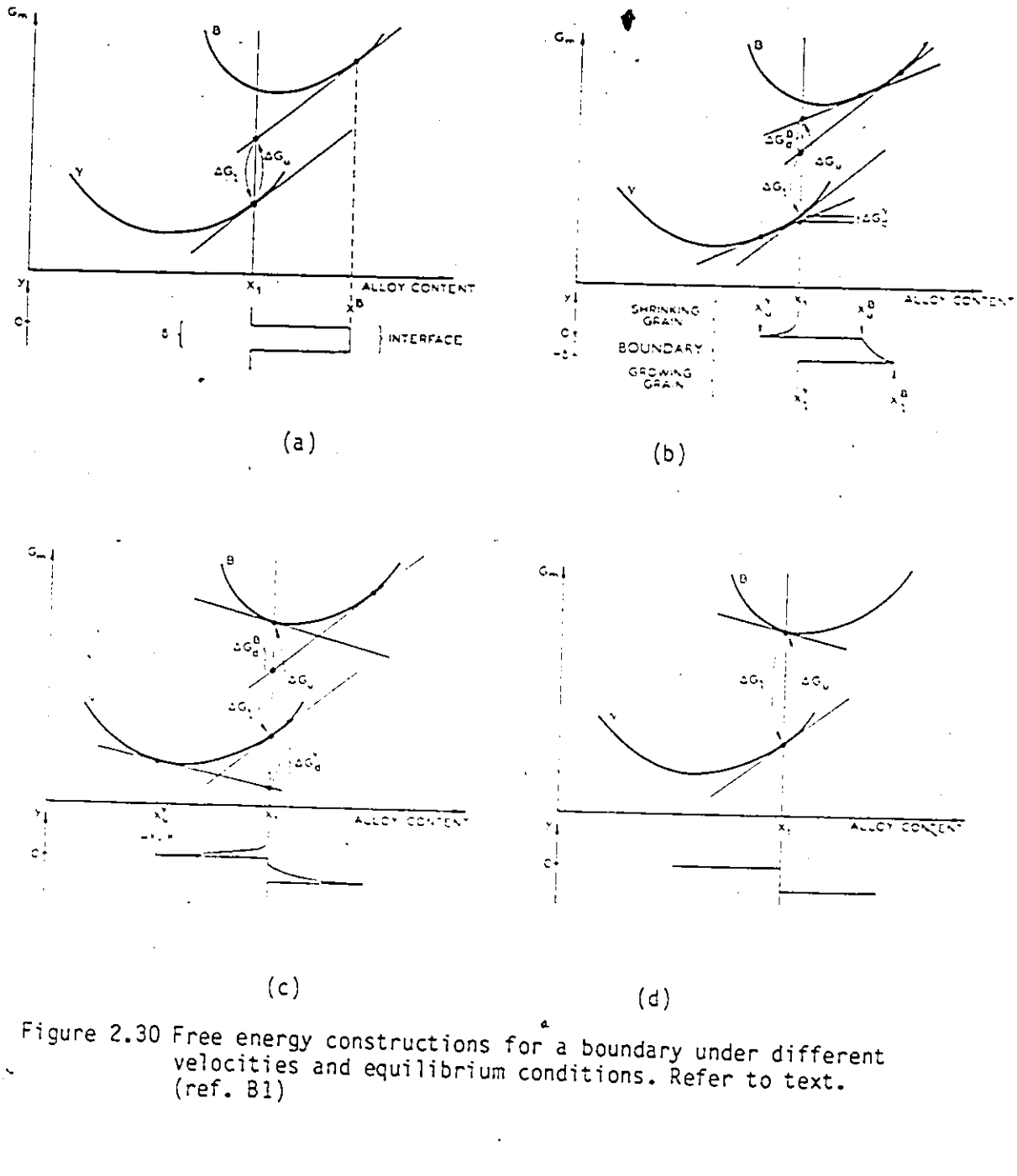

Figure 2.30 Free energy constructions for a boundary under different velocities and equilibrium conditions. Refer to text. (ref. B1)

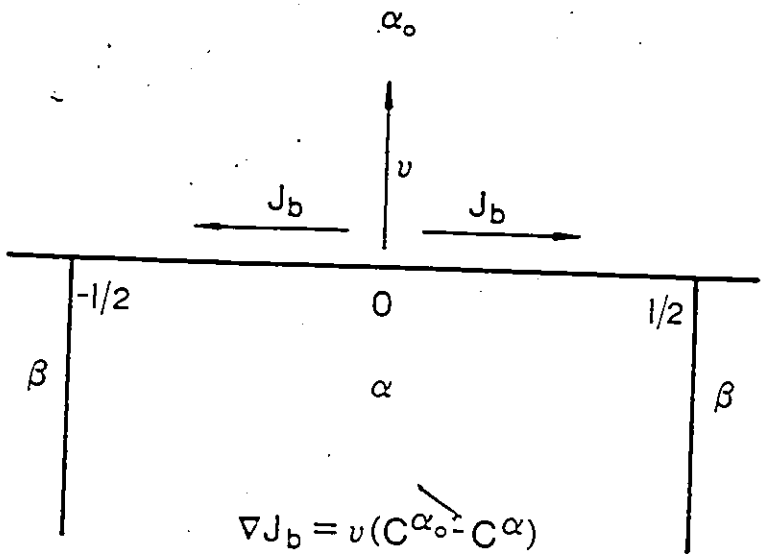

Figure 2.31 Discontinuous precipitation and the boundary diffusion problem the situation presents. The equation describes the flux divergence balance present at the interface. (Refer to text)

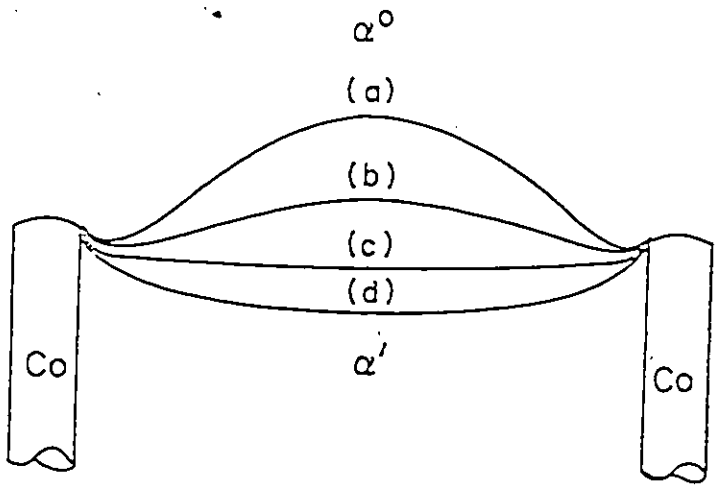

Figure 2.32 Possible alpha interface shapes in discontinuous precipitation. (a) is an interfaces driven by a large force, (b) driven by a smaller force, (c) no net force (planar interface) and (d) the interface is dragged by the precipitates. (ref. B6)

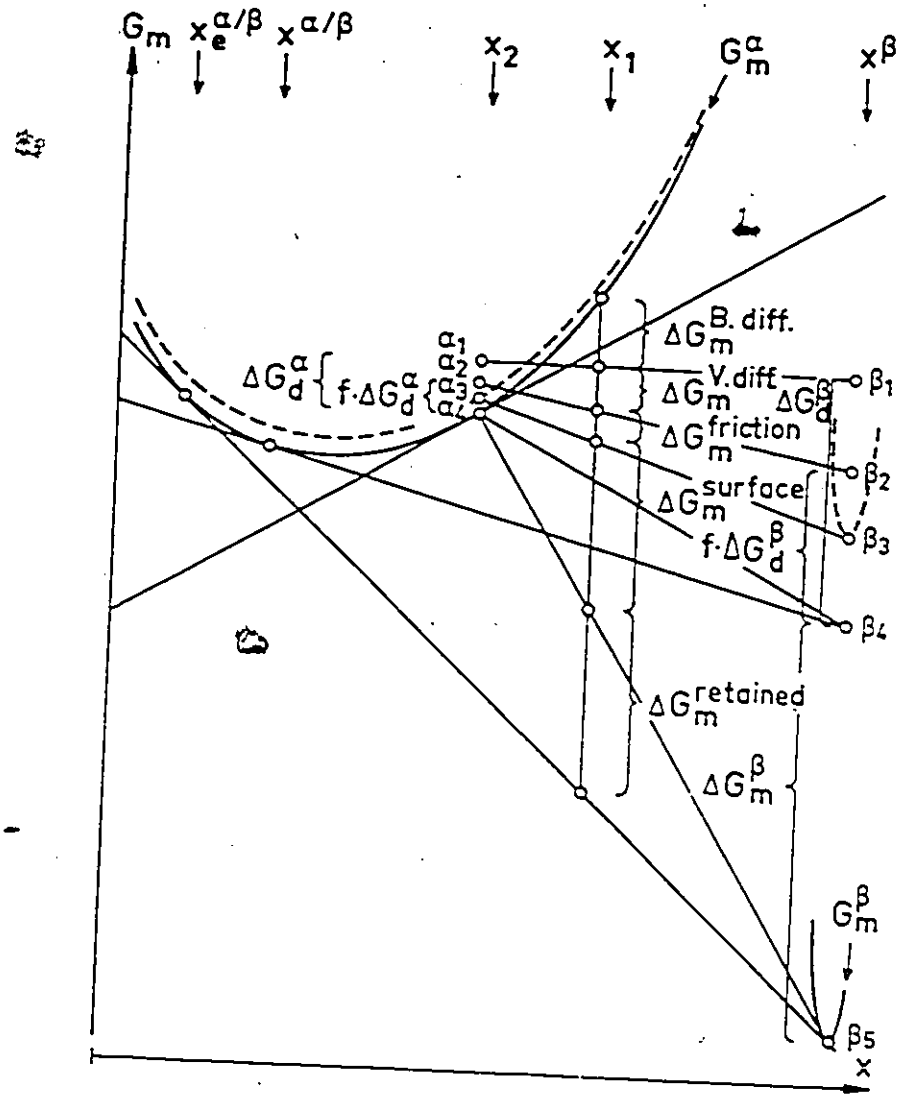

Figure 2.33 Free energy diagram illustrating the chemical driving force for the interfaces in discontinuous precipitation. X_e is the equilibrium alpha concentration which is never realised but becomes X_1 due to capillarity effects of the beta phase. X_2 is the initial concentration and $X_{\alpha\beta}$ is the concentration in the product alpha phase. The effective driving force for each phase is shown ($f\,\Delta G_\alpha$ for the alpha interface and $f\,\Delta G_\beta$ for the beta interface) as well as five different energy sinks. (ref. B2)

2.3 Chemically Induced Grain Boundary Migration

Chemically induced grain boundary migration (CIGM) earned its original importance in the study of discontinuous precipitation. The original proposal was that the interface between the supersaturated matrix and the alpha lamellae was chemically driven. However, since the process is complicated by the presence of the beta phase, the search for chemically driven boundary without a second phase precipitating was initiated. Thus, the required phenomenon was reported by Hillert and Purdy (C1) in 1978. However, CIGM was reported earlier by den Broeder (C19) in 1972 , Tu (C20) in 1977 and possibly as early as 1938 (C21), even though it was not recognised as CIGM originally.

The group of investigators which were to study CIGM next, developed a model based on the synchronous climb of grain boundary dislocations. The climb of the dislocations was a result of solute diffusion along the boundary and therefore, the phenomenon was termed diffusion induced grain boundary migration (DIGM) by this group. This model precludes the existence of a chemical force operating to drive the boundary. The origin of this phenomenon has been the centre of controversy in recent years.

The sections which will follow will consider the general characteristics of CIGM and then consider the details of each of the models separately.

2.3.1 General Characteristics of CIGM

The purpose of this section is to briefly outline the experimentally determined characteristics of CIGM. CIGM has been found in a large number of binary systems both metallic and non-metallic as

given in Table 2.2. The actual migration characteristics of migration vary from system to system but all demonstrate a few basic features. The first feature is the formation of an alloyed volume as shown schematically in Figure 2.34. In addition to uniform migration, CIGM also exhibits bidirectional migration as shown in Figure 2.35; therefore, migration proceeds against capillarity forces. CIGM also produces other curious effects in both the bulk and on the surface which will be considered individually.

2.3.1.1 Surface Modification by CIGM

CIGM also exhibits certain peculiar morphological effects which appear in certain systems and not others. The first is the surface feature of hillock formation (C1) usually observed in the Fe-Zn system as shown in Figure 2.36. The dilatation is usually large and can buckle thinner foils. Occasionally, the migrated region exhibits grain boundary facetting as migration proceeds as in the Cu-As system (C5). The facet formation is a rare event as not all boundaries exhibit this feature.

The most interesting surface modification feature that CIGM exhibits is the effect of surface recrystallization. The effect has been termed "Diffusion Induced Recrystallization (DIR)" by den Broeder (C9). The region affected always possess a finer grain structure than the parent material as shown in Figure 2.37. A fine layer of alloyed new grains is found near the surface for vapour induced CIGM or the interface for solid diffusion couples. Normal CIGM is always present and operating on the original grain boundaries of the annealled matrix. Such an effect may find use in surface alloying of materials as proposed

by Hillert and Li (C35).

2.3.1.2 Migration Characteristics in the Bulk

CIGM also demonstrates interesting behaviour in the bulk. The centre of this discussion concerns the alloying effect of CIGM in a binary system. CIGM is also capable of dealloying a single phase alloy when the boundary migrates. Dealloying effects have been found in the Fe-Zn system (C1) where the solute (zinc) was removed by evaporation from the surface of the Fe-Zn alloy. This effect has been also reported in the Cu-Ni system. In this particular instance, the boundary migrates to leave a Cu depleted zone in its wake. The Cu is selectively removed at the surface at a faster rate than the Ni by sputtering as shown in Figure 2.38. Another form of dealloying CIGM observed by Solorzano (B3) appears as a precursor to discontinuous precipitation in the Al-Zn system as shown in Figure 2.39. In this instance, the boundary sweeps out into the supersaturated matrix leaving a zinc depleted zone and zinc rich precipitates at the sides. This effect is not the beginning stages of discontinuous precipitation (B13) as the spacing between the zinc rich precipitates is far too large.

The concentration profile of the alloyed zone yields additional information concerning migration behavior. Consider the profile left in the wake of a boundary as shown in Figure 2.40. The erratic migration behavior is also reflected in the nonuniformity in the concentration profile. A more uniform concentration profile usually denotes a more uniform migration behaviour of the boundary. Whereas the concentration profile perpendicular to the boundary indicates the uniformity of migration, a concentration profile parallel to the boundary in the

alloyed zone can yield the value of the grain boundary diffusivity. As shown in Figure 2.41, the concentration profile for a thin foil exposed to solute on both sides appears hyperbolic in nature. Figure 2.42 gives the profile as exponential. Using an expression developed by Cahn (B4) for a boundary diffusion controlled flat interface,

$$\frac{X_o - X}{X_o - X_\alpha} = \frac{\mathrm{Cosh}(Z\sqrt{v/KD_b\delta})}{\mathrm{Cosh}(S\sqrt{v/KD_b\delta})} \qquad (2.10)$$

given that X_o is the surface concentration, v is the boundary velocity, X is the concentration along the boundary, K is the boundary - matrix equilibrium factor, S is the half foil thickness and D_b the boundary diffusivity. Using this expression Hillert and Purdy calculated the boundary diffusivity of Zn in Fe boundaries. Their result was the boundary diffusivity was orders of magnitude greater than for stationary boundaries.

Since other grain boundary characteristics are orientation sensitive, CIGM should also exhibit orientation dependence. An orientation study by Pan (C48) was performed on thin layers employing the Au-Cu and Au-Ag systems. The result for <111> tilt boundaries is given in Figure 2.43 and for <100> tilt boundaries in Figure 2.44. As expected low angle boundaries possess low mobility. There is the appearance of facetting during migration which does not appear to modify the overall migration significantly. The migration behaviour appears continuous and reduces to zero for those boundaries that exhibit high coincidence such as the <111> boundaries at 60 degrees ($\Sigma = 3$).

Finally, CIGM is also affected by the physical contraints placed on a sample. Constraint studies were performed by Pan (C48) employing Au

tilt boundaries formed by evapouration onto NaCl substrates. Some of the samples were removed from their substrate and others were not. As shown in Figure 2.45, Migration is inhibited on the boundaries constrained to their substrates substantially.

Table 2.2 Representative CIGM - DIGM Systems

System	Temperature Range °C	Diffusion Time hrs	Ref.
Ag-Zn	350	89	C43
Al-Zn	160 - 200	24 - 270	C37,C38
Au-Ag	200 - 375	72 - 396	C7,C18
Au-Cu	150 - 450	5 - 137	C7,C8,C23
Ca-ZrO2	1400	50	C42
Cr-W	1250 - 1600	16 - 96	C19
Cu-Al	350	12	C10,C12,C16
Cu-As	300 - 440	4 - 53	C5
Cu-Cd In	400 - 450	.5 - 96	C28
Cu-Ni	350 - 900	1 - 7	C9,C11,C13,C15
Cu-Pd	150	12	C14
Cu-Sn	400 - 450	.5 - 96	C28
Cu-Zn	250 - 400	1 - 3900	C5,C6,C10,C17 C22,C23,C34,C43
Fe-Zn	400 - 700	.25 - 244	C1,C2,C3,C4 C22,C36,C45
KBr-(OH)	20 - 30	6 Yrs	C39
Mo-Ni	800 - 1290	3 - 57	C24
Ni-C*	550 - 600	10 - 48	C25
NiO-O	1200	24	C26
Ag-O Cu-O	600	1	C33

* - No microanalytical measurements performed to substantiate that alloying has taken place

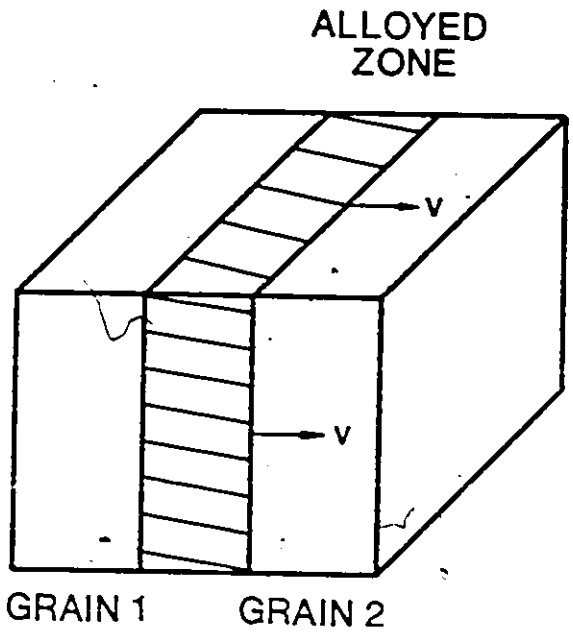

Figure 2.34 Schematic representation of uniform migration of a grain boundary. Solute flux is along the boundary.

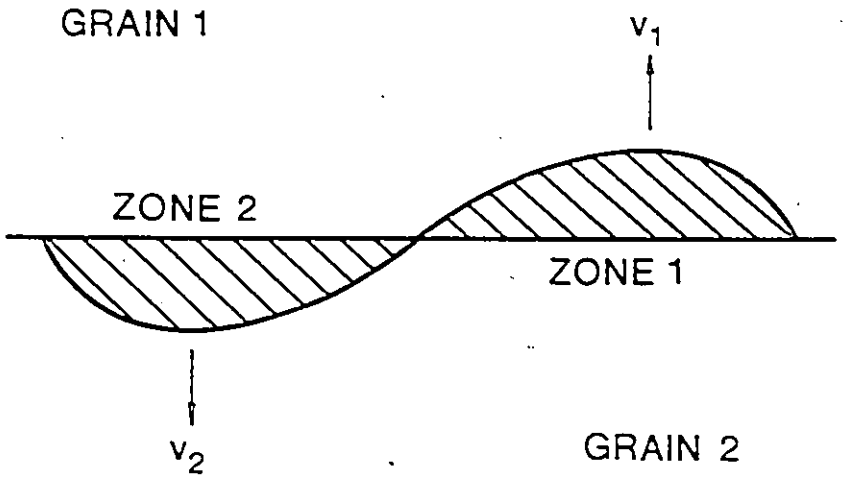

Figure 2.35 Schematic represntation of bidirectional migration. Zone 1 has the orientation of crystal 1 and zone 2 has the orientation of crystal 2.

Figure 2.36 Surface relief of an iron foil after zincification of 4hrs at 600°C (ref. C1)

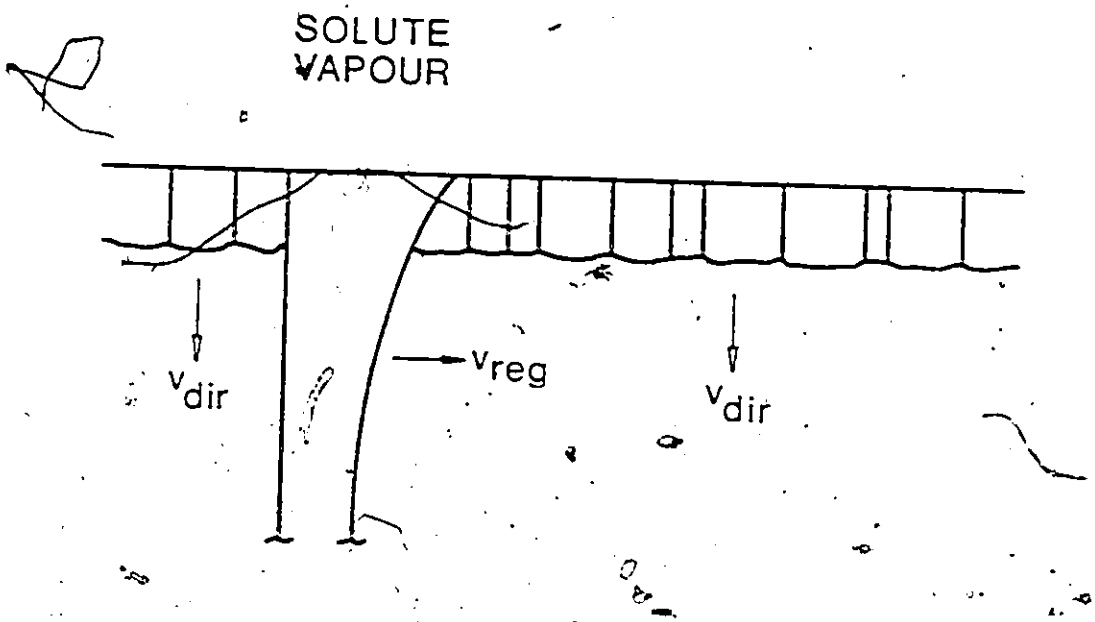

Figure 2.37 "Diffusion" Induced Recrystallization. A fine grain structure forms on the surface (v_{dir}) with the original boundaries still exhibiting regular GIGM (v_{reg}).

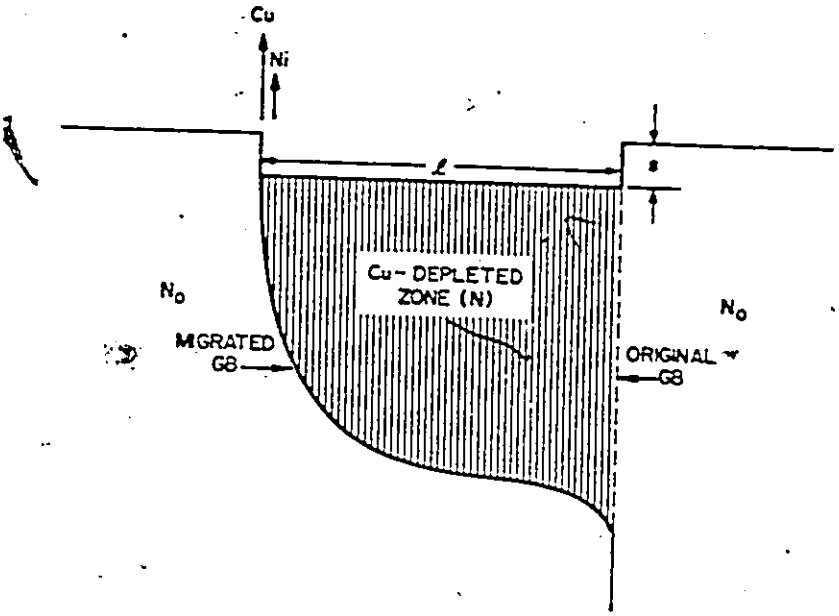

Figure 2.38 CIGM in the dealloying mode. A Cu-Ni alloy is sputtered with the Cu being preferentially removed faster than the Ni. The boundary migrates leaving a Cu depleted zone. The surface depression can be related to the removal of Cu. (ref. C13)

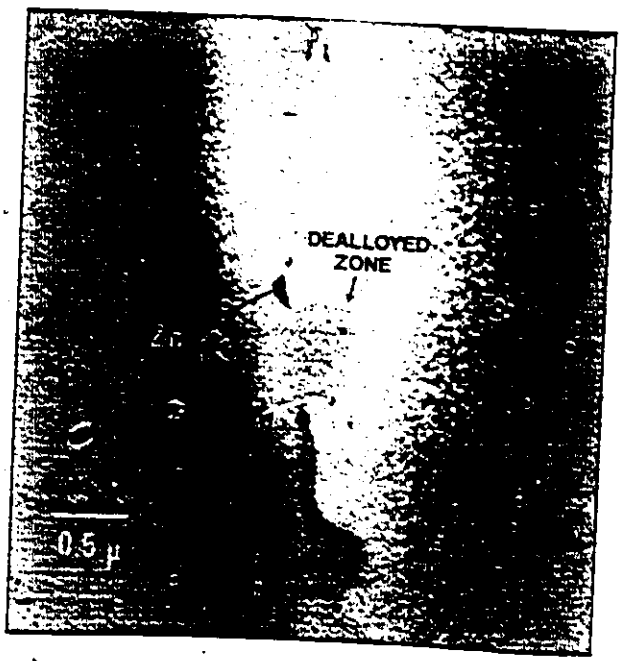

Figure 2.39 Dealloying CIGM as a precursor to discontinuous precipitation. Shown is an electron micrograph of dealloyed areas and precipitates of zinc. (ref. B3)

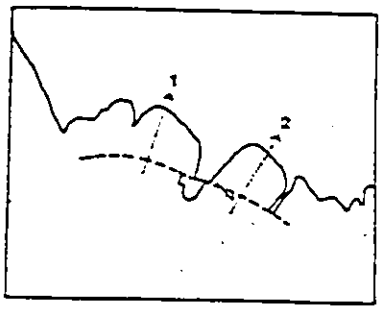

(a)

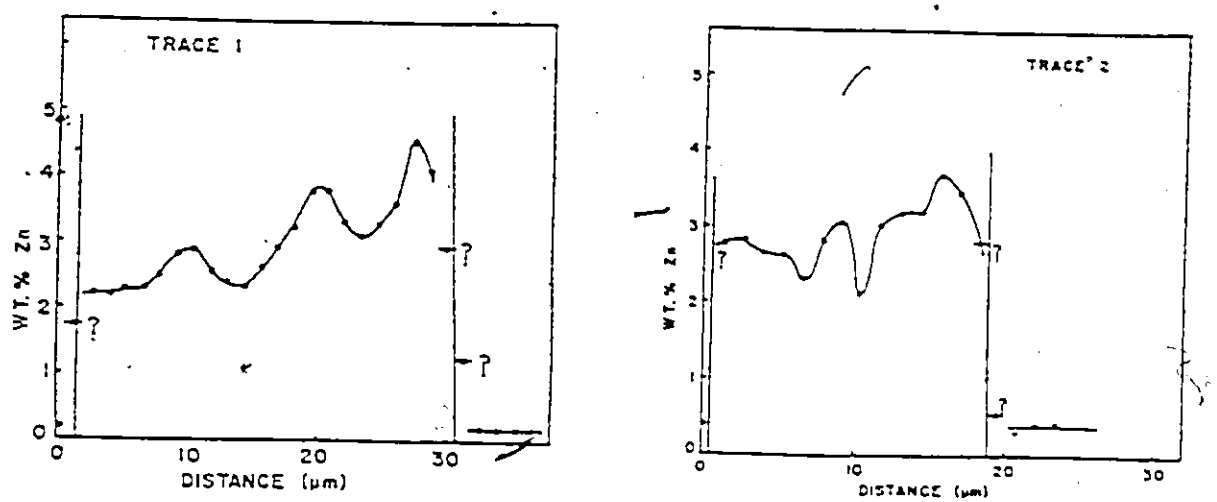

(b)

Figure 2.40 Nonuniform migration velocity is reflected in the concentration profiles in the alloyed grain. Figure (a) gives the boundary profile after migration and Figure (b) the concentration profiles of the region of interest. (ref. C10)

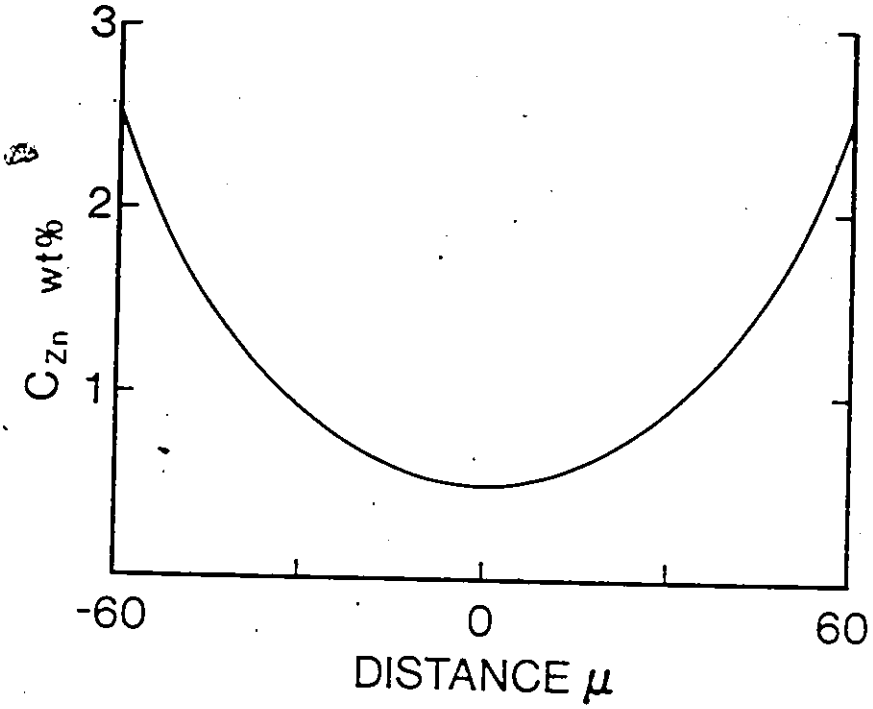

Figure 2.41 Concentration profile along the boundary for a finite thickness copper foil after exposure to a zinc vapour at 350°C. (ref. C43)

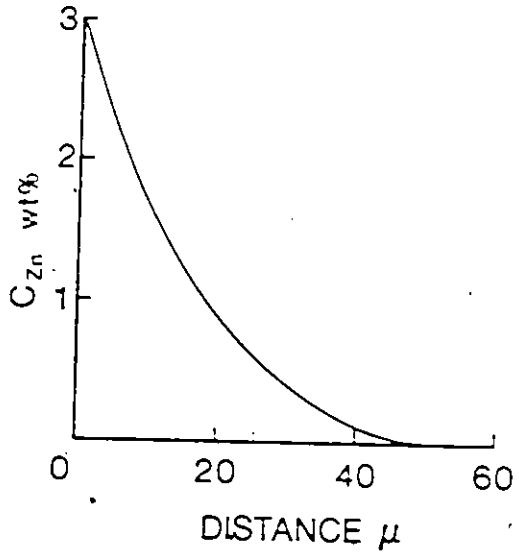

Figure 2.42 Concentration profile along a boundary in a thick copper foil after exposure to a zinc vapour at 400°C. (ref. C43)

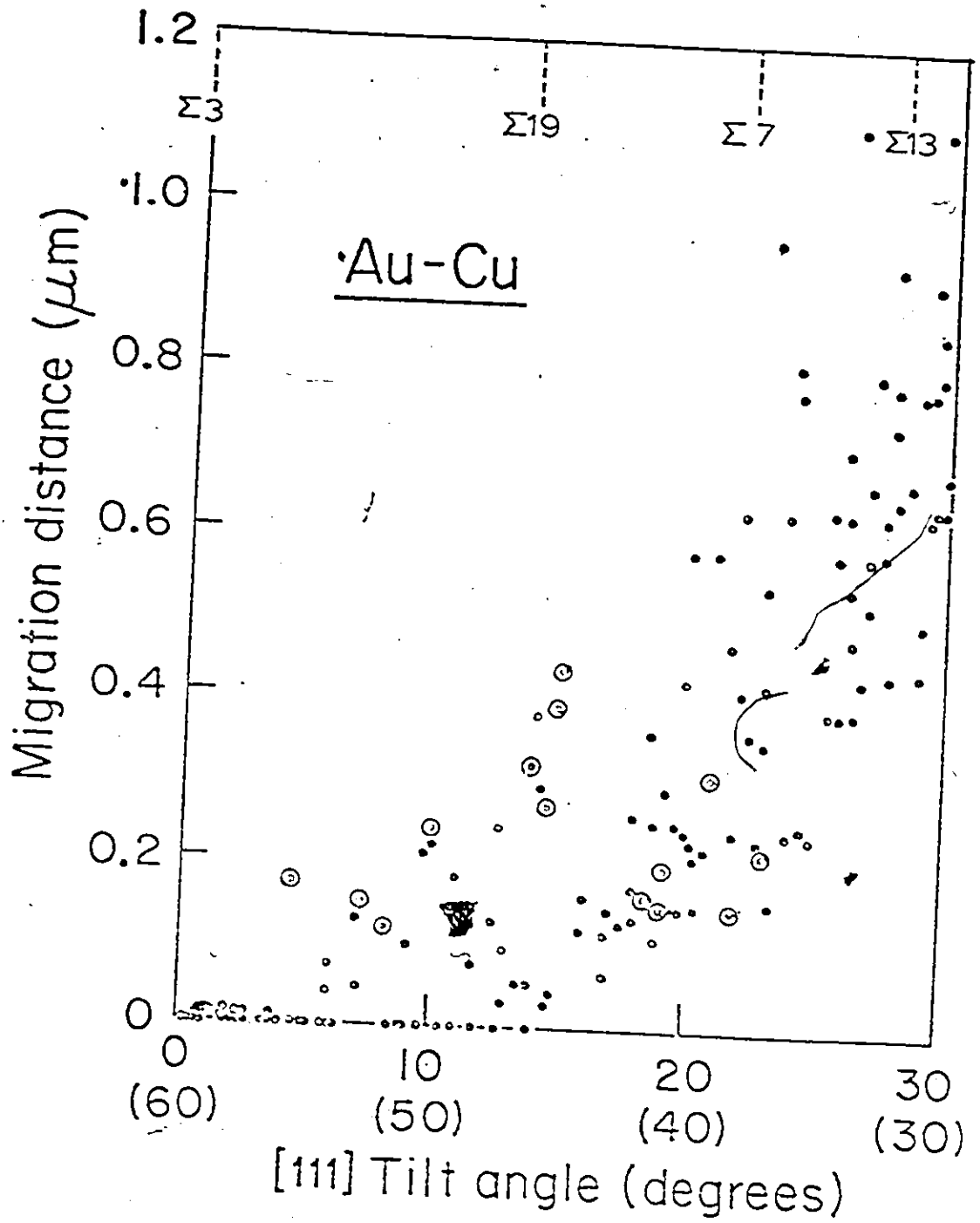

Figure 2.43 Migration characteristics for different orientations in the Au-Cu system for <111> tilt boundaries. Circled points denote strongly facetted boundaries. (ref. C48)

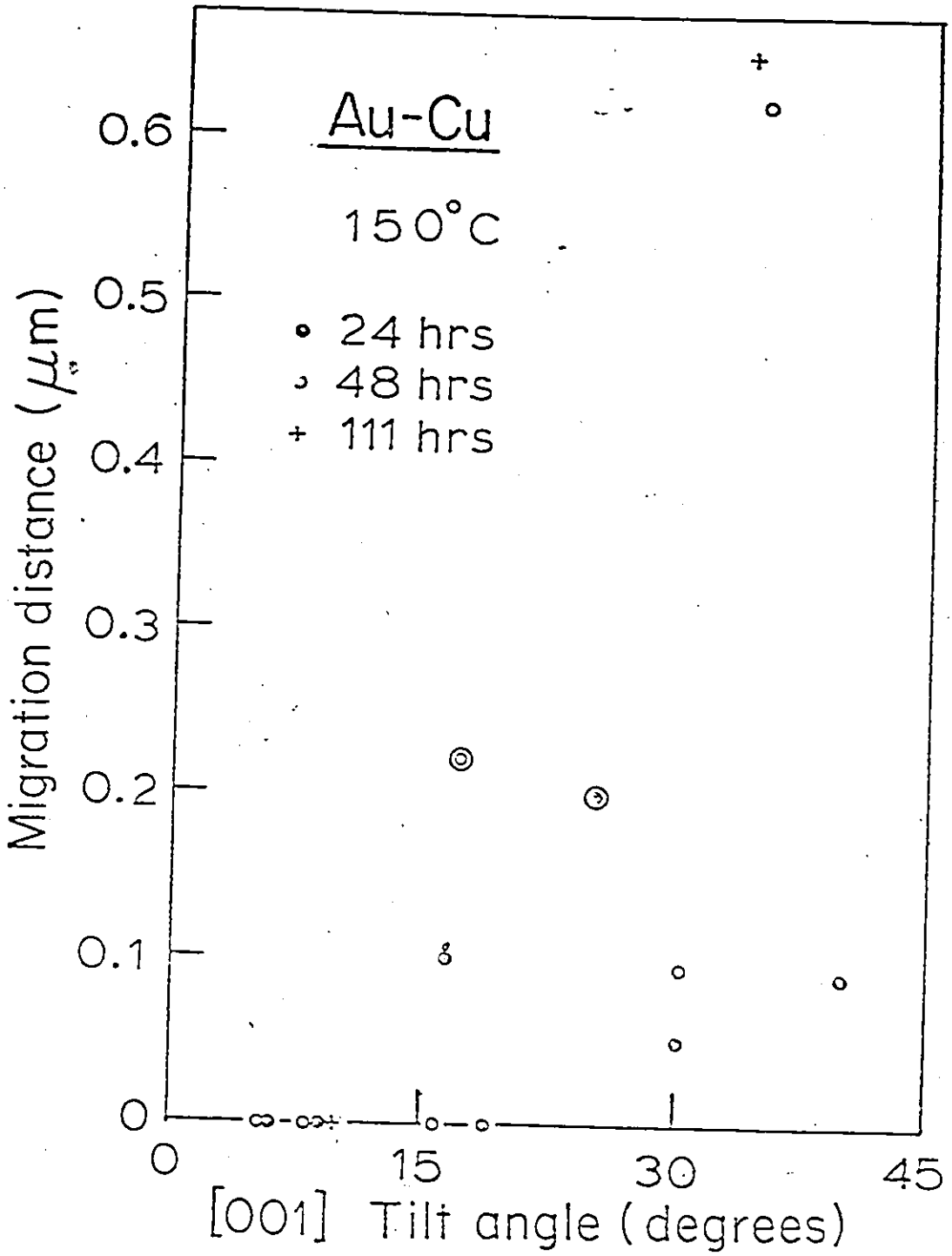

Figure 2.44 Migration characteristics for different orientations in the Au-Cu system for <100> tilt boundaries. Circled points denote strongly facetted boundaries. (ref. C48)

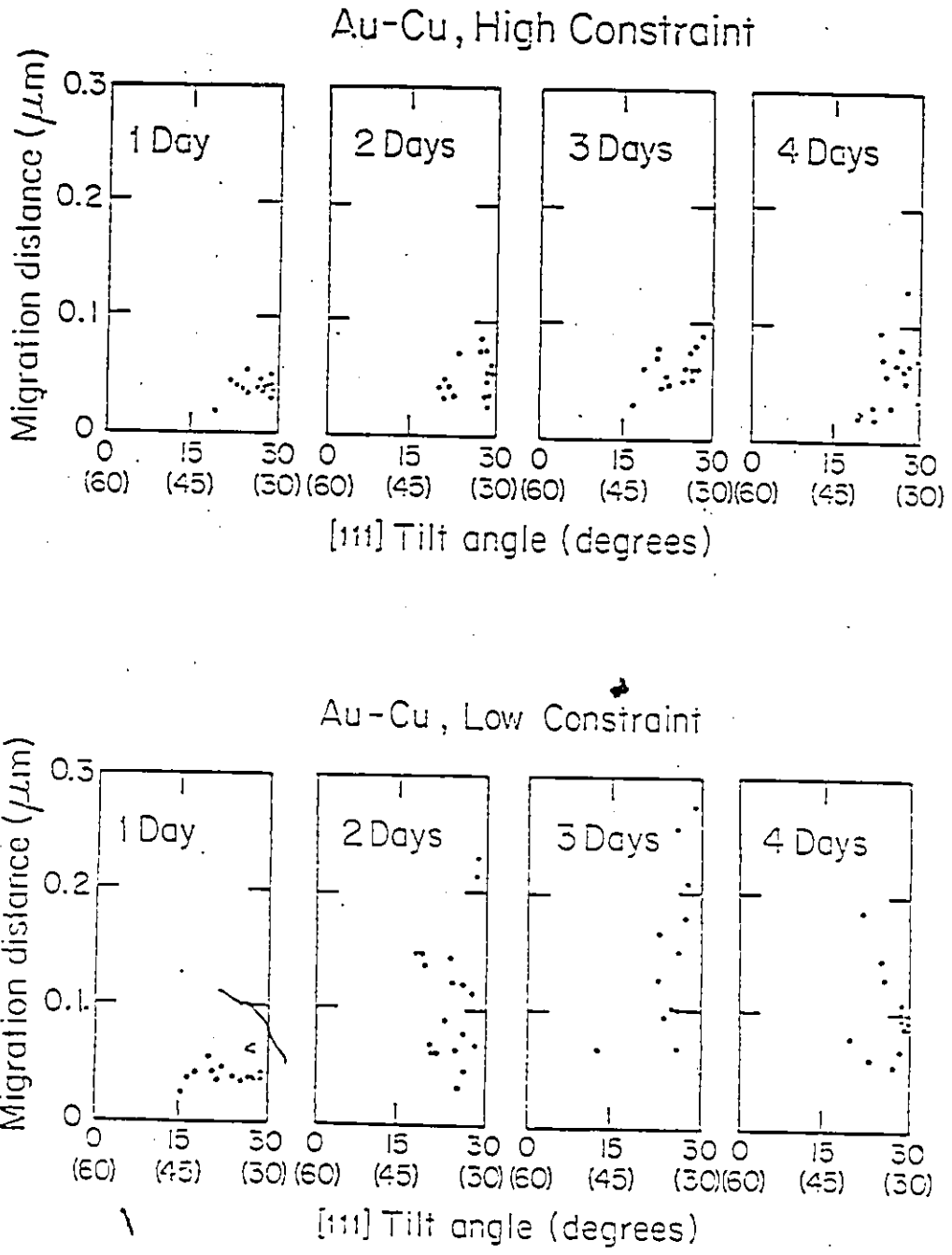

Figure 2.45 Migration under different levels of physical constraint for <111> Au tilt boundaries. High constraint samples are still attached to their substrates and have their overall migration reduced. (ref. C48)

2.3.2 Dislocation Climb Model of Chemically Induced Grain Boundary Migration

This model is based on the synchronous climb of grain boundary dislocations in response to a solute flux down it. Consider the simplified situation as shown in Figure 2.46. If the boundary flux J_b, the boundary velocity v and the concentration step across the boundary ΔC are known then the conservation condition that must apply is:

$$\text{Div } J_b = V\nabla C \tag{2.11}$$

The velocity of the boundary is related to the concentration difference across the boundary:

$$V = f(\nabla C) \tag{2.12}$$

This concentration difference is maximised if the solute penetration due to volume diffusion preceding the boundary is negligible or is dictated by the relationship:

$$g = D_v/v \tag{2.13}$$

where g is the atom spacing and D_v is the volume diffusivity.

Under these conditions, the diffusion (chemically) induced grain boundary migration (DIGM) model was proposed by Balluffi, Cahn and Pan (C29) and simultaneously by Smith and King (C30). The model suggests that a grain boundary Kirkendall effect was essential for DIGM as proposed by den Broeder (C19). The unequal fluxes of solute and solvent atoms in the grain boundary affects the grain boundary dislocations present. The dislocations act as flux divergence points which induce the boundary to migrate as indicated by equation 2.11.

The dislocation interacts with both the solute atoms and the vacancies produced by the diffusion process. The climb of the

dislocation by vacancies is shown in Figure 2.16 for a symmetric tilt boundary (angle = 36.9 degrees) for a pure edge grain boundary dislocation. If the dislocation climbs by adsorbing a vacancy, it will move three atoms from crystal II and add two atoms to crystal I destroying the vacancy in the process. Therefore, crystal II grows at the expense of crystal I. Dislocations of both edge and screw nature will both climb and glide.

If the dislocation interacts with a solute atom, climb of the dislocation also results. In this situation, the solute atoms are diffusing down the boundary faster than the solvent atoms. Solute flux divergence is achieved by the adsorption of solute atoms by dislocations. This results in the climb of the dislocation as shown in Figure 2.47. The climb results in the movement of the boundary into the pure crystal II and alloying crystal I. The adsorption and climb of the solute atom at the dislocation also incurs a depression of the solute concentration at that point. This then stimulates additional diffusion of solute along the boundary. Therefore, the process is self sustaining.

The detailed mass balance for the dislocation model is as follows; the flux of the species is given by Fick's laws using $D_a\delta$ and $D_b\delta$ as the intrinsic boundary diffusion coefficients as being:

$$J_a = -D_a\delta \, \partial C/\partial x \qquad J_b = -D_b\delta \, \partial C/\partial x \tag{2.14}$$

The net flux of atoms is assumed constant between grain boundary dislocations as they represent the only possible means of flux divergence. At the dislocations, the flux divergence produce a concentration gradient change which leads to the deposition of atoms given by:

$$-\nabla(J_a+J_b) = (D_b-D_a)\delta\ \partial C/\partial x \qquad (2.15)$$

which results in a dislocation climb velocity of:

$$V_d b_n = (D_b-D_a)\delta\ \partial C/\partial x \qquad (2.16)$$

where, b_n is the Burgers vector normal to the boundary plane. If the grain boundary dislocations possess a step height of u, then the climb of the dislocation by solute adsorption results in a layer u of crystal I being converted to $u + b_n$ of crystal II. The reverse is true if climb is due to vacancy adsorption. A mass balance for B atoms at the dislocations is:

$$\nabla J_b = V_d\ uC_i - V_d(u+b_n)C_{ii} = -D_b\delta\ \partial C/\partial x \qquad (2.17)$$

where V_d is the boundary velocity and C_i and C_{ii} are the compositions of crystal I and II respectively. This equation indicates that there is a compositional gradient change at the moving dislocation step. The compositional change across the grain boundary can be derived by solving equations 2.16 and 2.17 to yield:

$$C_{ii}-C_i = (u/b_n)\ [D_b/(D_b-D_a) - C_{ii}] \qquad (2.18)$$

Certain problems with the model become apparent immediately. The concentration step across the boundary is an unstable parameter. Large values of ΔC result in greater dislocation climb which promotes greater concentration gradients in the boundary and greater climb motion. The reverse is also true, as small ΔC can lead to cessation of migration. In addition to this difficulty is the lack of velocity dependence for determining the concentration step across the boundary and the total independence of the alloyed grain concentration upon the grain boundary concentration. Therefore, the expression describing the process as given

by equation 2.18 is too simple.

King (C31,C32) addressed these problems and formulated a model to eliminate them. Consider a grain boundary dislocation jog as shown in Figure 2.48. If the atomic volume in the grain boundary which differs from the volume in the lattice is O and the width is δ, then the volume of the zone (V_z) affected by the climb of the jog is:

$$V_z = hO/b \tag{2.19}$$

where h is the jog height and b the Burgers vector of a pure edge dislocation normal to the boundary plane. If one vacancy is adsorbed the volume is reduced by one atomic volume:

$$V_z = O\,(h/b - 1) \tag{2.20}$$

The final concentration of the zone is determined by the number of solute atoms provided by the boundary volume V_b and the matrix V_m:

$$V_b = \delta(hj + hl + jl) \tag{2.21}$$

$$V_m = V_z - V_b \tag{2.22}$$

then:

$$C_z = (V_b C_b + (V_z - V_b) C_m)/V_z \tag{2.23}$$

$$= C_m + \delta\,(hj + kl + jl)\,(C_b - C_m)/(O(h/b-1)) \tag{2.24}$$

given $dC_z = C_z - C_m$ and A_b the area of the boundary:

$$dC_z = \delta A_b (C_b - C_m)/(O(h/b - 1)) \tag{2.25}$$

The new relationship for the concentration of the affected zone now possesses the required dependence upon boundary cencentration and the topography of the grain boundary dislocation as compared to the Cahn-Balluffi equation 2.18.

The time dependent equation for diffusion as performed by King

using the method of Cahn and Balluffi must consider the dislocation spacing within the boundary. Performing a mass balance for B atoms along the boundary length r which is equal to the dislocation spacing yields:

$$(dC_b/dt) = D_b/r + [\delta 0\ (C_m-C_b)(D_b-D_a)/b_n r]\ \Delta(dC_b/dx) \qquad (2.26)$$

If the discontinuities resulting from the dislocations are smoothed out over the boundary length, the concentration discontinuity given by $\nabla(dC_b/dx)$ can be estimated by a second derivative by dividing this term by the dislocation spacing r to yield:

$$(dC_b/dt) = D_b/r + [\delta 0\ (C_m-C_b)(D_b-D_a)/b_n r]\ (d^2C_b/dx^2) \qquad (2.27)$$

Solution of this equation for steady state conditions yields a result independent of boundary concentration for both the King and Cahn-Balluffi formulations.

King has commented (C31) on the validity of the assumption of a continuous first derivative from which a second derivative can be derived and the assumption of a steady state being established. Consider first the assumption of a continuous first derivative. Two possible situations concerning the dislocation density can exist for a given boundary velocity. The first is closely spaced, slow moving dislocations and the second is widely spaced, fast moving dislocations. For the first situation, the concentration discontinuity that the dislocations produce (a large square well on a continuous slope) can moderate before the next dislocation can climb through. Under these conditions, the second derivative is valid and equation 2.27 is valid. However, if the second situation is dominant, then the concentration discontinuity will not moderate before the next climb event. Then, equation 2.26 is the only expression valid in this situation. The assumption of a continuous first

derivative removes the dependence of the solution upon the dislocation spacing. For a steady state situation to be established, the dislocation spacing must be constant and uniform. However, since the spacing will be affected by the concentration gradient in the boundary and since the gradient is finite, the spacing may never acheive uniformity and constancy. Therefore, the steady state and the second derivative may not exist.

For the Cahn-Balluffi model or the King reformulation to be tenable, there must be an adequate supply of grain boundary dislocations. The source of dislocations as previously described (All) can be a result of the nonequilibrium concentration of vacancies in the grain boundary due to unequal solute and solvent fluxes, sessile grain boundary dislocations forming growth spirals or the intersection of the surface with the boundary itself.

Referring to equation 2.17, if the original grain boundary concentration $C_i \doteq 0$ and $D_b/D_a \gg 1$ then equation 2.18 becomes:

$$\Delta C = C_{ii} - (b_n/u)/(1-b_n/u) \qquad (2.28)$$

For normal high angle grain boundaries, the ratio b_n/u is usually small producing concentration steps across the boundary of acceptable levels (i.e. if $b_n/u=.1$ then $\Delta C=.1$). However, high coincidence boundaries have high values of b_n/u producing large concentration steps which may not be allowable. Such boundaries may not be able to migrate as suggested by experimental observations.

It is assumed that the driving force which causes the dislocation to climb originates from the discontinuous solute concentration change across it. Therefore, it should be possible to

evaluate a chemical potential change across the dislocation for the solute. However, if a grain boundary Kirkendall effect is present, den Broeder stated (C9), it should be possible to evaluate a vacancy chemical potential changes across the dislocation. Therefore, the total climb force on the dislocation is:

$$du_s + du_v = du_{disl} \qquad (2.29)$$

At velocities and temperatures, where the penetration of solute ahead of the moving boundary is small. ($D_v/v < .5$ nm), both components contribute to the climb process. However, when solute penetration is substantial, the concentration step across the boundary is removed and therefore, as suggested by den Broeder, the vacancy component only is active.

In the Cu-Ni experiments performed by den Broeder (C9), Cu is the faster diffusing species and solute penetration ahead of the boundary is substantial. Therefore, the vacancy chemical potential term of equation 2.29 will dominate and a vacancy supersaturation will occur in the Cu grain boundaries and an undersaturation in the Ni grain boundaries. According to den Broeder's model, the migration in the Cu boundaries will be controlled by the migration energy of the vacancy only (Em). However, the Ni boundaries, being undersaturated, must create and move the vacancies in order to migrate (Em + Ec). Some evidence to substantiate this model was found by den Broeder as the activation energies for the Cu grain boundaries was only .59 ev as compared to the Ni grain boundaries' activation energy of 1.64 ev.

Hillert (C44) has discussed certain objections concerning the dislocation climb model description of this process. Firstly, the model is highly sensitive to boundary structure and should demonstrate a

higher dependence of migration velocity upon boundary orientation than what has been observed. The nucleation of new grains is also inconsistent with the climb model as no boundaries are present initially and a definite amount of energy must be comsumed in order to nucleate them. Oscillatory migration whcih is regularly observed is also inconsistent with the climb model since once migration direction is selected, the dislocation's Burgers vector is also selected.

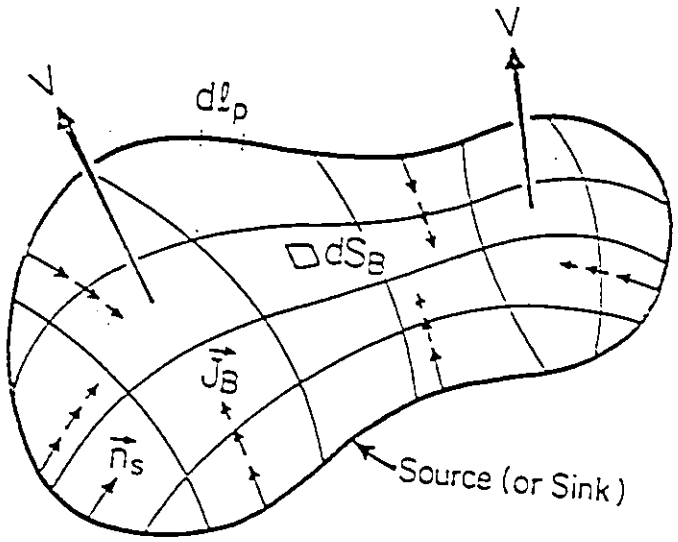

Figure 2.46 Diffusion geometry for a boundary migrating with a solute source or sink at its perimeter. The smaller arrows denote local boundary flux divergences and the larger arrows boundary velocity. (ref. C23)

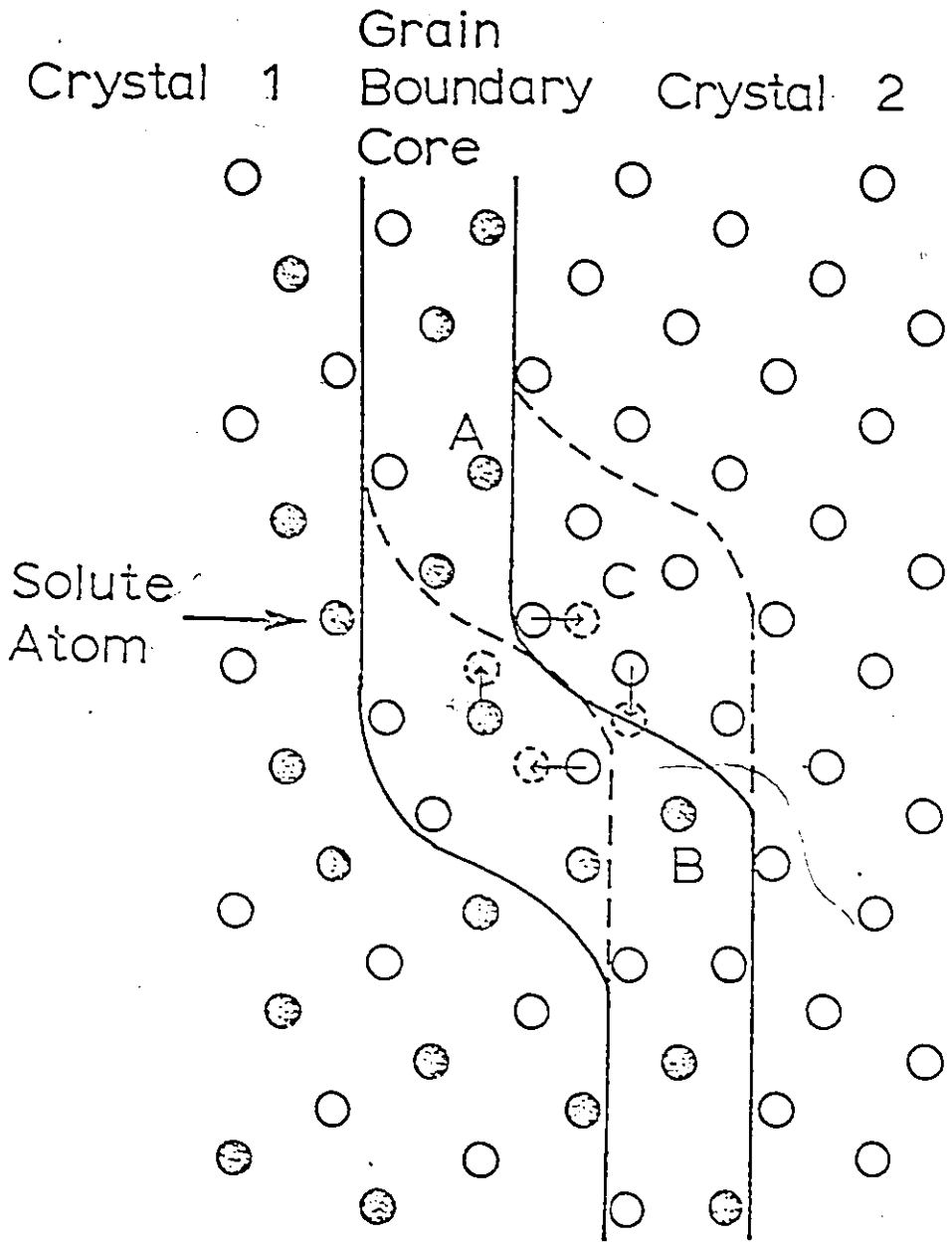

Figure 2.47 Diagram demonstrating atomic rearrangement due to climb of grain boundary dislocations by vacancy adsorption for a <100> tilt boundary. (ref. C48)

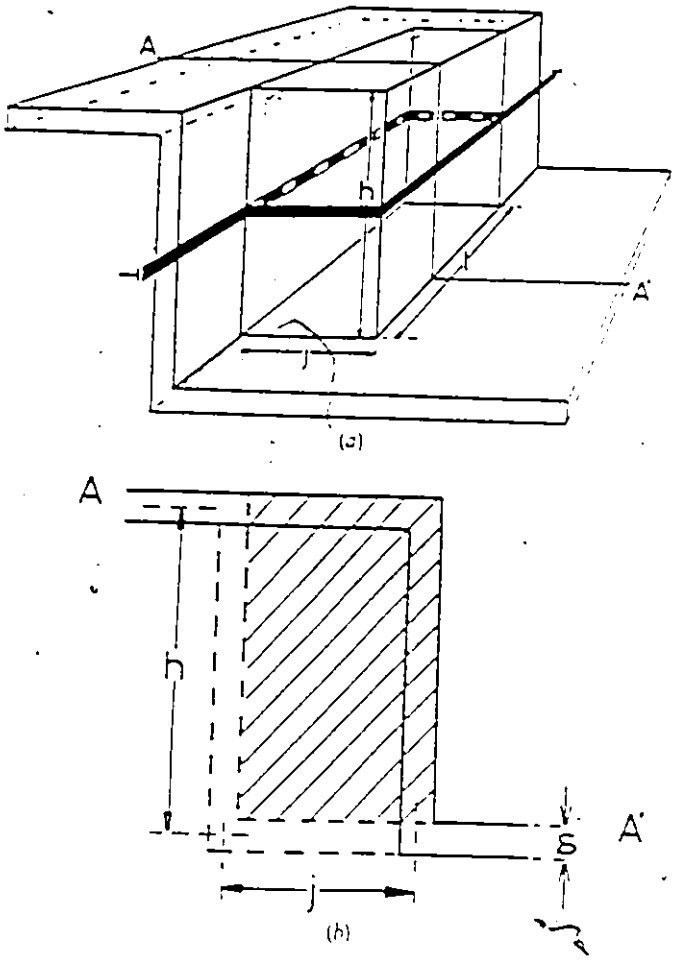

Figure 2.48 Grain boundary dislocation jog geometry. (a) is a sketch showing the dislocation line and boundary plane positions. The full line is before vacancy adsorption and the broken line is after adsorption. (b) is a cross section for which a mass balance is performed. (ref. C31)

2.3.3 Chemical Driving Forces in CIGM

The concept of the grain boundary being driven by a chemical force was introduced by Hillert and Purdy (C1). In order for a boundary to be chemically driven, there must be a concentration step across the boundary. Then, there is a decrease in free energy as material from one grain is transported to the other across the boundary. As stated in a previous section, the total free energy produced is not dissipated totally in moving the boundary as there are many other processes occurring simultaneously to dissipate this energy. The resulting boundary velocity is assumed to be linearly related to the free energy remaining.

Hillert has analysed the fine grained surface growth (C2) after a diffusion induced recrystallization (DIR) event in the Fe- Zn CIGM system using the concept of a chemically driven boundary. The geometry assumed is shown in Figure 2.49. The vertical boundaries are assumed stationary and are the solute path for the horizontal boundaries which do migrate. A linear force - velocity relationship of:

$$dL/dt = v = M\Delta G_m/V_m \qquad (2.30)$$

is assumed, where v is the boundary velocity, dL/dt is the thickening rate of the layer, M is the grain boundary mobility, V_m the molar volume and ΔG_m the free energy available to drive the boundary. Assuming negligible volume diffusion penetration ahead of the boundary, the full concentration step is present across the boundary. In addition, it is assumed that the full amount of the chemical energy available is dissipated in moving the boundary. Assuming the free energy can be described using dilute solution behaviour:

$$\Delta G_m = RT\, X_{zn} \qquad (2.31)$$

which yields the growth rate as:

$$dL/dt = MRT\, X_{zn}/V_m \qquad (2.32)$$

where X_{zn} is the concentration of zinc just behind the boundary. If the diffusivity of the migrating horizontal boundaries is greater then the stationary vertical boundaries, then the mass flow will be controlled by the vertical boundaries. This assumption is justified by the planar form of the horizontal boundaries and the constant zinc concentration in the alloyed layer. Therefore, the mass transfer down the vertical boundaries whose grain diameter is s is given by:

$$(dm/dt) = \pi s\, D_b \delta\, (x^o_{xn} - x^b_{xn})/2V_m L \qquad (2.33)$$

The mass of zinc consumed as the horizontal boundaries migrate is given as:

$$(dm/dt) = (dL/dt)\, \pi s^2\, x^b_{zn}/4V_m \qquad (2.34)$$

Combining equations 2.32 to 2.34 yields a partial differential equation whose solution is of the form:

$$J = 2\lambda + \lambda\sqrt{1+\lambda^2} + \ln(\lambda + \sqrt{1+\lambda^2}) \qquad (2.35)$$

where:

$$J = 4t\, (MRTx^s_{zn}/V_m)^{3/2}/(D_b\delta)^{1/2} \qquad (2.36)$$

$$\lambda = L\, (MRTx^s_{zn}/V_m D_b \delta)^{1/2} \qquad (2.37)$$

For small values of L, then $J = 4\lambda$ and for larger values $J = \lambda^2$. These functional dependences are shown in Figure 2.50b with the experimentally determined dependences shown in Figure 2.50a. The line $\lambda = f(J)$ resembles the 600°C curves or higher and the line $\lambda = f(\sqrt{J})$ resembles the curves of 550°C or lower. Using the 600°C curve to estimate the boundary diffusivity of the assumed stationary vertical boundaries to the model

yields values three orders of magnitude greater than expected for stationary boundaries. However, it was found experimentally, that the vertical boundaries did migrate and therefore, the calculated boundary diffusivity was in agreement with other migrating boundary diffusivity calculations. The calculations for the fine grain layer growth shows success, although limited, with the concept of a boundary experiencing the effects of the full chemical force upon it.

It was pointed out by Cahn et. al. (C10) that a large portion of the chemical energy can be dissipated by a large amount of volume diffusion ahead of the moving boundary. Therefore, the lowest possible value of the chemical driving force is the chemical driving force left after coherency strain effects are accounted for. The coherency strain is produced by solute diffusing into the grain ahead of the moving boundary and dilating the lattice. Then, the two grain surfaces will be in equilibrium, one with the coherency energy present due to solute dilation and the other strain free as shown in Figure 2.51. Therefore, a constrained equilibrium will be established. The free energy diagram for this situation is given in Figure 2.52 as described by Hillert (C44). The free energy curve for the strain free grain is given by G_a and the free energy curve for the coherently strain grain is G_c. The coherent grain possesses an additional strain energy term given as:

$$w = E V_m \eta^2 (x_1 - x_c)/(1-\nu) \qquad (2.38)$$

where E is Young's modulus, V_m is the molar volume, η is the misfit parameter, ν is Poisson's ratio, x_1 is the common composition and x_c is the coherent composition. Assume that the overall composition of both grains is x_1. If an incoherent nucleus forms of composition x_2 then the

coherent grain will have a composition of x_c. The alloyed region of composition x_2 can draw material from the coherent grain of composition x_c with a decrease in free energy given by $G_a - G_c$. If the misfit parameter were larger, the coherency free erergy curve would be steeper and the equilibrium concentration x_c would approach x_1. It is conceivable that a small coherency strain energy could give rise to a large compositional difference across the boundary.

The driving force is chemical in nature and the coherency effects define its value. Assuming ideal solution behaviour, the actual value of the driving force can be estimated. The expressions for the free energy curves for the incoherent and coherent grains are as follows:

$$G_a^{\alpha} = (1-x_2)G_a^{\circ} + x_2 G_b^{\circ} + RT\,[(1-x_2)\ln(1-x_2) + x_2 \ln x_2] \quad (2.39)$$

$$G_a^{coh} = (1-x_c)G_a^{\circ} + x_c G_b^{\circ} + RT\,[(1-x_c)\ln(1-x_c) + x_c \ln x_c] + E\,V_m\,\eta^2(x_1-x_c)^2/(1-\nu) \quad (2.40)$$

the chemical potential for each species in each phase is given as:

$$G_b = G_b^{\circ} + RT \ln x_2 \quad (2.41)$$

$$G_a = G_a^{\circ} + RT \ln (1-x_2) \quad (2.42)$$

$$G_b = G_b^{\circ} + RT \ln x_c + E\,V_m\,\eta^2(x_1-x_c)(x_1+x_c-2)/(1-\nu) \quad (2.43)$$

$$G_a = G_a^{\circ} + RT \ln (1-x_c) + E\,V_m\,\eta^2(x_1-x_c)(x_1+x_2)/(1-\nu) \quad (2.44)$$

assuming $1-x_2 = 1$ and $1-x_c = 1$ and solving for x_c yields:

$$\frac{x_1-x_c}{x_1-x_2} = \left(\frac{RT}{2x_2} + \frac{E\,V_m\eta^2}{1-\nu}\right)\Big/\left(\frac{RT}{2x_2}\right) \quad (2.45)$$

assuming a small mismatch parameter and $x_c \sim x_2$ yields the driving force as:

$$\Delta G_a = E V_m \eta^2 (x_2 - x_1)^2/(1-\nu) \qquad (2.46)$$

The equation given represents the maximum force available for the boundary to migrate under the conditions of large solute penetration ahead of the boundary. This force will not be exclusively dissipated in moving the boundary. It also may be dissipated in capillarity or solute drag effects depending upon the velocity. It is possible that only a fraction of the full coherency derived chemical driving force is developed across the boundary. Such conditions are considered in the discussion section of this thesis.

Two forms of energy are present near the boundary, the chemical energy of the concentration step and the strain energy of the coherent layer. Under steady state conditions, the strain energy is constant since the concentration gradient ahead of the boundary is constant. However, if an external stimulus resulted in the boundary increasing speed, both the concentration profile and the strain energy ahead of the boundary would decrease. The remaining strain energy could be recovered by the boundary to increase the driving force. Therefore, the driving force could recover the strain energy and be driven by a force a maximum of twice the chemical force as given in equation 2.46.

The concept of a chemical force derived from coherency strains driving an interface has been tested experimentally in a set of sintering experiments by D. Yoon et al (C40,C41,C46,C47). The conditions are almost identical to CIGM under high solute penetration conditions except the boundary is replaced with a thin liquid film and is known as

liquid film migration (LFM). The similiarities are shown in Figure 2.53 for LFM in the W-Ni system. The best verification of the coherency strain model is to be able to vary the misfit parameter as described in equation 2.46. If the model is correct, if the misfit parameter can be controlled and set to zero, the migration velocity should also drop to zero even though the free energy decrease due to alloying is still finite. An experiment of this nature was performed by D. Yoon et. al. (C46) in the Mo-Ni-Fe ternary system. A ternary system was chosen since the misfit parameter can be controlled and the misfit can stay constant over a wide range of compositions. By varying the Fe concentration from 0 to 3 at%, the coherency strain varies from compressive to tensile respectively. The results of the experiment are shown in Figure 2.54. The misfit parameter was estimated using the mixture rule. The result is consistent for a chemical driving force which is coherently derived. The similiar effects of a ternary solute in adjusting the misfit parameter is also observed in solid systems indicating coherency forces also drive grain boundaries.

An additional question considered by D. Yoon et. al. is the initiation mechanism and the importance of elastic anisotropy for LFM. During the initial stages of LFM, the solute penetrates equally into each grain so that both diffusion profile are symmetric. The problem is what mechanism causes the breaking of this symmetry to form the necessary condition to cause LFM. As shown in equation 2.46, the elastic modulus is an important quantity. In most real systems, the modulus is actually anisotropic and therefore, Yoon defines the anisotropic modulus Y as:

$$Y = E/(1-v) \qquad (2.47)$$

Y is now a vector quantity and is essential in describing the initial stages of LFM. From equation 2.46, migration should proceed into the higher stressed grain which can be the result of the difference in anisotropic modulus Y between the two solid grains and stress relaxation in one of the grains.

Since the strain energy is greater in the grain with the larger Y, the liquid film would be expected to migrate into that grain first as thermodynamics predict. However, the second mechanism states that since this particular grain has the higher Y, it should be easier to nucleate dislocations in this coherently strained volume and relax the stress. The relaxation however cannot occur until a critical value of layer thickness has built up. It is assumed that a dislocation nucleation event is present as the critical layer thickness represents a critical stress for the existence of dislocations not their nucleation. Such stress relaxation could conceivably not be uniform along the boundary and result in nonuniform migration.

The discussion of a chemically driven grain boundary has to this point ignored grain boundary structure. Two possible mechanisms are possible which can resolve the motion of a boundary with a chemical driving force across it. The first mechanism ignores all boundary structure components and relies on purely random atom jumps across the boundary. Such a mechanism is suggested by Turnbull (A20). The second mechanism as proposed by Li and Rath (C27) acknowledges the existence of boundary structure components and utilises them as an integral part of the migration mechanism.

In order to promote migration and a compositional change, there must be an asymmetrical exchange of atoms on each side of the boundary. This can occur in a random manner as in Turnbull's model or it can also occur with the aid of boundary structure components. The first of these components is a structural ledge. The motion or climb of such a ledge will induce boundary migration. Assuming a chemical potential exists across the ledge, then the exchange of solvent and solute atoms from each face of the ledge will be different. In this situation, the ledge will move due to a net flux of atoms at its two faces.

An alternate mechanism for asymmetric atom deposition is the direct deposition of B atoms on one face with the subsequent dissolution of A atoms from the other face. In both cases, a chemical potential is developed across the ledge which helps to promote further deposition.

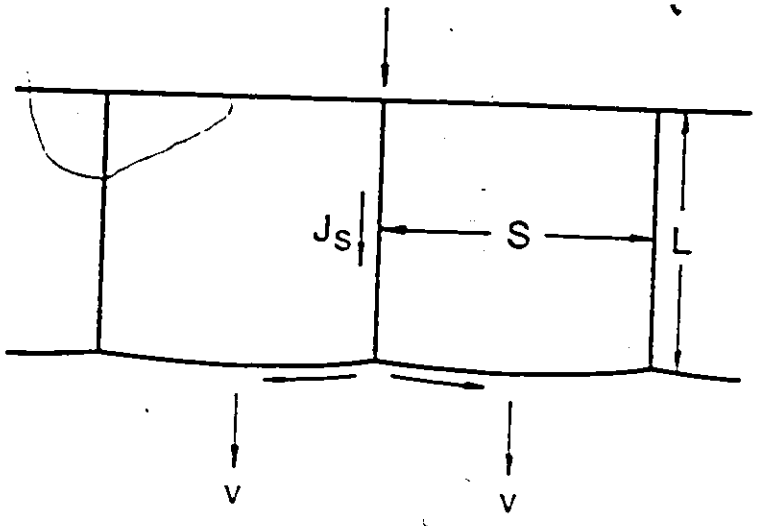

Figure 2.49 Geometry of the fine grained surface layer growth. Refer to text. (ref. C2)

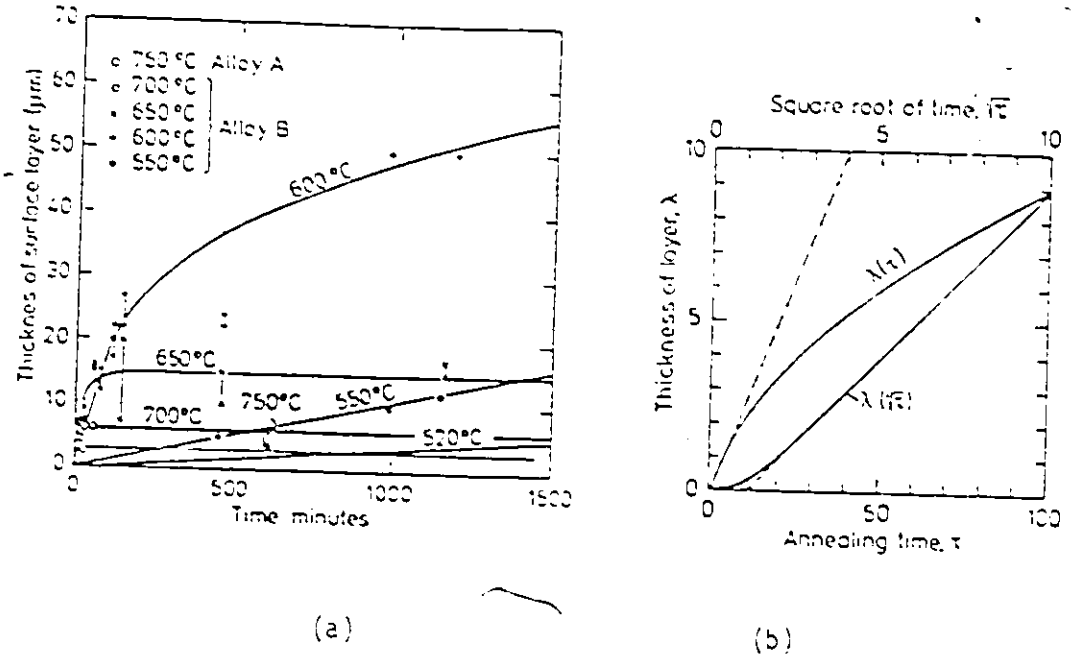

(a) (b)

Figure 2.50 (a) Experimentally obtained growth kinetics and (b) the theoretically predicted kinetics. It is suggested that the growth is limited at high temperatures in (a) due to the appearance of abnormal grain growth. (ref. C2)

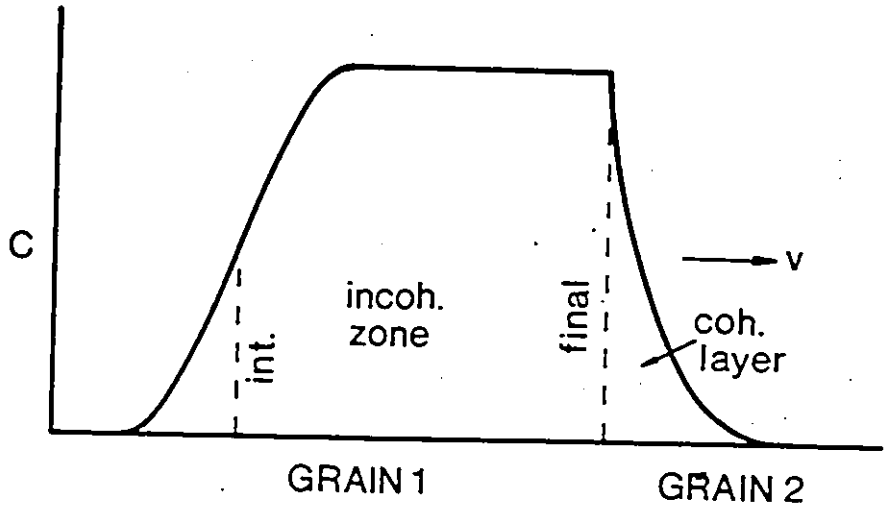

Figure 2.51 Compositional profile of CIGM with large lattice penetration. The coherent strain energy is in grain 2 in the thin layer where the solute has passed. Grain 1 is unstrained.

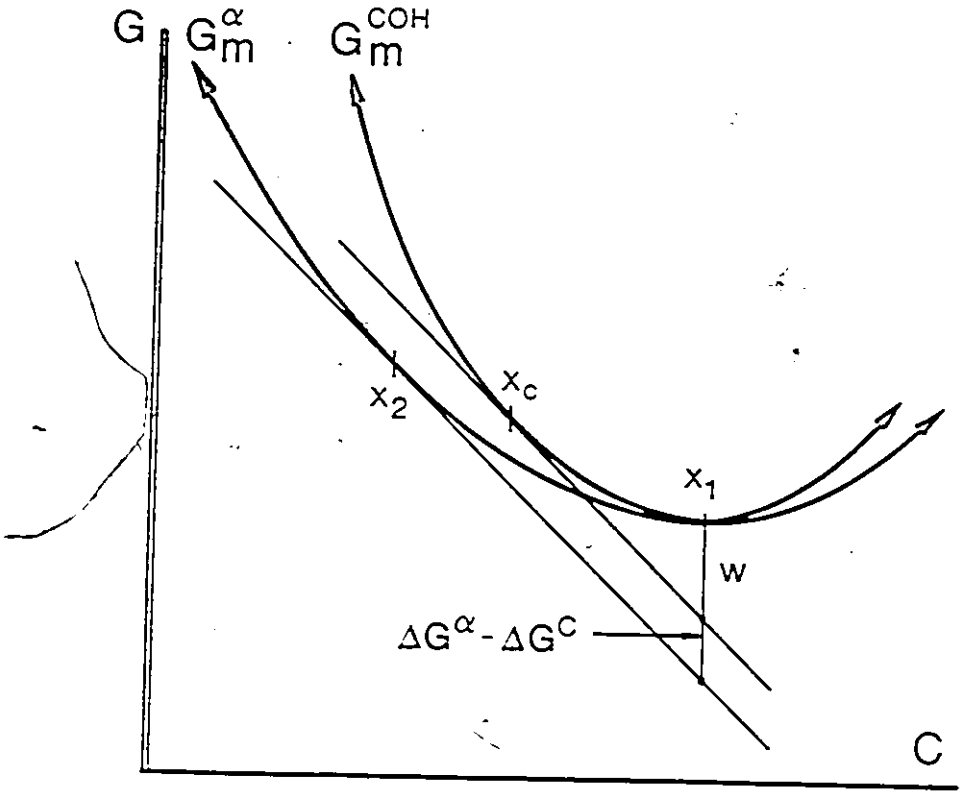

Figure 2.52 Free energy diagram of a system with coherency effects present. (ref. C44)

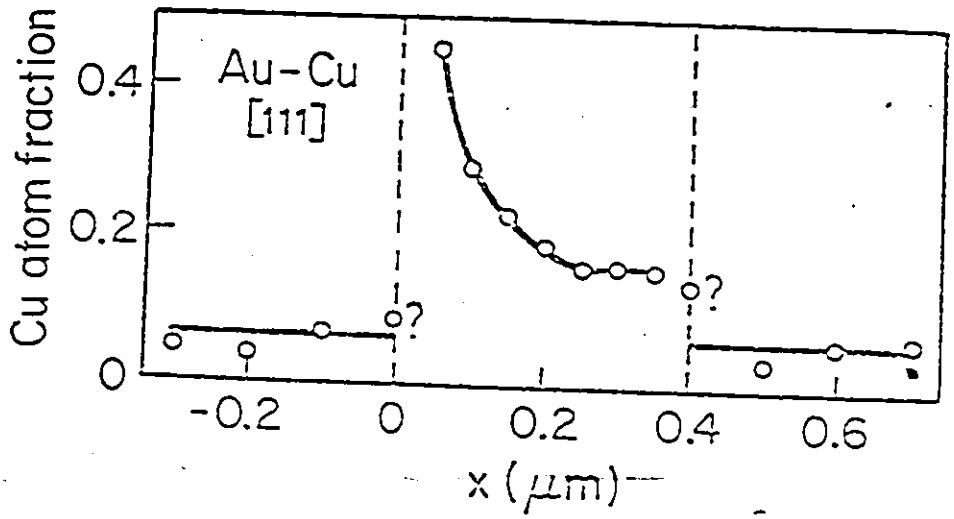

(a)

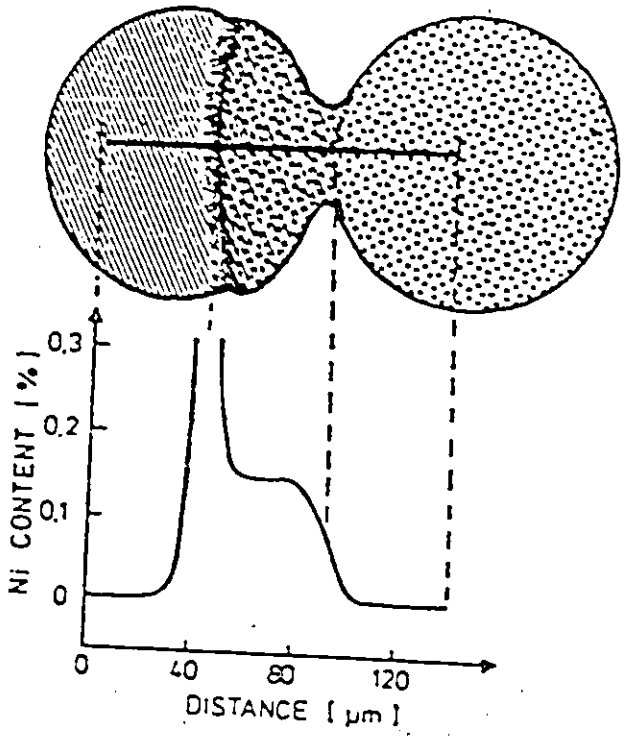

(b)

Figure 2.53 (a) Comparison of CIGM in the Au-Cu system (ref. C7) and (b) LFM in the W-Ni system (ref. C40). Due to the finite liquid layer thickness probe studies can be made as to its concentration.

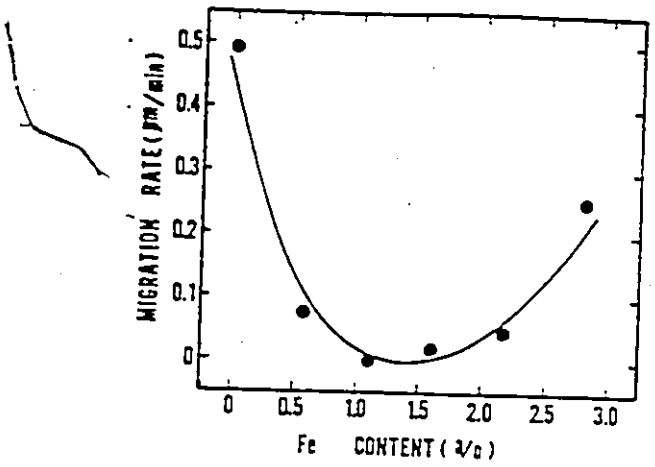

(a)

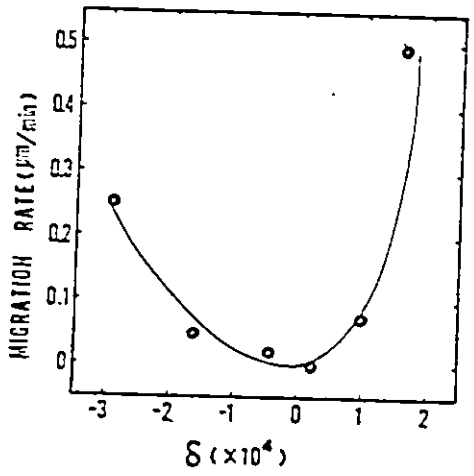

(b)

Figure 2.54 Results of the coherency control experiment. (a) is the migration rate dependence upon the amount of Fe added. (b) is the migration rate dependence upon estimated misfit parameter changes. (ref. C46)

CHAPTER 3

EXPERIMENTAL PROCEDURES

3.1 Alloy Diffusion Couple Preparation

3.1.1 Choice of Alloy Systems

A number of binary alloy systems was chosen for investigation. In most cases, the system chosen possessed a large solid solubility (greater than 5 at. %) for the solute. The exception was the Ag-Cu system which was chosen for examination since the diffusivities of each species in a matrix of the other are similiar in value. A variety of different systems was chosen in order to test the universality of the chemically driven boundary. A list of the systems studied is given in Table 3.1 .

3.1.2 Sample Preparation and Heat Treatment

All samples were prepared in a similiar manner. The base materials were thin foils approximately 0.2 to 0.4 mm thick which where polished on one side only with a minimum of one micron diamond compound. The foils were then individually sealed in Vycor tubes which were then evacuated. An extensive anneal was then performed in order to grow very large grains (typically 4 to 6 hours at 800 to 900°C). The foils were then carefully removed in order to minimize cold working the foil. The solute was then electroplated onto the polished surface using bath compositions as described in Appendix A. After the plating procedure, the diffusion couples were then resealed into evacuated Pyrex tubes. The

final heat treatment was performed in a standard tube furnace for the temperatures and times as indicated in Table 3.1 . After the final heat treatment, the solute plated surfaces were carefully removed mechanically and then polished as finely as possible. The samples were then prepared for optical examination using the etchants as described in Appendix B.

TABLE 3.1 BINARY ALLOY SYSTEMS

MATRIX	SOLUTE	TEMP°C	TIME hrs	SOLUBILITY
Ag	Cu	400 500	408 408	Limited
Ag	Mn	400 500	216 144	Limited
Ag	Pd	400 500	216 144	Unlimited
Au	Ni	600	75	Unlimited
Au	Pd	500	144	Unlimited
Cu	Mn	400 500	216 144	Limited
Cu	Pd	400	216	Unlimited
Pt	Pd	500 800	408 48	Unlimited

In addition to the optical examination, chemical information was also obtained using a Philips 515 SEM with a Kevex 7000 energy dispersive analyser using the standardless ZAF correction method when concentration levels and non overlapping spectral line allowed.

3.2 Measurement of the Migration Characteristics in the Al-Zn System

The measurements of the chemically induced grain boundary migration characteristics in the Al-Zn system are examined in more detail in order for comparisons to be made with discontinuous precipitation within the same system.

3.2.1 Bulk Samples

The preparation of the Al-Zn diffusion couples differs from the previous diffusion couples due to the tenacious oxide film covering the sample. The samples used for bulk analysis where in either a wire or foil form. The wire diameter ranged from 0.17 to 0.25 mm and the foil thickness ranged from 0.25 to 2.0 mm. All samples were sealed in evacuated Pyrex tubes and annealed for 4 to 6 hours at 500°C in order to develop a large grain size. The mean grain size was of the order of 0.1 to 0.2 mm in diameter. After carefully removing the very soft samples, zinc was then deposited onto the surface using the following procedure:

<1> Sodium Hydroxide Pickle (50%) 1 min

<2> Nitric Acid Pickle (50%) 1-2 min

<3> Zinc Strike 5 min (Appendix A)

<4> Wash

<5> Zinc Plate (Appendix A)

The diffusion couples were then again sealed into evacuated Pyrex tubes and annealed for times ranging from 2 to 17 days at temperature from 100 to 220°C. The samples were then sectioned and etched (Appendix B) and then examined optically. In addition, chemical composition was also obtained using the Kevex 7000 system.

3.2.2 Surface Samples

The sample preparation for these special Al-Zn diffusion couples is similiar to the procedure already presented. The foils are thinner than the previous samples (0.1 to 0.2 mm thick) and are polished on one side only. A mechanical polish using 6 micron polishing compound was first preformed. The foils were then annealed as previously described. Since in this instance, the foils were considerably thinner, they were temporarily mounted polished side up onto glass slides in order to minimize cold working effects. The samples were then electropolished using a 10% Nitric Acid - Methanol electrolyte. The foil is then removed from the slide, remounted with the polished side downwards and then zinc was electroplated on to the unpolished side using the methods previously described. The foils were again sealed into evacuated tubes and annealed. The surfaces were examined optically in both the etched and unetched states.

3.2.3 Externally Stressed Samples

This set of experiments was intended to examine the effects of an externally applied stress on the migration characteristics. The first experiment applied a tensile stress to a zinc plated wire sample as shown in Figure 3.1. A control sample was always included with the stressed sample for comparison purposes. The second experiment applied a bending moment to a Al-Zn diffusion couple strip. Again, a control strip was also present. All samples were then sectioned, etched and optically examined for the extent of migration.

3.3 Quantitative Boundary Migration Measurement

For certain samples, the treatment temperature is high enough such that volume diffusion is appreciable. In this particular instance, the concentration profile deviates from the ideal profile (rectangular) to a profile as shown in Figure 3.2. The migration distance must be corrected for this volume diffusion penetration so the true migration distance can be determined. The concentration profile in front of the migrating boundary follows the expression:

$$C = C_o \exp(-vx/D) \tag{3.1}$$

Where, v is the boundary velocity, D is the volume diffusivity, C_o is the equilibrium concentration and x is the distance from the moving boundary. Then, the true migration velocity can be deduced as:

$$v = (m-c)/t \tag{3.2}$$

Where m is the measured distance and c is the correction distance. Using this expression and the previous relationship, the correction distance can be found to be:

$$c = [m - \sqrt{(m^2 - 4DT\ln 2)}]/2 \tag{3.3}$$

Measurements in which the discriminator is negative are eliminated from further consideration.

3.4 In situ Observation of Chemically Induced Grain Boundary Migration in Al-Zn Diffusion Couples

By exploiting the surface migration behavior of CIGM in the Al-Zn system, it is possible to observe the migration of a boundary in situ. Such an observation is anticipated to yield a considerable amount of information concerning the migration behaviour of grain boundaries under these conditions.

3.4.1 Sample Preparation and Heat Treatment

The samples required for the in situ observation are identical to the surface migration samples in all aspects. The experiment was conducted in a Cambridge Stereoscan S180 SEM with an attached Kevex 7000 X-ray analyser. A heating stage for this microscope was easily constructed as shown in Figure 3.3. Using the thermocouple embedded within the heating block, the temperature was held to within 2°C with the aid of microcomputer control (Apple II+) as shown in Figure 3.4. The progress of the boundary was recorded by using the backscatter image from the sample and a digital line scan recording of the zinc K alpha line intensity. The actual migration distance is obtained by correcting the measured results for tilt and rotation of the sample.

3.4.2 X-Ray Analysis

In order to facilitate analysis at a later date, the x-ray line intensity data were recorded digitally instead of by the usual line scan photograph. This method allowed extremely slow line scans in excess of 5 minutes. The Kevex system was first initialised to produced digital pulses from the map output by placing a count window around the zinc K alpha spectral line. These pulses were counted over short time periods and then collected by a microcomputer (Apple II+) as shown schematically in Figure 3.4. Once the data was collected, the line scan was produced by grouping the short period counts into larger groups, smoothing the data over a number of the larger groups and subtracting the background.

3.5 In situ Observation of Discontinuous Precipitation in the Al-Zn System

This experiment permitted an in situ observation of the discontinuous precipitation process in the Al-Zn System whose equilibrium phase diagram is shown in Figure 3.5. This system was chosen as it precipitates at low temperatures (100 - 200°C) which does not place an extreme demand upon the heating stage. Unfortunately, this system undergoes a wide range of continuous processes which interferes with the discontinuous process. The continuous precipitation sequence is:

Supersaturated alpha => Guinier-Preston Zones =>

rhombohedral alpha => cubic alpha => zinc

The experiment would not be possible without a heating stage which is capable of attaining the required temperature and vacuum stability demanded from it. Such a heating stage was not readily available from the manufacturers of the HB5 STEM, Vacuum Generators Inc., therefore, an inhouse construction of such a stage was initiated. The design detailed for the stage is given in Appendix C and the stage is shown in Figure 3.6.

3.5.1 Sample Preparation

A 22% Zn-Al alloy was obtained in the form of a rolled plate. A section was removed and cold rolled until it reached the thickness of 0.15 mm. This foil was then cut into smaller sections and electrolytically polished using the window technique and a 15% Perchloric Acid - Methanol electrolyte. The foil's final thickness was approximately 25 microns.

From the thinned foil, a large quantity of 3 mm disks were punched and then wrapped tightly in a foil of the same alloy. This packet was then rewrapped in aluminum foil for water tightness. The packet was then annealed at a temperature of 370 to 380°C for 1 hour. This heat treatment produced a single phase alloy and a recrystallised structure which was fine enough to allow a large number of grain boundaries to be present in the final thinned sample. The packet was quenched into an ice water bath, then quickly placed into an alcohol bath cooled to 0°C. The inner packet was then removed while still within the alcohol and then quickly placed into a dry ice - methanol bath (-78°C). All further handling of the samples were performed under a dry ice - methanol bath in order to prevent excessive spinodal decomposition and grain boundary precipitation of the zinc rich phase. The disks were then jet polished using a Fischione jet polisher. The electrolyte was a 15% Perchloric Acid - Methanol mixture used at -30°C. A higher polishing current (10 mA) was used at first for about 1 minute in order to break the oxide film and thin the sample uniformly. A final polishing current of 2-4 mA for 3 to 4 minutes was used to produce the final thinned zone. The finished disks were stored in a dry ice - methanol bath to prevent alloy decomposition.

3.5.2 Heating Stage Operation and Heat Treatment

Prior to sample insertion into the heating stage, the stage is loaded into the microscope empty and heated. This step allows the stage's specimen holder and heater to degas so that during the actual experiment, vacuum integrity is not compromised. The stage is then allowed to cool and the specimen is immediately loaded into it and

reinserted into the microscope. Due to a number of heat transfer problems, the actual specimen temperature is not well known even though the stage temperature is monitored. Therefore, the actual specimen temperature can only be estimated using the dissolution temperature of the discontinuous precipitate as a calibration point.

The STEM is set to standard EIA television scan rates and the video output was recorded using a standard VHS video recorder. The signal recorded was from the annular dark field detector. This detector was chosen as it provided the best signal to noise ratio at EIA scan rates. The video signal from the bright field detector was deemed too noisy to record.

The sample was heated using a current regulated supply with the temperature monitored continuously and the sample tilt set to zero. The grain boundaries of the sample were carefully monitored and a suitable lamellae colony was chosen. The criterion for the colony chosen was:

<1> The zinc lamellae were parallel to the electron beam.

<2> The area of interest was in a thin part of the foil.

<3> Interfacial contrast was great enough to be discernible.

Quite often, discontinuous precipitation ceases before a meaningful observation can be recorded. This problem can be easily surmounted by simply heating the sample past the dissolution temperature of 573 K. The discontinuous product dissolves leaving the boundary (usually) in the middle of the grain. The sample is then cooled as quickly as possible and the discontinuous product reappears and grows.

With the discontinuous precipitation process recorded on video

tape, the measurement of instantaneous velocities for a particular interface shape was easily performed. Since the signal to noise ratio for the recorded signal was also low, still photographs were made from the recording by allowing the television frames to be integrated by using a long shutter time (1 sec) in photographing the monitor screen.

3.5.3 Microanalysis

The composition profiles of the depleted alpha lamellae of the discontinuous product was measured using the microanalytical capabilities of the HB5 STEM and the Tracor Northern TN7000 energy dispersive analyser. The sample was transferred from the heating stage into a double tilt analysis stage. This was done in order to tilt to the best analysis angle and to avoid spurious excitation of the sample from the X-ray generated from the stainless steel sample holder of the heating stage. Positioning of the beam back to the original area was not difficult, since the recorded image greatly aided reorientation.

The factors which control the accuracy and the resolution of the microanalysis are:

<1> Beam Spreading: This effect is minimised by using a thin part of the foil and since spreading is proportional to atomic number the use of an aluminum alloy also minimises this effect.

<2> Specimen Drift: This effect is minimised through the use of drift compensation circuits which produce small deviations in the scan system.

<3> Extraneous X-rays: The use of a beryllium holder, the removal of the objective aperture and the use of an X-ray collimator on the detector reduces this effect.

<4> Absorption Effects: A thinner portion of the sample reduces this effect.

<5> Probe size: Since the objective aperture omitted from the analysis, the probe is larger than is possible, however, through the use of a virtual objective aperture, beam definition is still possible. The smallest virtual objective aperture (100 um) was used to produce a 1 nm probe size.

The quantitative nature of the analysis relies on the thin film criterion (D3) which states that the count rate from a particular element is proportional to its concentration. Therefore, the ratio of the total X-ray counts (I_a/I_b) for each element of interest is related to their concentration (C_a/C_b) ratios as given by Cliff-Lorimer:

$$C_a/C_b = K_{ab}\, I_a/I_b \qquad (3.4)$$

where K_{ab} is a constant which involves the accelerating voltages, fluorescence factors, film thickness and detector geometry. This factor known as the Cliff-Lorimer constant can be determined analytically or experimentally. These particular sets of experiments will use an experimentally determined factor. The factor was determined by using the undecomposed portion of the foil as a standard (22 at%).

The actual collection of X-ray data was performed using the following techniques:

<1> The collection time must be minimised in order to prevent excessive contamination buildup.

<2> The detector deadtime level should be kept less than 10%.

<3> The probe is stepped manually across the lamellae, however, particular attention was given when the probe was nearest the zinc

lamellae. The analysis spot was kept as far away as possible in order to prevent spurious zinc X-rays from being generated from the zinc lamellae.

<4> The background was manually removed from the aluminum K_α and the zinc K_α lines.

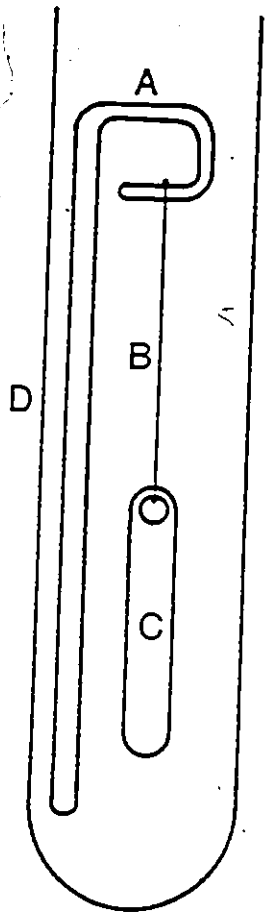

Figure 3.1 Tensile Stress Experimental Design
(a) Glass Rod Support
(b) Al-Zn Wire Diffusion Couple
(c) Glass Weight
(d) Evacuated Glass Tube

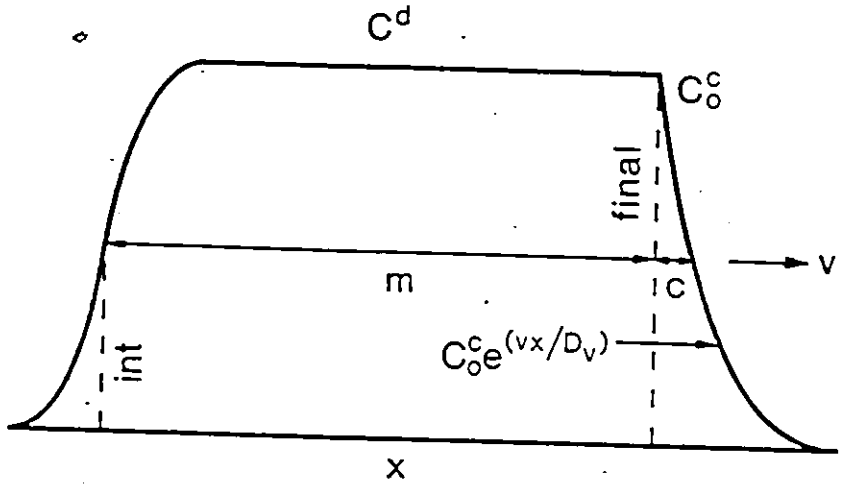

Figure 3.2 Concentration Profiles During CIGM (Refer to text)

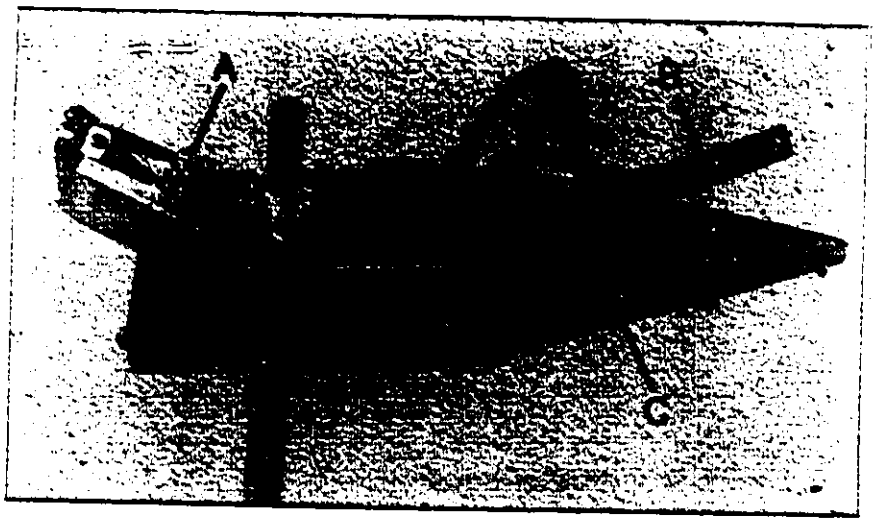

Figure 3.3 Cambridge Stereoscan S180 Heating Stage
(a) Heating Block
(b) Specimen Stage
(c) Electrical Contact Block

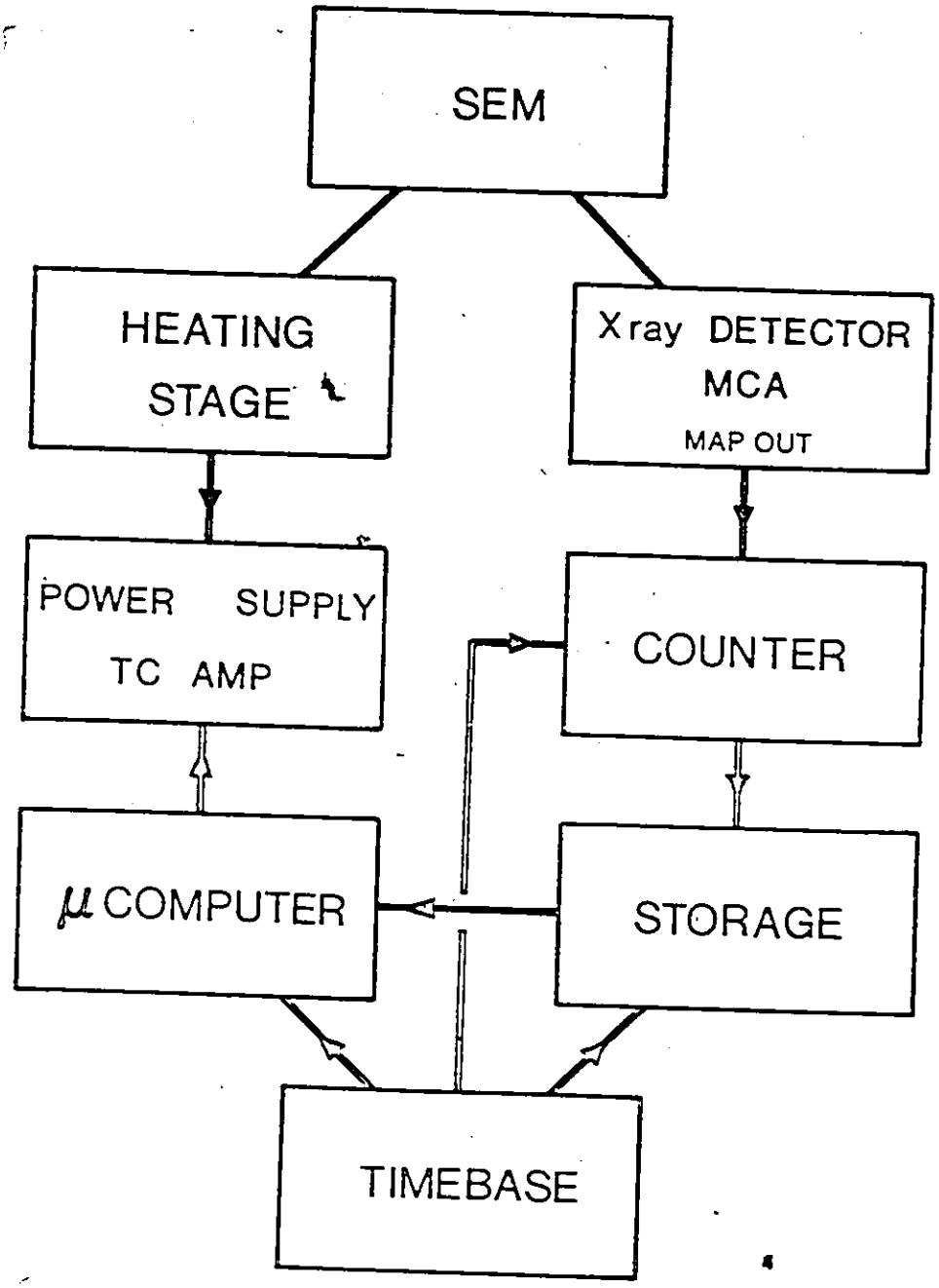

Figure 3.4 Block Schematic of the in situ CIGM Experimental Control System

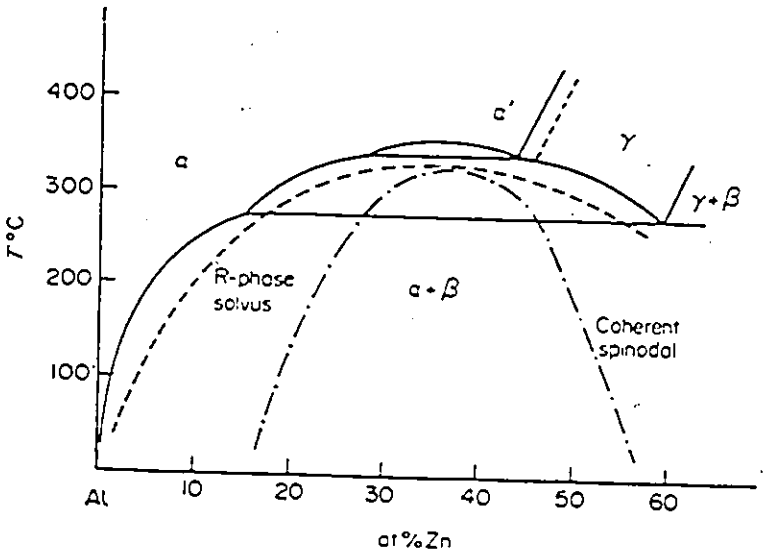

Figure 3.5 Al-Zn Equilibrium Phase Diagram

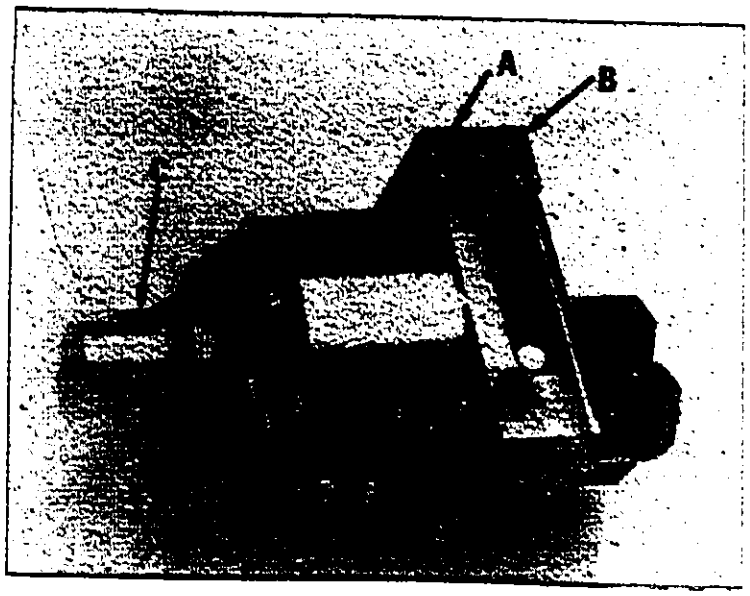

Figure 3.6 HB5 STEM Heating Stage
(a) Modified Double Tilt Body
(b) Electrical Contact Block
(c) Heating Nose Piece (Appendix C)

CHAPTER 4

EXPERIMENTAL RESULTS

The intention of the present investigation was to attempt to establish the importance of a chemical driving force in the migration of a grain boundary. This was attempted by studying the following features of a chemically induced migrating boundary; the universality of boundary movement and the detailed characteristics of movement. These features will be considered in the following sections.

4.1 CIGM in New Alloy Systems

The experimental evidence presented here, illustrates the existence of CIGM in many of the systems studied with the exception of one system. Tables 4.1 and 4.2 tabulate the migration characteristics, volume diffusion penetration and solute concentrations respectively. Figures 4.1 to 4.7 illustrate CIGM in these systems. The main feature observed is an asymmetric etching effect about the boundary indicating assymetric alloying due to boundary migration. In addition, boundary bowing, which represents migration against capillarity is also present. Perhaps most important is the observation that migration can take place under conditions of low and high volume penetration from the boundary for different systems as shown in Table 4.2 and within the same system such as the Ag-Pd and Pt-Pd system.

The migration characteristics differ from system to system. Migration can be uniform and linear as in the Ag-Pd system or very

irregular such as in the Cu-Mn system. The presence of CIGM in the Ag-Cu system is sometimes obscured by the presence of annealing twins as shown in Figure 4.1. Therefore, X-ray analysis was a necessity in order to confirm the presence of an alloyed zone.

An interesting feature is the absence of CIGM in the Ag-Mn system. The confidence of this observation is limited to the resolution of the instruments used. Under these conditions, the boundary is positioned symmetrically in the etched zone. The X-ray line scan using the Mn K_{α} line as shown in Figure 4.8, substantiates this feature as it exhibits the expected shape for volume diffusion penetration from the grain boundary only.

Table 4.1

Migration Characteristics of Various Binary Alloys

Mat.	Sol.	Temp °C	Time hrs	dm um	dv um	dc um	v pm/s
Ag	Cu	400	408	19±7	0	19±7	12±4
		500	408	27±6	.2	26.8±6	18±4
Ag	Mn	400	216	0	0	0	0
		500	144	0	0	0	0
Ag	Pd	400	216	3.9±.6	0	3.9±.6	5±.7
		500	144	4.2±.8	0	4.2±.8	8±1
Au	Ni	600	75	9.3±.9	2.9	6.4±.9	23±3
Au	Pd	500	144	13.6±4	0	13.6±4	26±7
Cu	Mn	400	216	6.1±1	0	6.1±1	8±1
		500	144	15.8±6	0	15.8±6	30±12
Cu	Pd	400	216	3.1±.6	0	3.1±.6	4±.7
Pt	Pd	500	408	2.5±1	0	2.5±1	2±.8
		800	48	10.1±2	0	10.1±2	58±11

Note: dm: measured distance
dc: corrected distance
dv: volume diffusion penetration distance
<dv> is determined by equation 3.3 using values of
of the volume diffusivity which can be found in Table 4.2

Table 4.2

Concentration and Penetration Characteristics of Various Binary Alloys

Mat.	Sol.	Temp	Time	Dv	Dv/v	X
		°C	hrs	m^2/s		at%
Ag	Cu	400	408	$8x10^{-20}$	6 nm	*
		500	408	$6x10^{-18}$	330 nm	2.6±.2
Ag	Mn	400	216	$9x10^{-22}$	-	7±.5
		500	144	$9x10^{-20}$	-	13±.5
Ag	Pd	400	216	$3x10^{-22}$	60 pm	*
		500	144	$8x10^{-20}$	10 nm	*
Au	Ni	600	75	$1x10^{-16}$	4.3 um	8±.3
Au	Pd	500	144	$3x10^{-18}$	110 nm	*
Cu	Mn	400	216	$5x10^{-20}$	6 nm	>.1
		500	144	$4x10^{-18}$	130 nm	>.1
Cu	Pd	400	216	$3x10^{-22}$	75 pm	.2±.1
Pt	Pd	500	408	$1x10^{-23}$	5 pm	8.3±.5
		800	48	$1x10^{-18}$	20 nm	10.7±.5

Notes: * X-ray Determination of Solute not performed due to overlapping spectral lines or extremely low concentrations levels

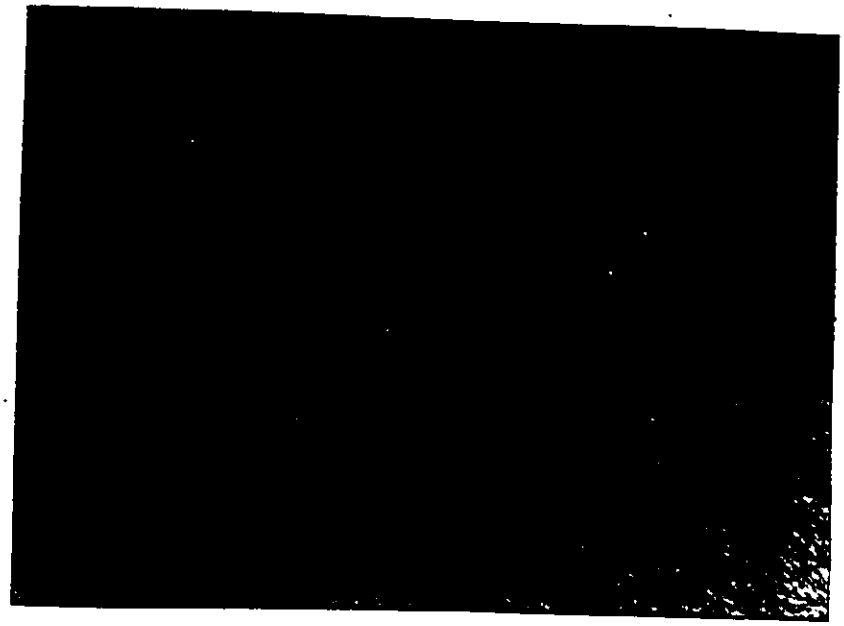

Figure 4.1 Optical micrograph of CIGM in the Ag-Cu system
Interference contrast 500°C 408hrs

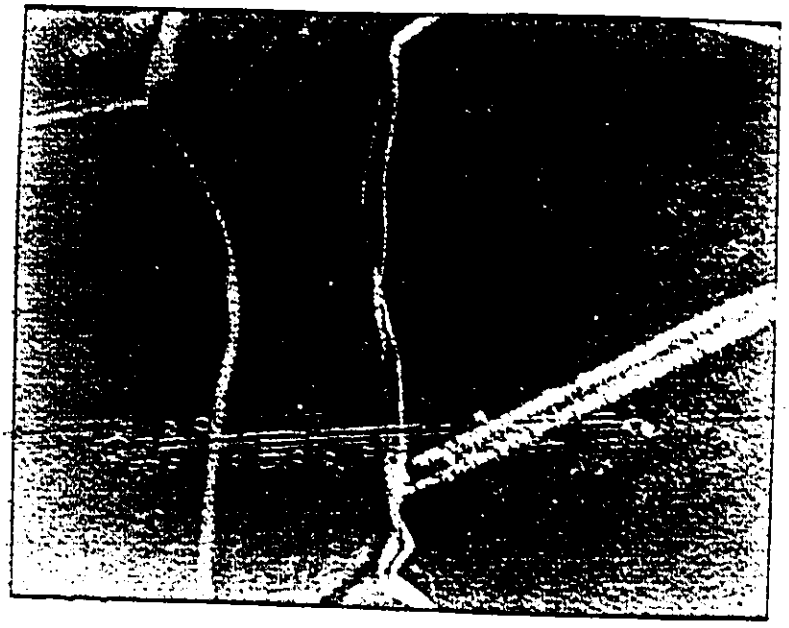

Figure 4.2 Optical micrograph of CIGM in the Ag-Pd system
Interference contrast 500°C 144hrs

Figure 4.3 Scanning electron micrograph of CIGM in the Au-Ni system 600°C 75hrs

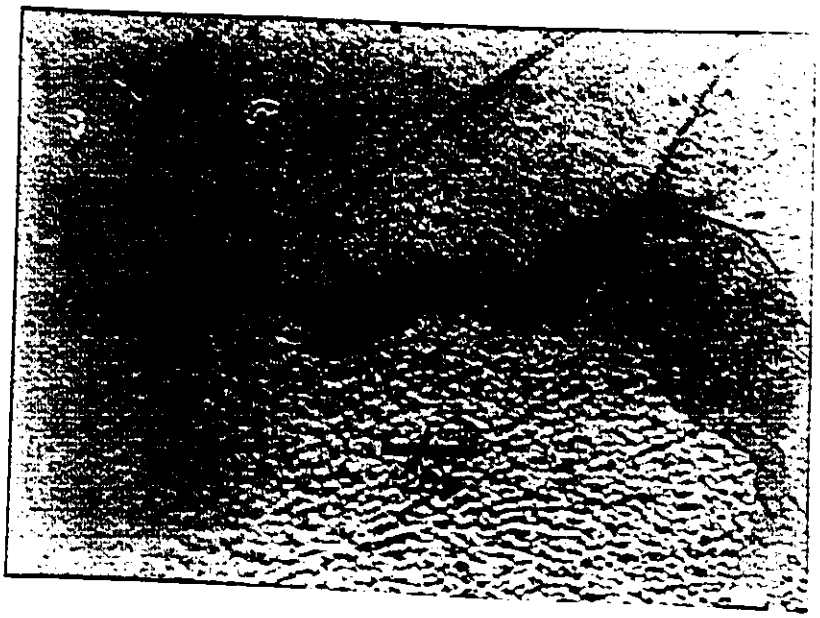

Figure 4.4 Optical micrograph of CIGM in the Au-Pd system 500°C 144hrs

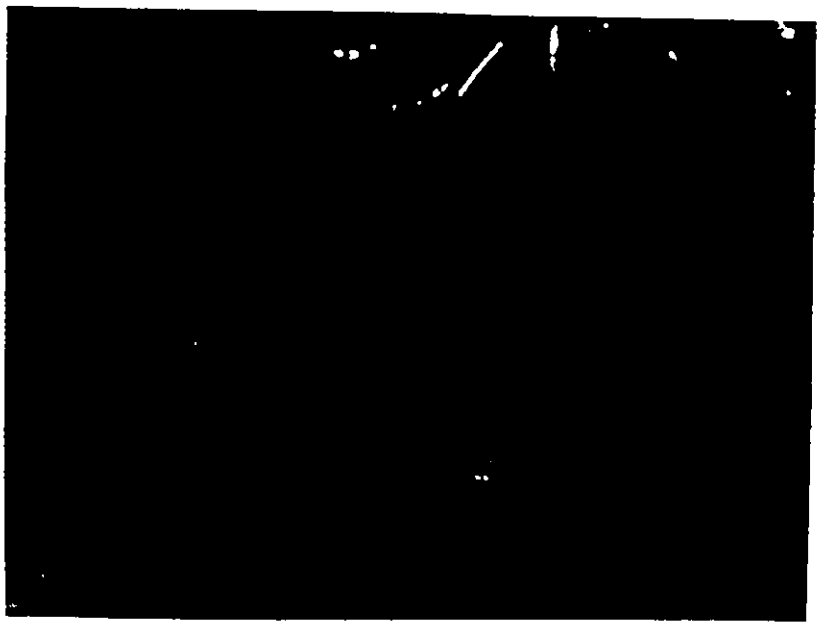

Figure 4.5 Optical micrograph of CIGM in the Cu-Mn system (Note the large amount of irregular migration) Interference contrast 500°C 144hrs

Figure 4.6 Optical micrograph of CIGM in the Cu-Pd system Interference contrast 400°C 216hrs

Figure 4.7 Optical micrograph of CIGM in the Pt-Pd system
Interference contrast 500°C 408hrs

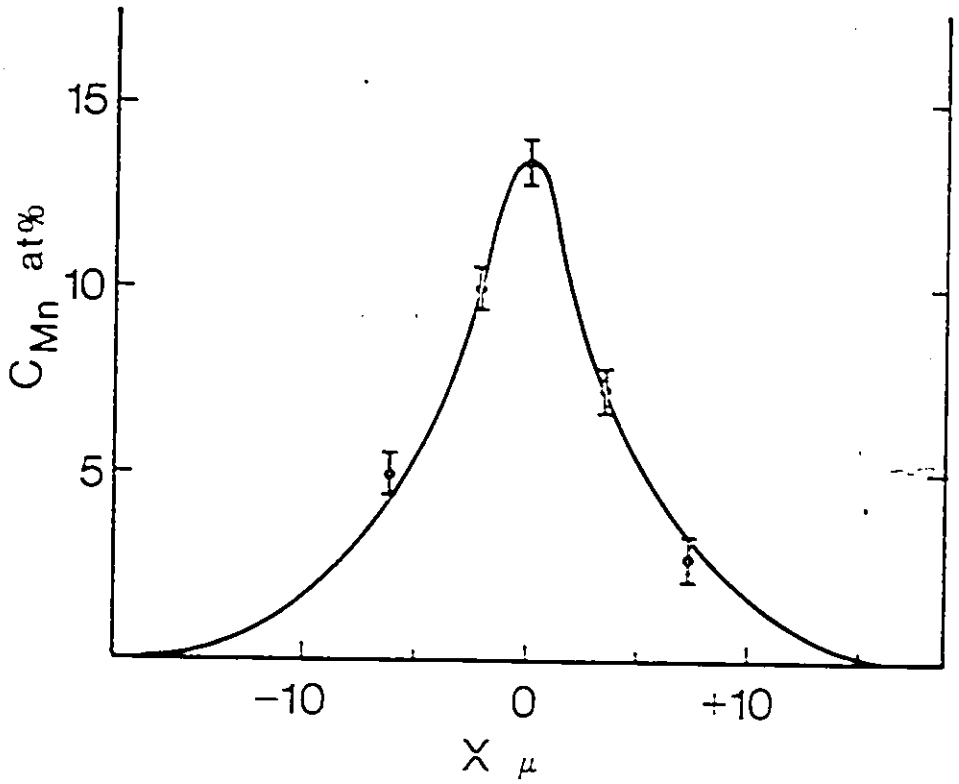

Figure 4.8 Mn K_α X-ray line scan across a grain boundary profile in the Ag-Mn system. This profile is produced by volume diffusion from a static boundary.

4.2 Migration and Penetration Characteristics in the Al-Zn System

This purpose of this section is to present as comprehensive as possible, a study into the migration characteristics of CIGM in the Al-Zn system. This is attempted by studying as thoroughly as possible the following facets of CIGM in the Al-Zn system:

<1> Uniform migration in the bulk

<2> Migration near the free unplated surface

<3> CIGM alloy penetration into an infinite sample

<4> External stress effects

A typical example of uniform migration is given in Figure 4.9 and the associated concentration profiles across and along the boundary are shown in Figure 4.10. The migration against capillarity which is the usual distinguishing feature of CIGM is present in the Al-Zn system as demonstrated in Figure 4.11. A summary of the bulk migration velocities observed in this study is given as an Arrhenius plot in Figure 4.12.

An unusual feature of CIGM in the Al-Zn system is the presence of CIGM near the free unplated surface of the Al foil. This enhanced CIGM near a free unplated surface is shown in Figure 4.13. When this form of enhanced CIGM is observed optically using interference contrast, it appears that ridges lie off the plane of the foil as shown in Figure 4.14. These surface migration features appear as strong etched lines as shown in Figure 4.15 which indicate an enrichment of zinc. Surface migration appears at temperatures in which bulk migration is difficult to detect optically. Such surface migration as shown in Figure 4.16 appears

to coexist with volume diffusion from the boundary and true migration. The Arrhenius plot of this type of migration is given in Figure 4.17. Generally, it was observed that the displacements of boundaries undergoing enhanced CIGM near the surface were greater than those in the bulk.

Shown in Figure 4.18 is CIGM into infinite bulk samples at various temperatures. The concentration profiles as shown in Figure 4.19 are profiles which indicate that the alloyed layer concentration is determined by boundary diffusion.

Since external stress effects have been documented in CIGM (B5) and in discontinuous precipitation (A43), a search for similiar effects is attempted in the Al-Zn system. The effects for an externally applied tensile stress are shown in Figure 4.20. It can be seen that regardless of the stress level, no significant change in migration behaviour is present. Regardless of the stress level, there is no significant modification of the migration behaviour.

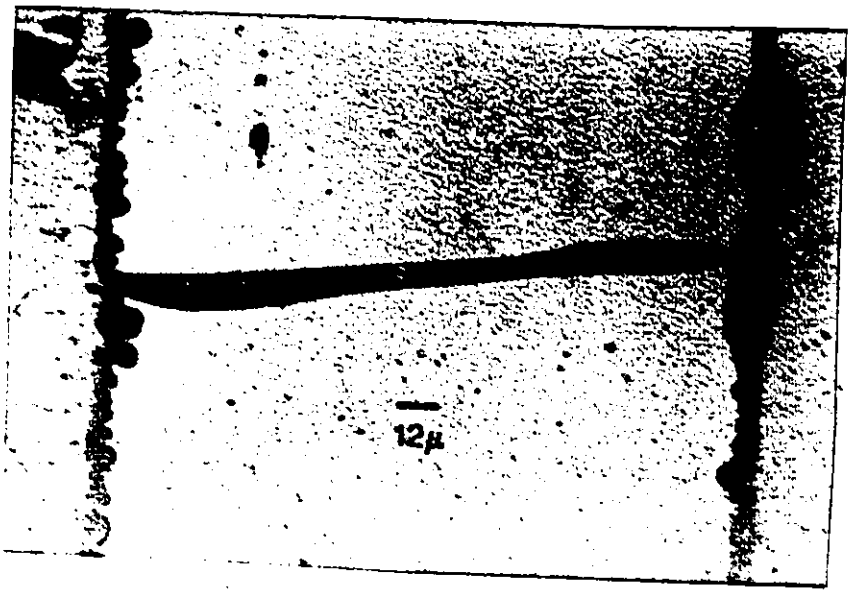

Figure 4.9 Optical micrograph of bulk CIGM in the Al-Zn system (200°C 95hrs)

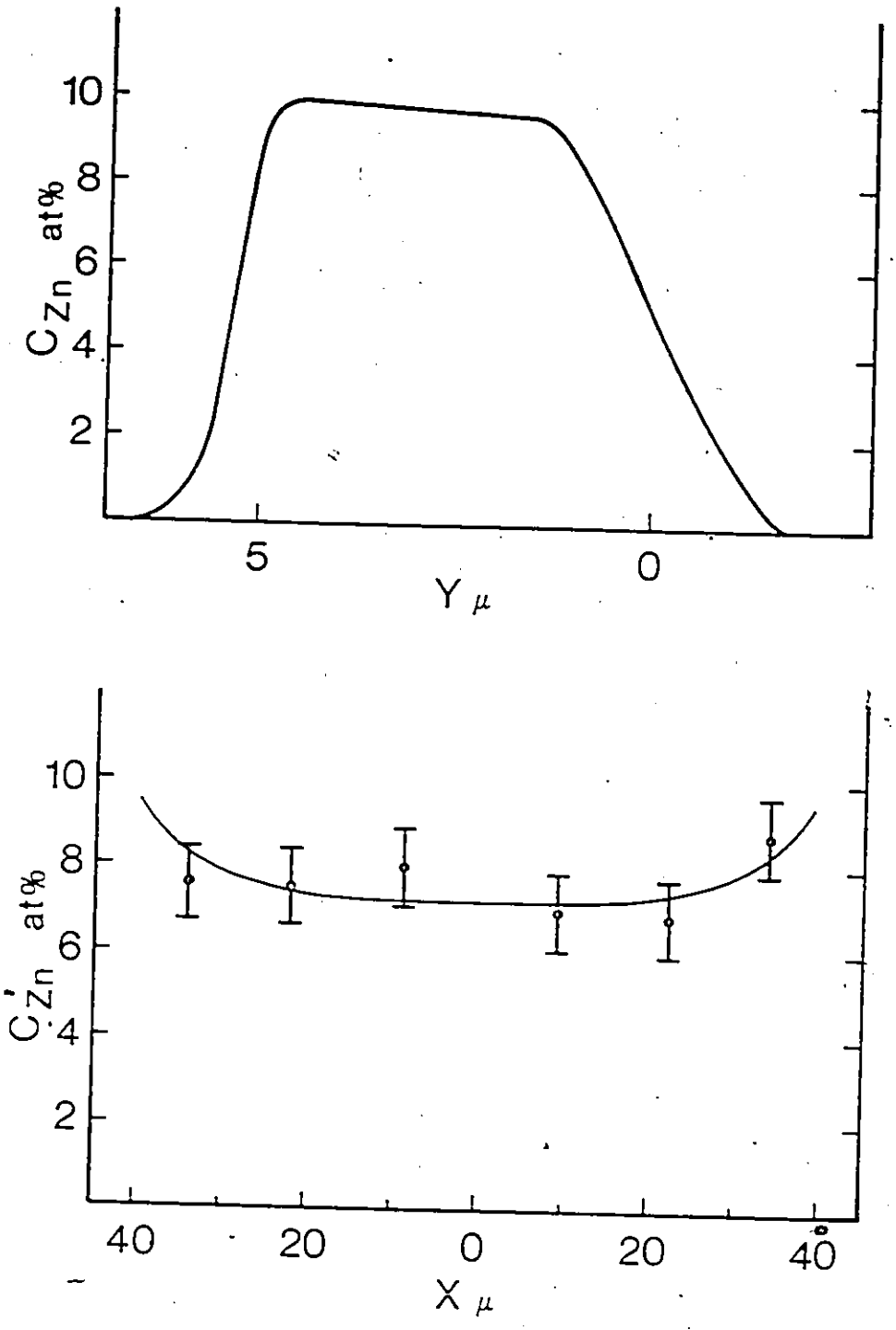

Figure 4.10 Parallel and perpendicular concentration profiles for Al-Zn CIGM.

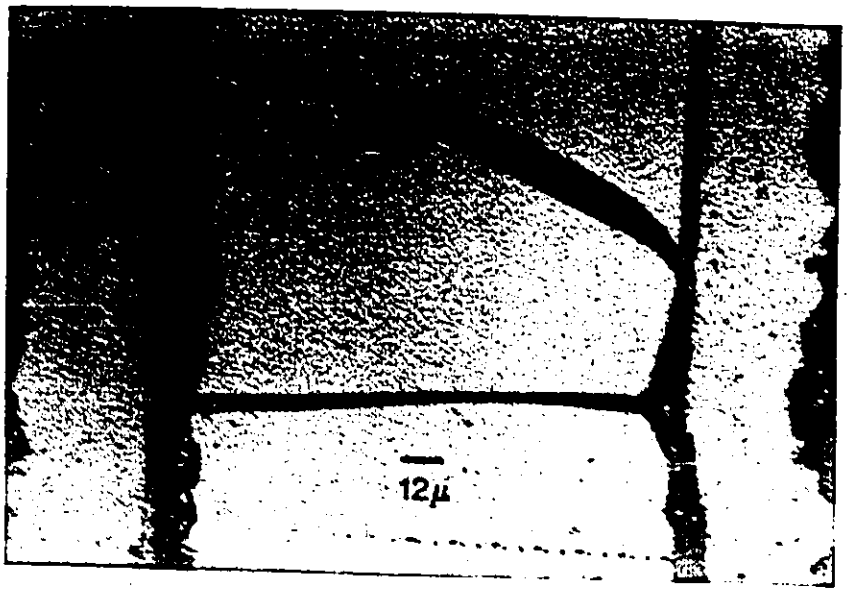

Figure 4.11 Optical micrograph of bulk CIGM in the illustrating migration against capillarity (200°C 95hrs)

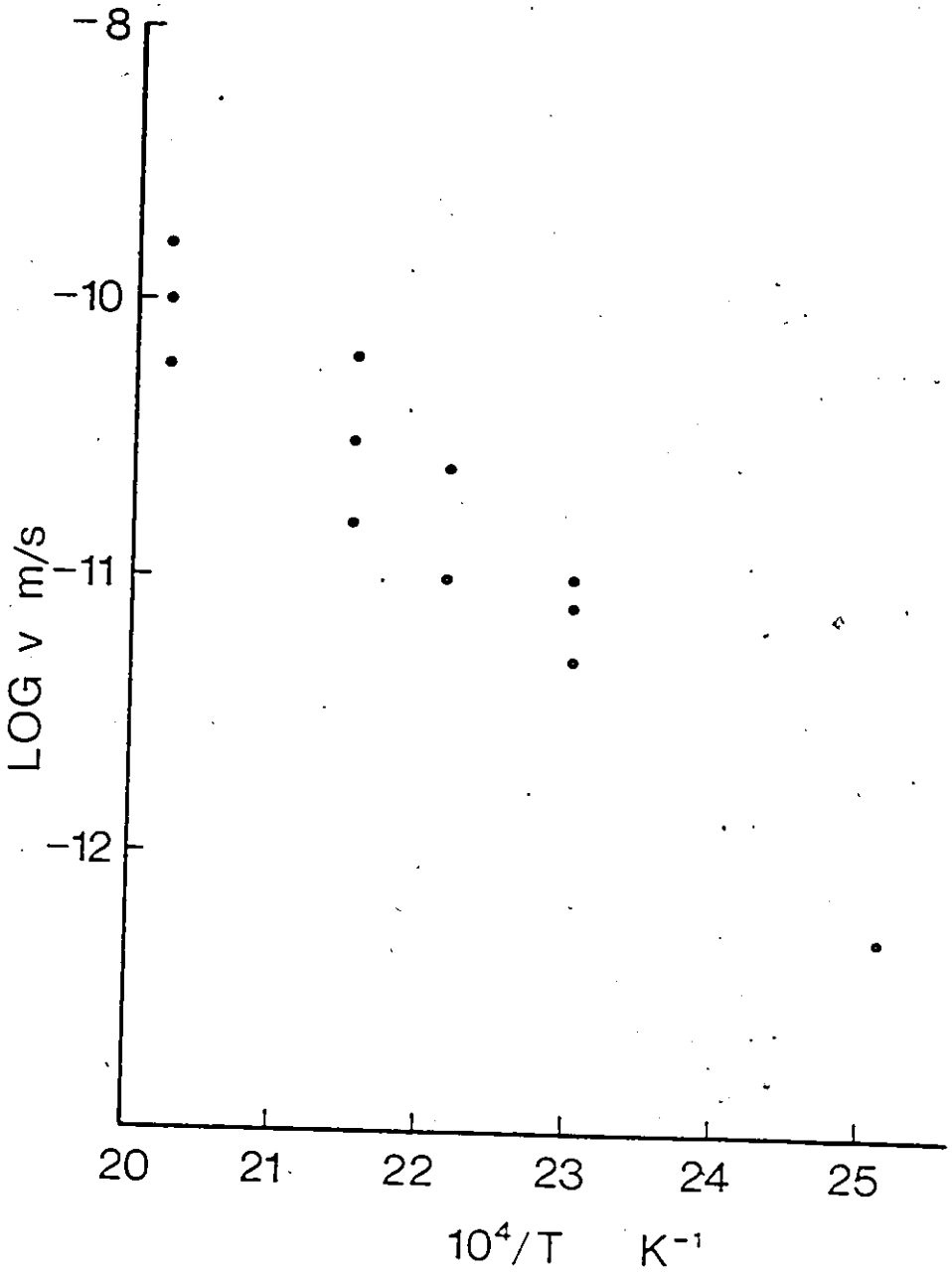

Figure 4.12 Arrhenius plots of bulk CIGM in the Al-Zn system.

Figure 4.13 Optical micrograph of bulk CIGM indicating enhanced migration at the surface. The enhancement appears as flattened migration zones in the bulk at the free surface. (195°C 262hrs)

Figure 4.14 Optical micrograph of surface CIGM. Interference contrast has been used to illustrate the formation of surface features which resemble ridge formation. (195°C 262hrs)

Figure 4.15 Optical micrograph of surface CIGM. Lightly etched. (175°C 120hrs)

Figure 4.16 Optical micrograph of surface CIGM. Etching suggests the boundary has not migrated in many areas. However, certain assymetric areas indicate migration has occurred. (100°C 408hrs)

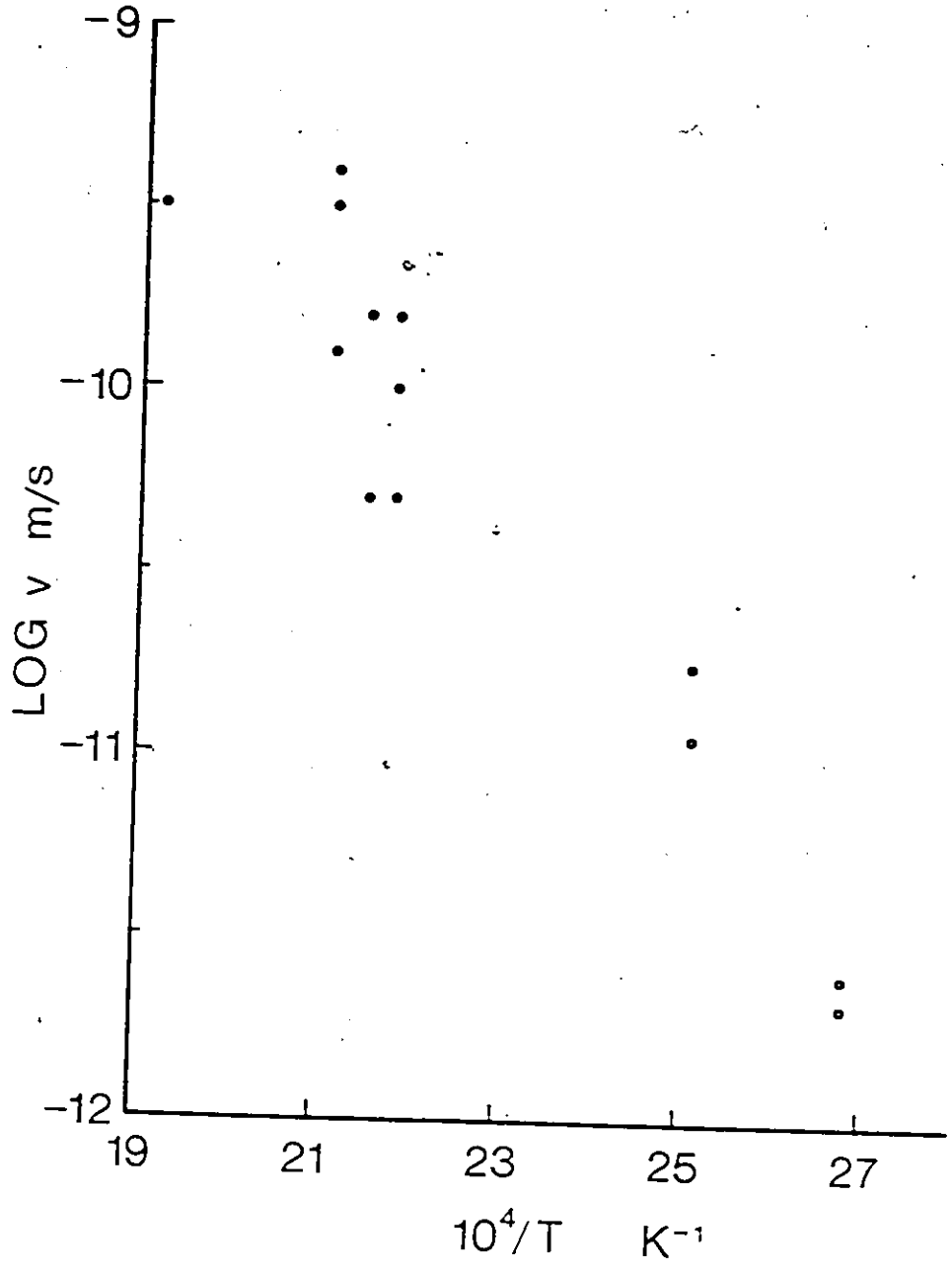

Figure 4.17 Arrhenius plots of surface CIGM in the Al-Zn system.

(a)

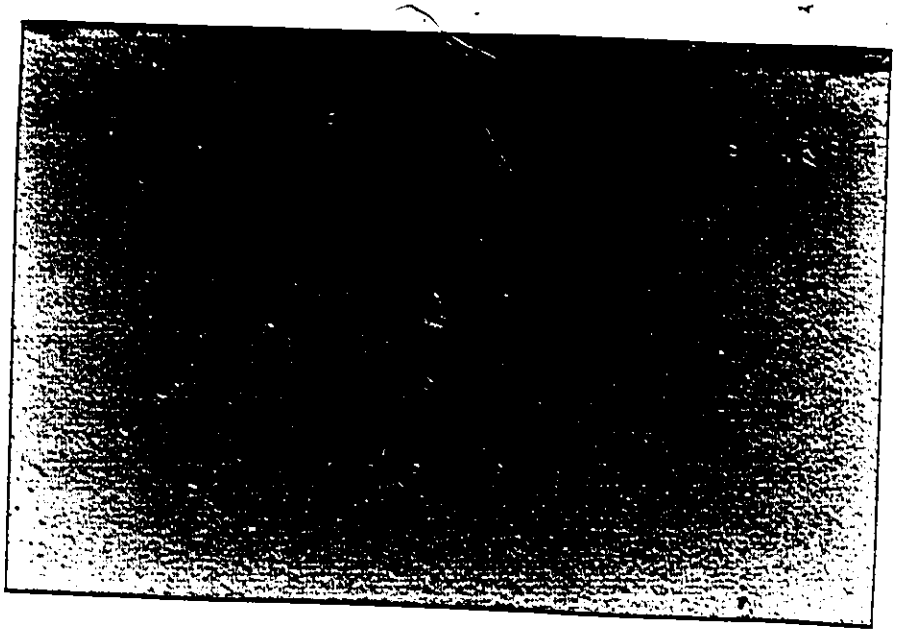

(b)

Figure 4.18 Optical micrographs of bulk CIGM in the Al-Zn system (a) 220°C 95 hrs (b) 195°C 144hrs

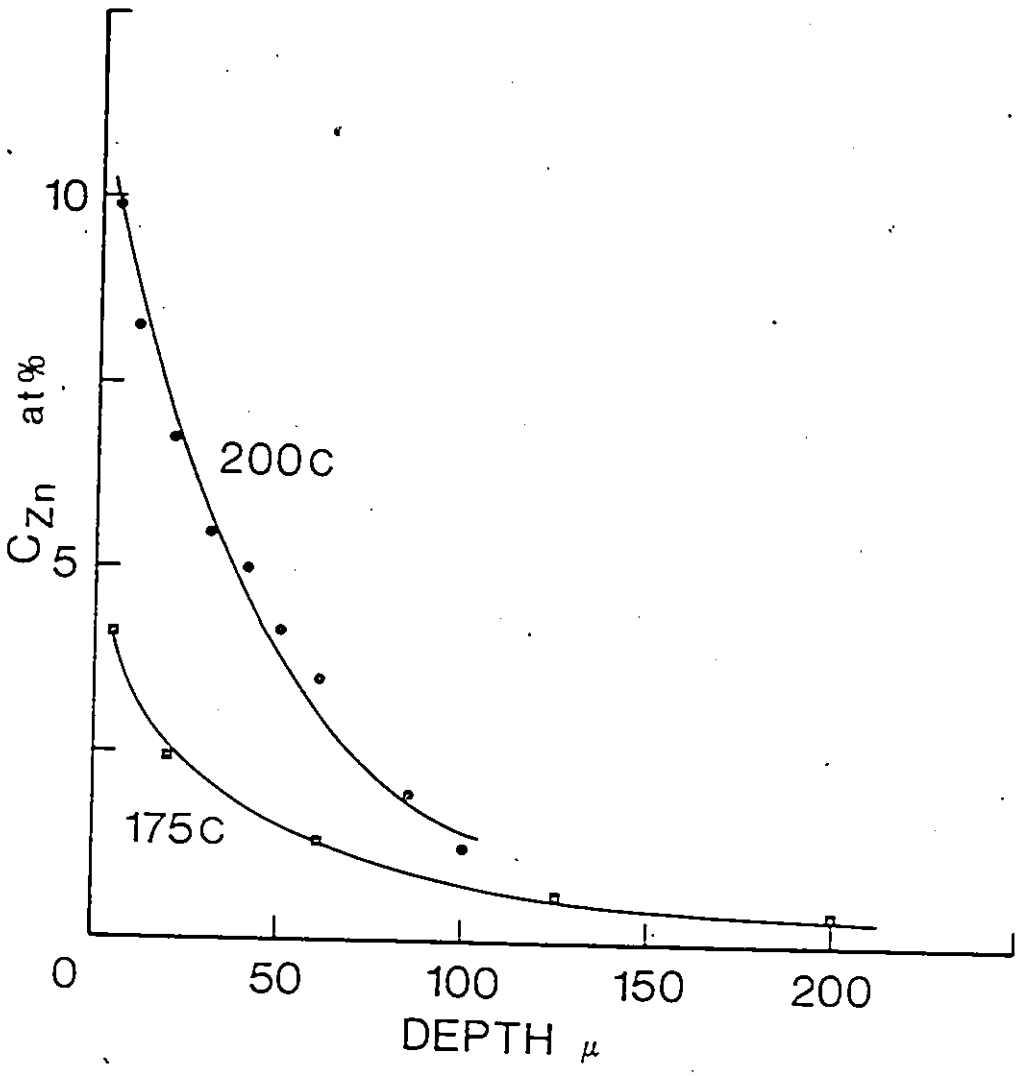

Figure 4.19 Concentration profiles parallel to the boundary in the alloyed zones of thick samples.

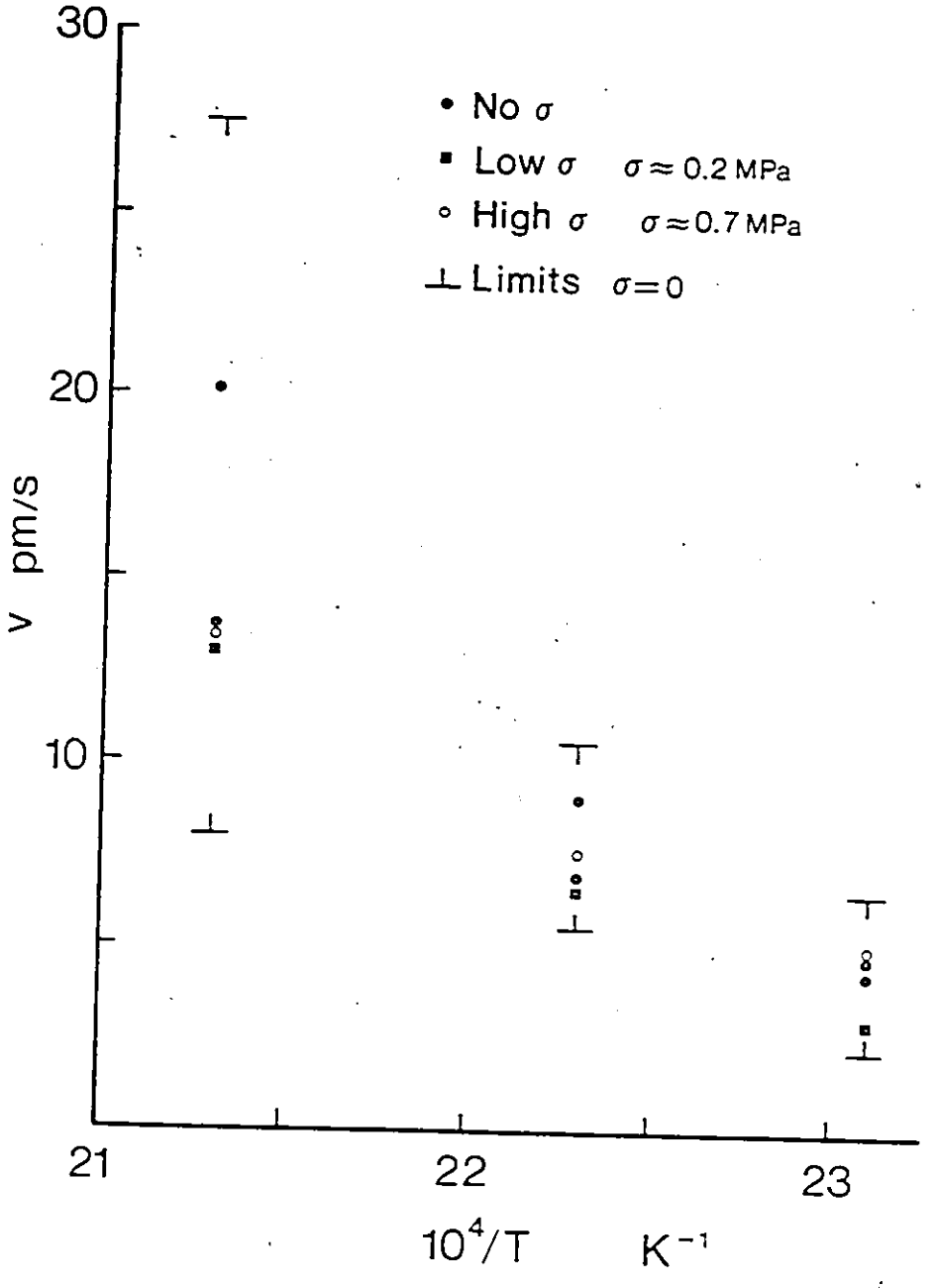

Figure 4.20 Effects of an externally applied stress upon the migration behaviour of CIGM in the Al-Zn system

4.3 In Situ Observation of CIGM in the Al-Zn System

The purpose of this study was to observe as much detail as possible, the migration characteristics of CIGM in the Al-Zn system. This was attempted by observing migration as it actually took place. The movement of the boundary was recorded using the backscatter image from the SEM imaging system and a zinc Ka line scan.

The actual recording of the initiation of migration was not possible due to lack of any discernible features. For a period of up to 3 hours, possible features were monitored without any significant changes due to migration occurring. Therefore, it was found that a certain amount of time was required to pass before recognizable features developed for recording. At this time, a number of features were noted, their position on the foil surface recorded and further observation was allowed to proceed.

Figures 4.21 and 4.22 demonstrate an interruption in the migration pattern of an aluminum boundary. The static boundary appears to enrich in zinc as it appeared to possess a greater contrast than the rest of the alloyed zone. This enrichment would also account for the dark etched lines which were observed in previous optical microscopy studies. The velocity of the boundary is definitely reduced by this feature. After a period of time, the boundary appears to regain its previous velocity.

Other boundaries appear to achieve steady state migration as shown in Figures 4.23 and 4.24. However, this is not always the case as other boundaries cease migration as shown in Figures 4.25 and 4.26. A summary of all the boundaries which were observed to migrate is

presented in Figures 4.27 to 4.29 for the temperature range as indicated. Boundary velocities appears to be very dependent upon the boundary being studied and the overall thickness of the foil being studied.

The observations made here do not conclusively remove the possibility of an incubation period existing since observation of the initiation process was not possible. The present study suggests that steady state migration is established early in time for most boundaries and is maintained for the period of the observation.

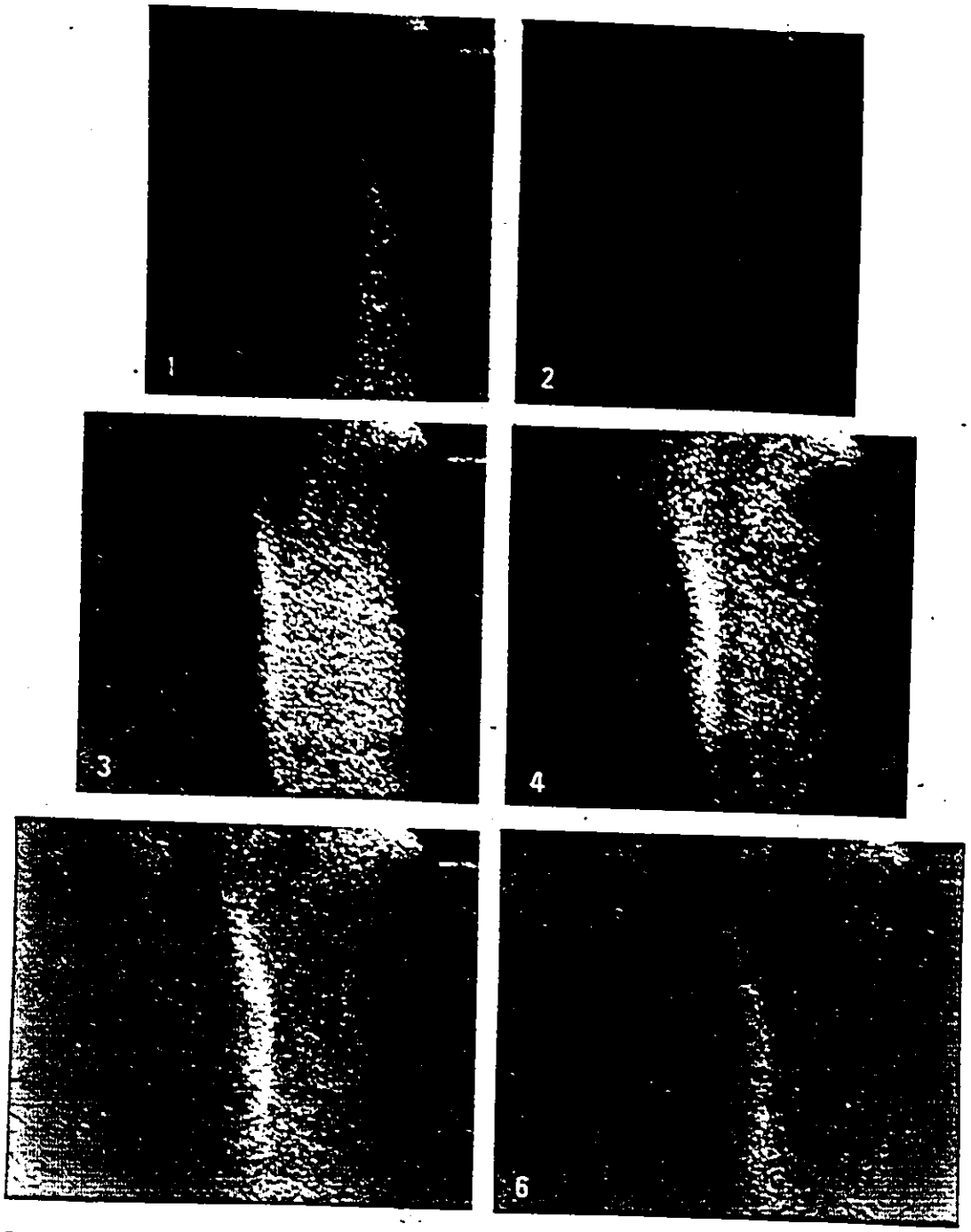

Figure 4.21 Migration sequence for boundary A in an Al-Zn diffusion couple. The boundary is pinned momentarily by the surface feature which appears to be created by the migration process itself. (185°C)
(1: 18hrs 2: 22hrs 3: 28hrs 4: 40hrs 5: 45hrs 6: 53hrs)

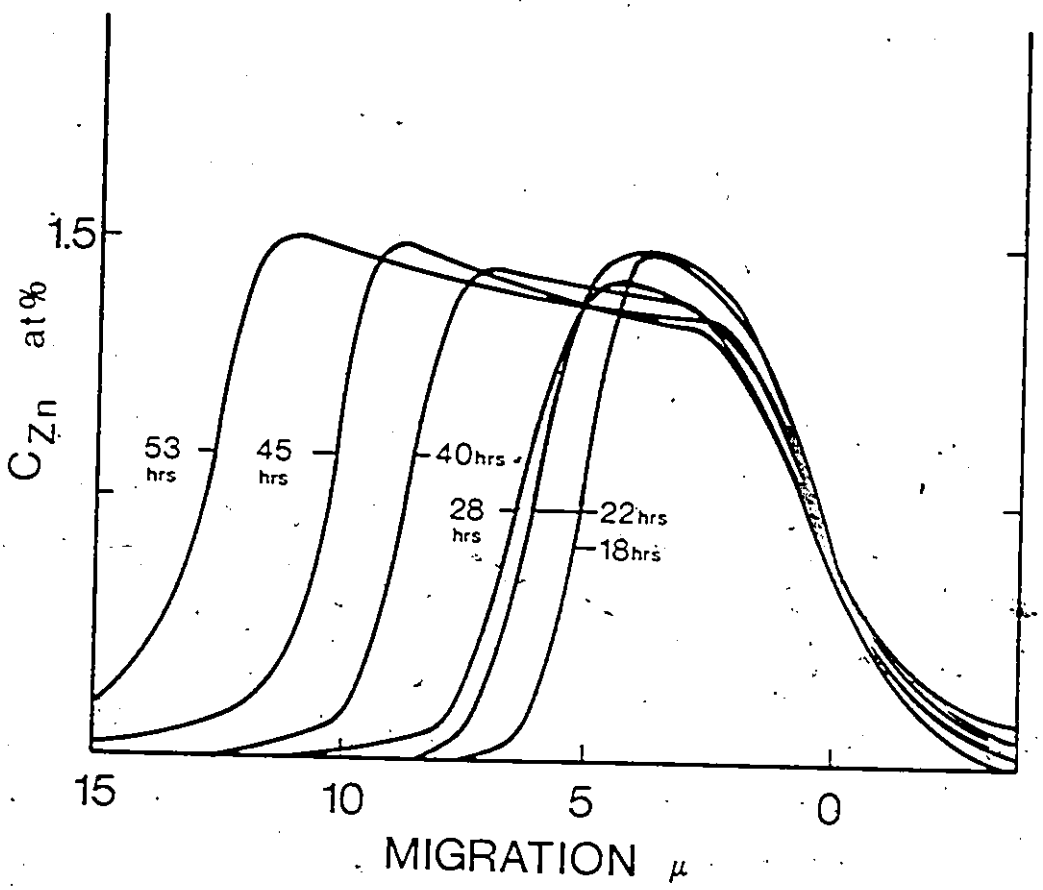

Figure 4.22 Zn K_α X-ray line scan sequence for grain boundary A

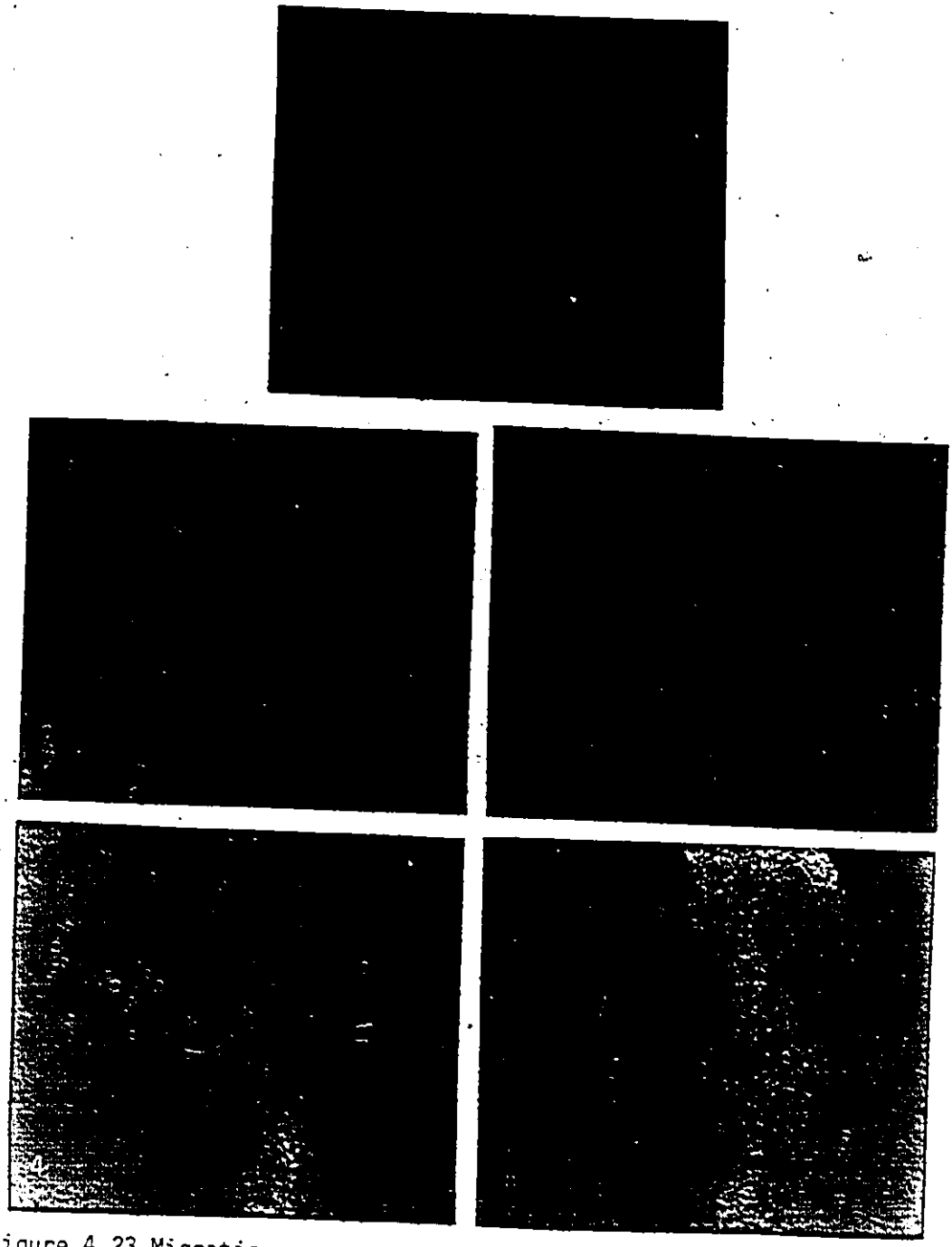

Figure 4.23 Migration sequence for boundary B in an Al-Zn diffusion couple. Migration appears to have reached a steady state. (185°C)
(1: 18hrs 2: 22hrs 3: 28hrs 4: 40hrs 5: 45hrs)

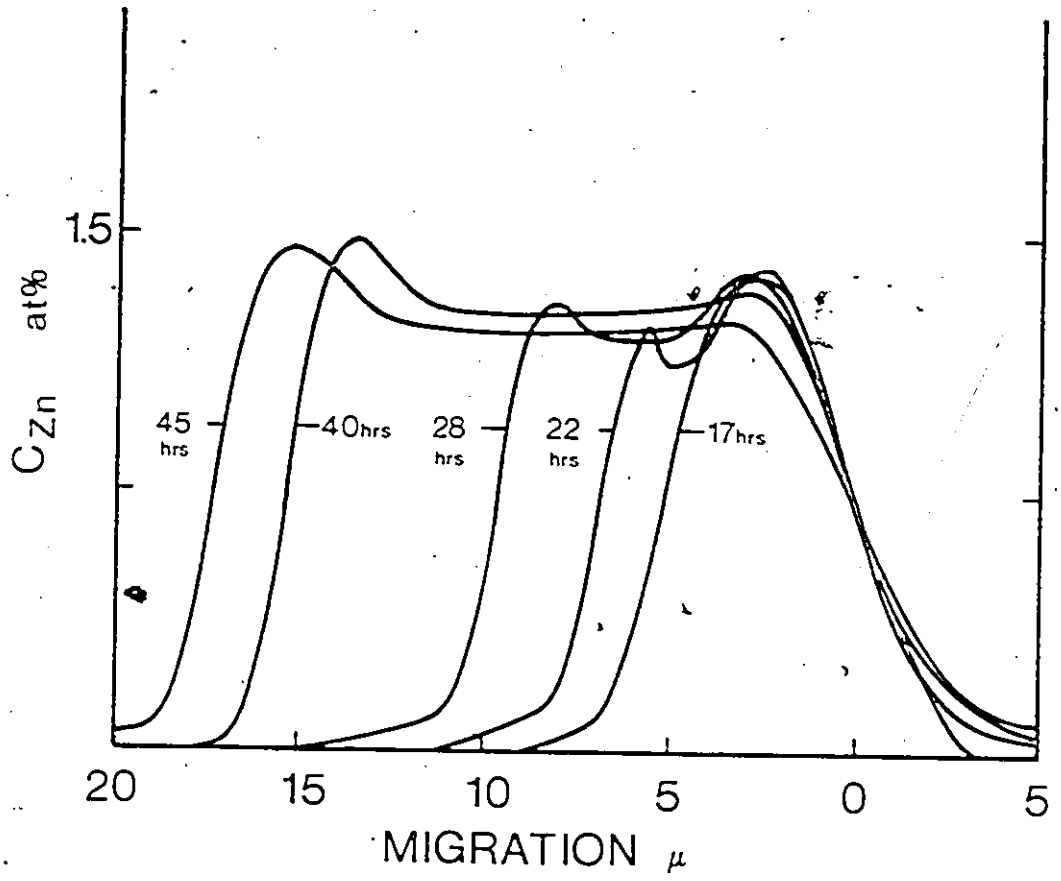

Figure 4.24 Zn K_α X-ray line scan sequence for grain boundary B

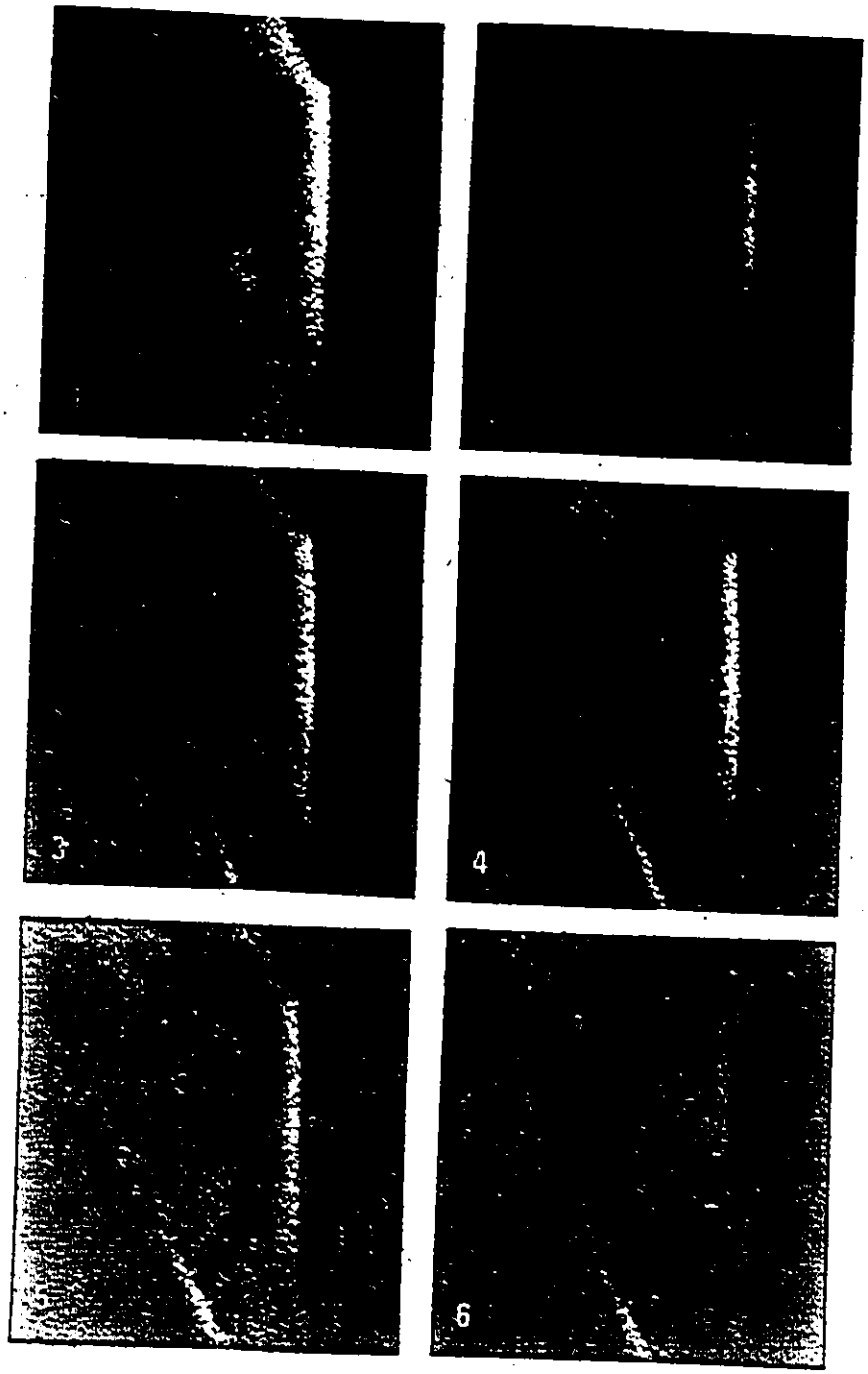

Figure 4.25 Migration sequence for boundary C in an Al-Zn diffusion couple. Migration appears to cease after steady state is acheived. (185°C)
(1: 18hrs 2: 22hrs 3: 28hrs 4: 40hrs 5: 45hrs 6: 64hrs)

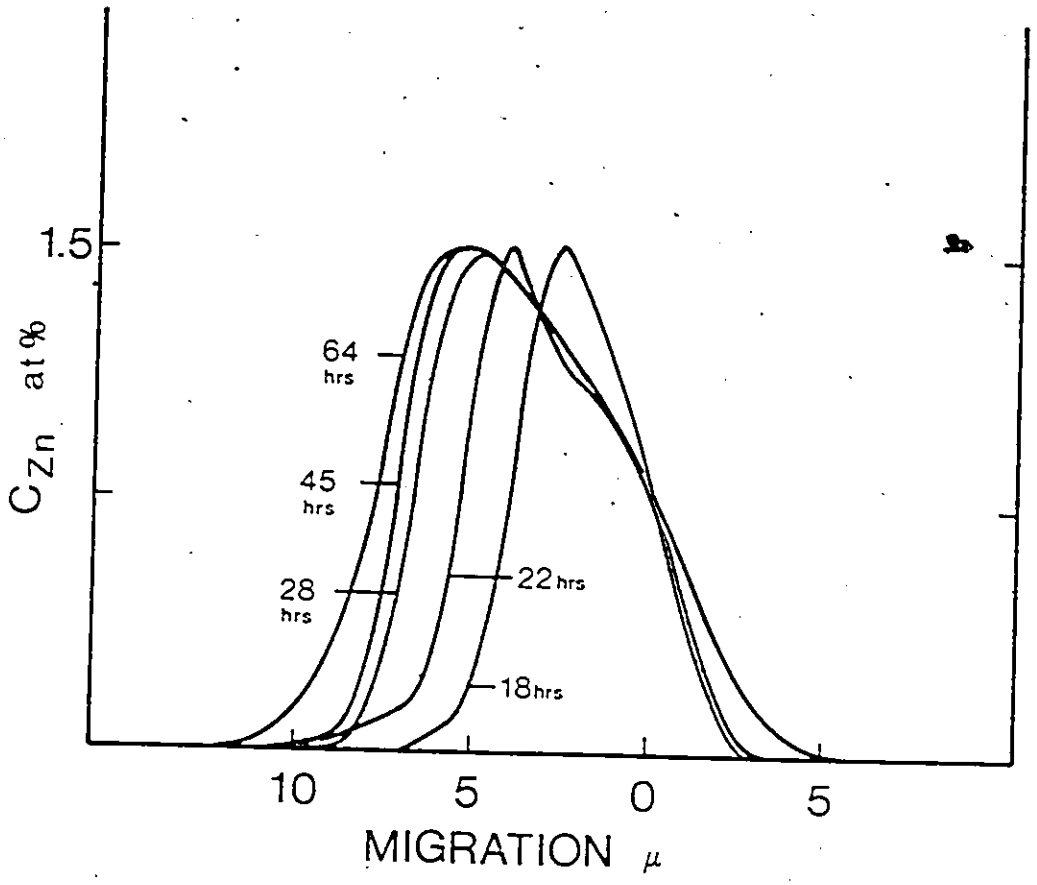

Figure 4.26 Zn K_α X-ray line scan sequence for grain boundary C

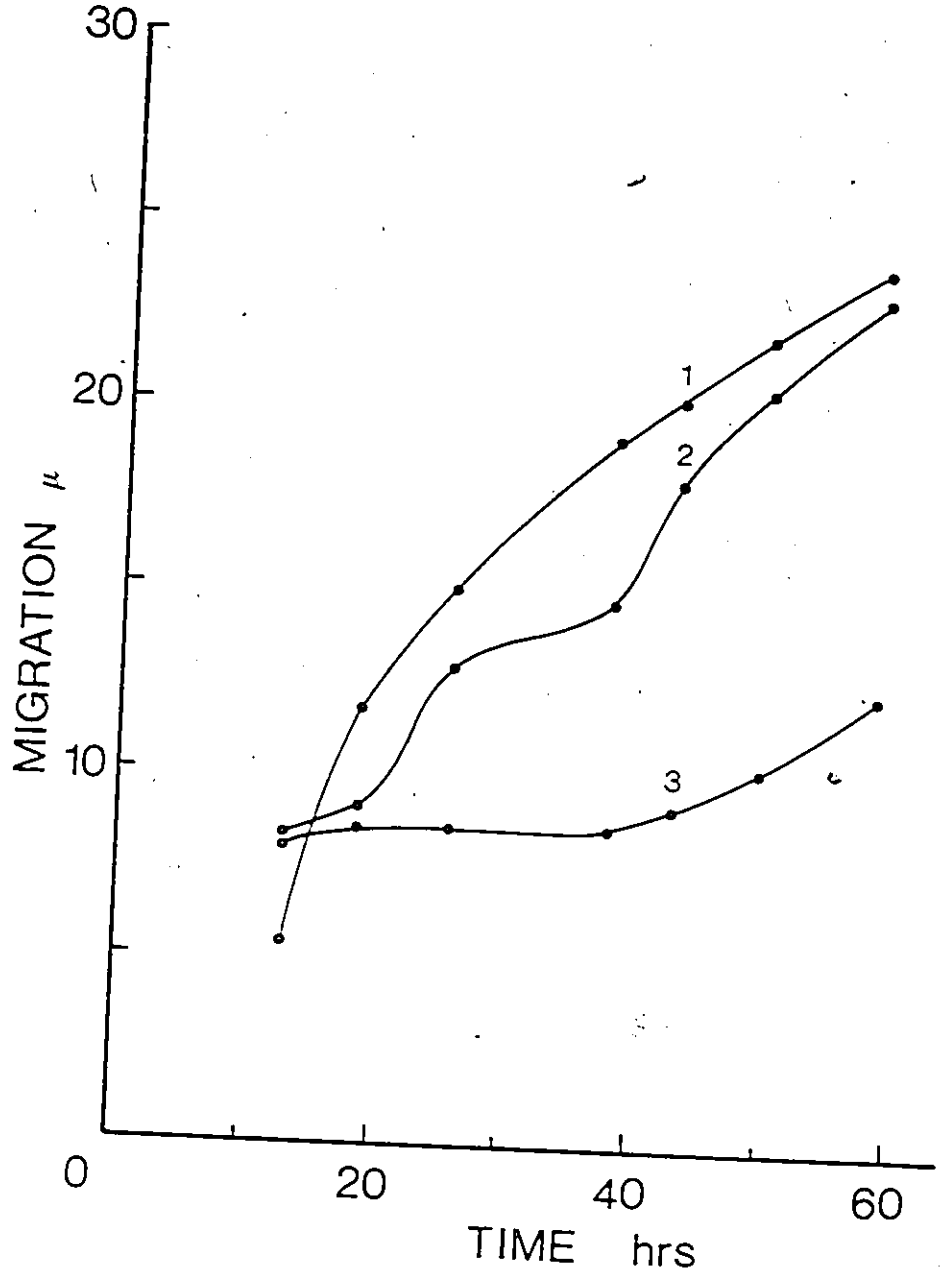

Figure 4.27 Migration and velocity characteristics of CIGM for different boundaries in the same sample in the Al-Zn system at 185°C (Foil thickness 100 um)

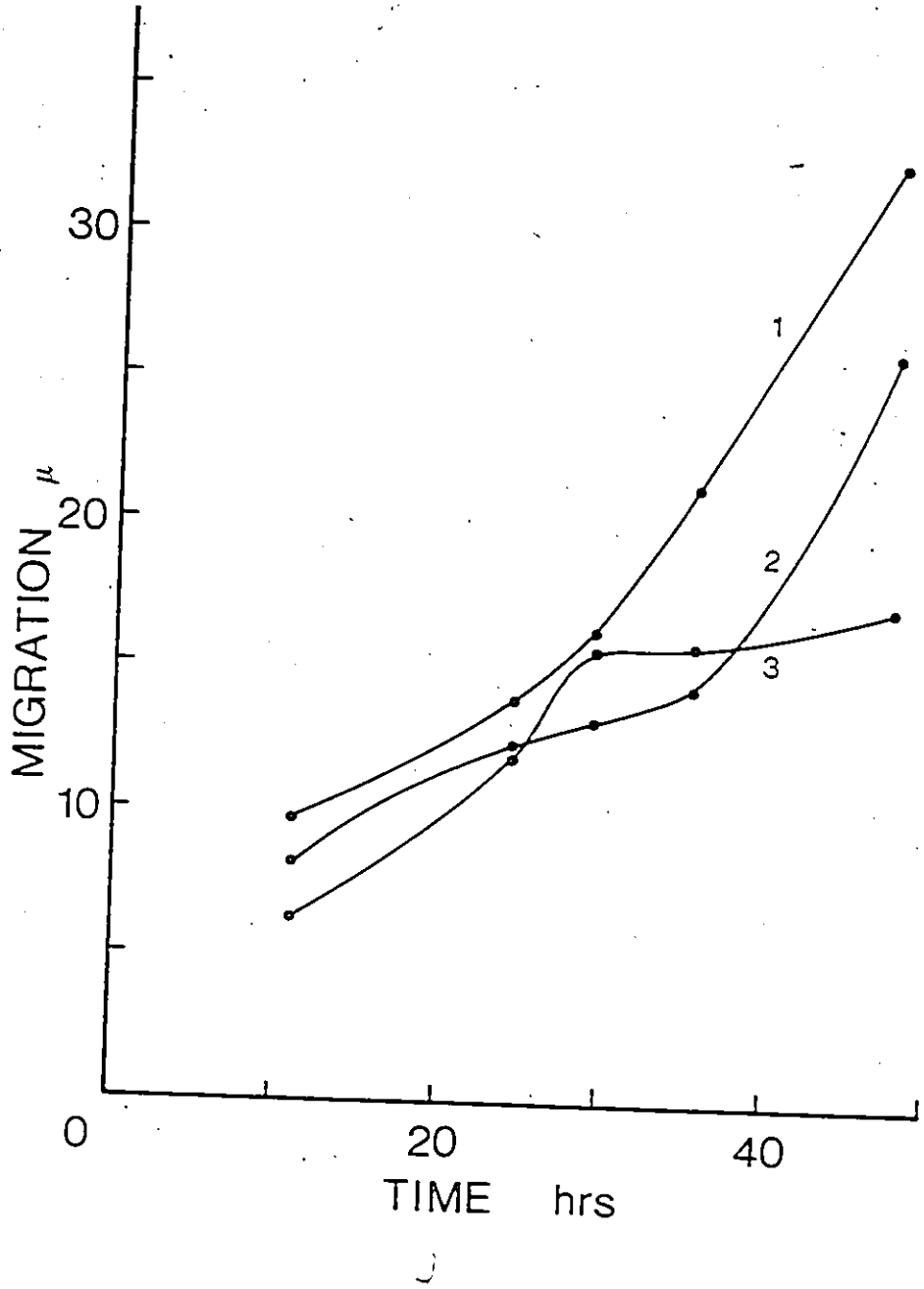

Figure 4.28 Migration and velocity characteristics of CIGM for different boundaries in the same sample in the Al-Zn system at 190°C (Foil thickness 100 um)

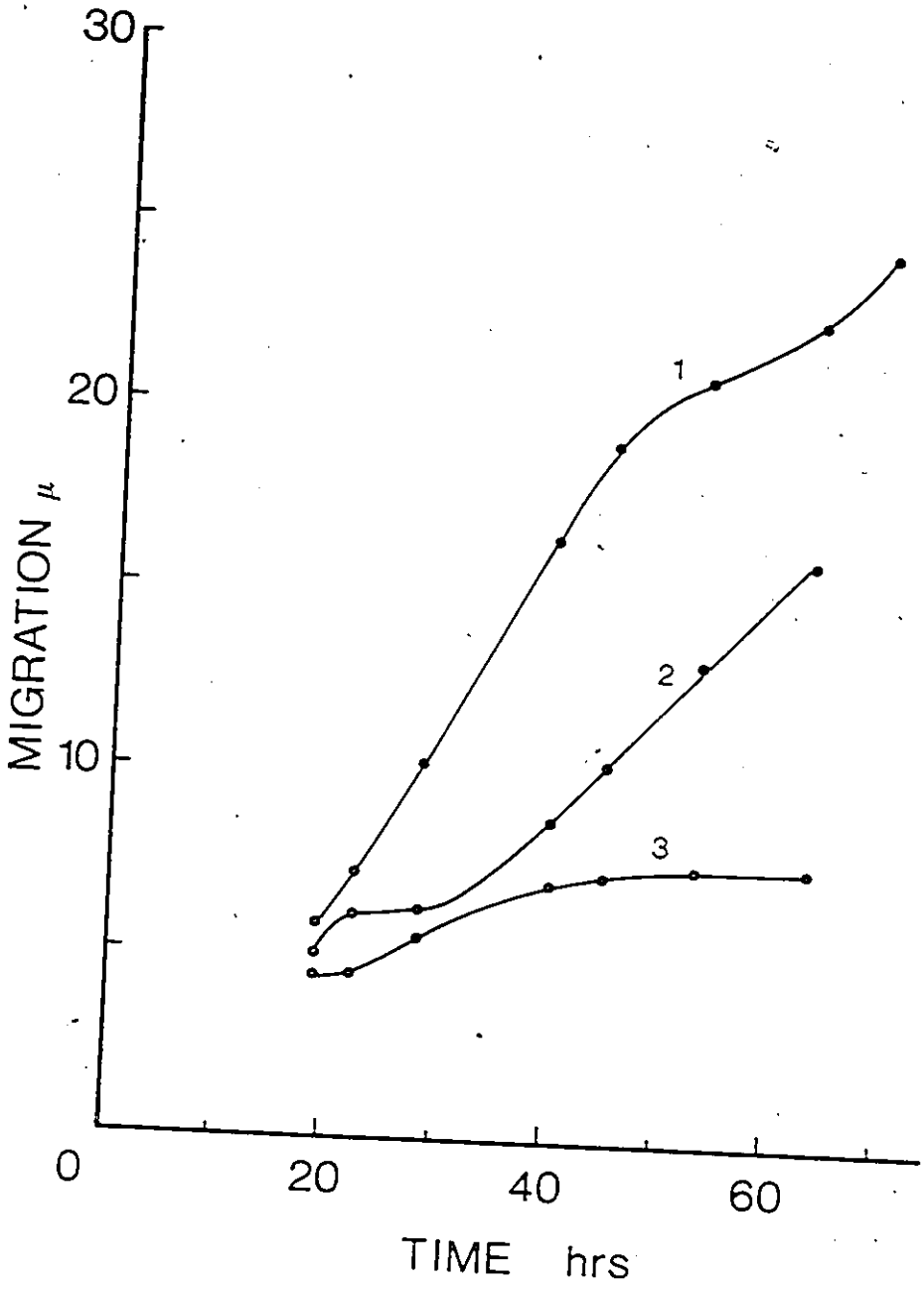

Figure 4.29 Migration and velocity characteristics of CIGM for different boundaries in the same sample in the Al-Zn system at 200°C (Foil thickness 100 um)

4.4 In Situ Observation of Discontinuous Precipitation in the Al-Zn System

The purpose of this study is to monitor the progression of discontinuous precipitation in situ. Then by obtaining the microchemistry of the alpha lamellae, the chemical driving force for the alpha interface can be calculated and then related to loss mechanisms such as spinodal decomposition and capillarity. The velocity measurements on the interface would also be superior to those inferred from static measurements of displacements.

Shown in Figures 4.30 to 4.31 are sequences illustrating the progression of the discontinuous precipitate front. Figure 4.32 illustrates the initiation of a zinc rich precipitate. It was uncertain whether the precipitate was a beta lamella from the discontinuous product nucleating from an unstable situation or a zinc surface precipitate.

A total of five different interfaces were observed at different times during precipitation in the same foil. For each interface, microchemistry was also obtained as shown in Figures 4.33 to 4.37. The first two interfaces shared a common front as well as the last three interfaces. The last two interfaces Figures 4.36 and 4.37 are the same interface measured at different times and which also possess different velocities. In competition with the discontinuous precipitation was spinodal decomposition and what appears as surface precipitation. The spinodal product presented itself in the supersaturated matrix in front of the interface as a mottled tweed-like background. The other zinc precipitate were found to be mainly on the surface of the foil. (This

was surmised as the discontinuous precipitate was observed to be able to pass by the larger surface precipitate.) The discontinuous precipitate interface was observed to exhibit a loss in velocity as it passed underneath but it did resume its normal velocity as the interface emerged from under the surface precipitate.

For each interface studied, the velocity was measured and was found not to be constant throughout the process. This deviation from steady state was also accompanied by changes in curvature of the alpha interface; on occasion the interface was observed to reverse. Microchemistry of the lamellae also indicated that these reverse curvature regions possessed a higher zinc concentration than the other regions of the interface with the normal curvature whose centres of curvature lay in the depleted alpha phase.

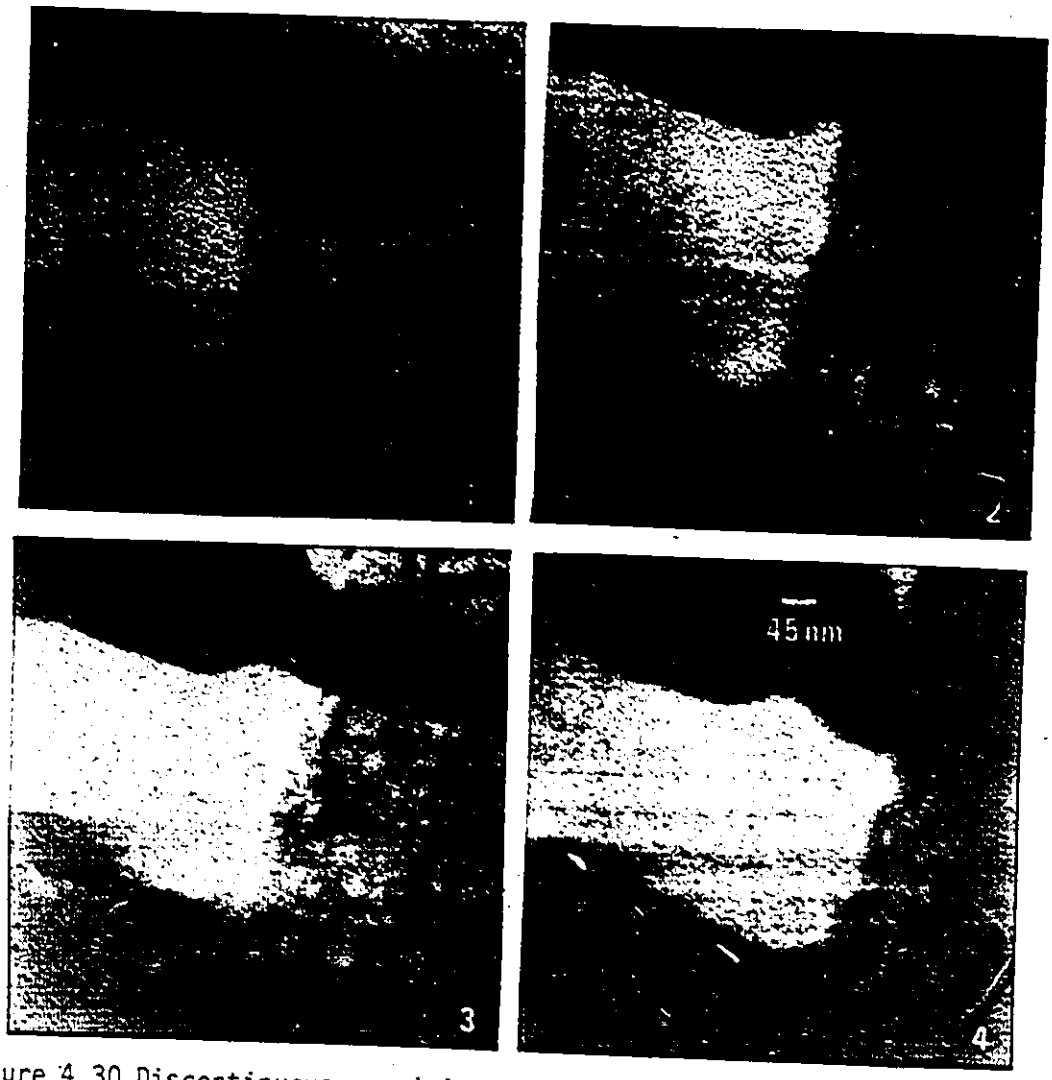

Figure 4.30 Discontinuous precipitation sequence A in a 22% Zn-Al alloy (130°C 15-20 sec. interval)

Figure 4.31 Discontinuous precipitation sequence B in a 22% Zn-Al alloy (130°C 15-20 sec. interval)

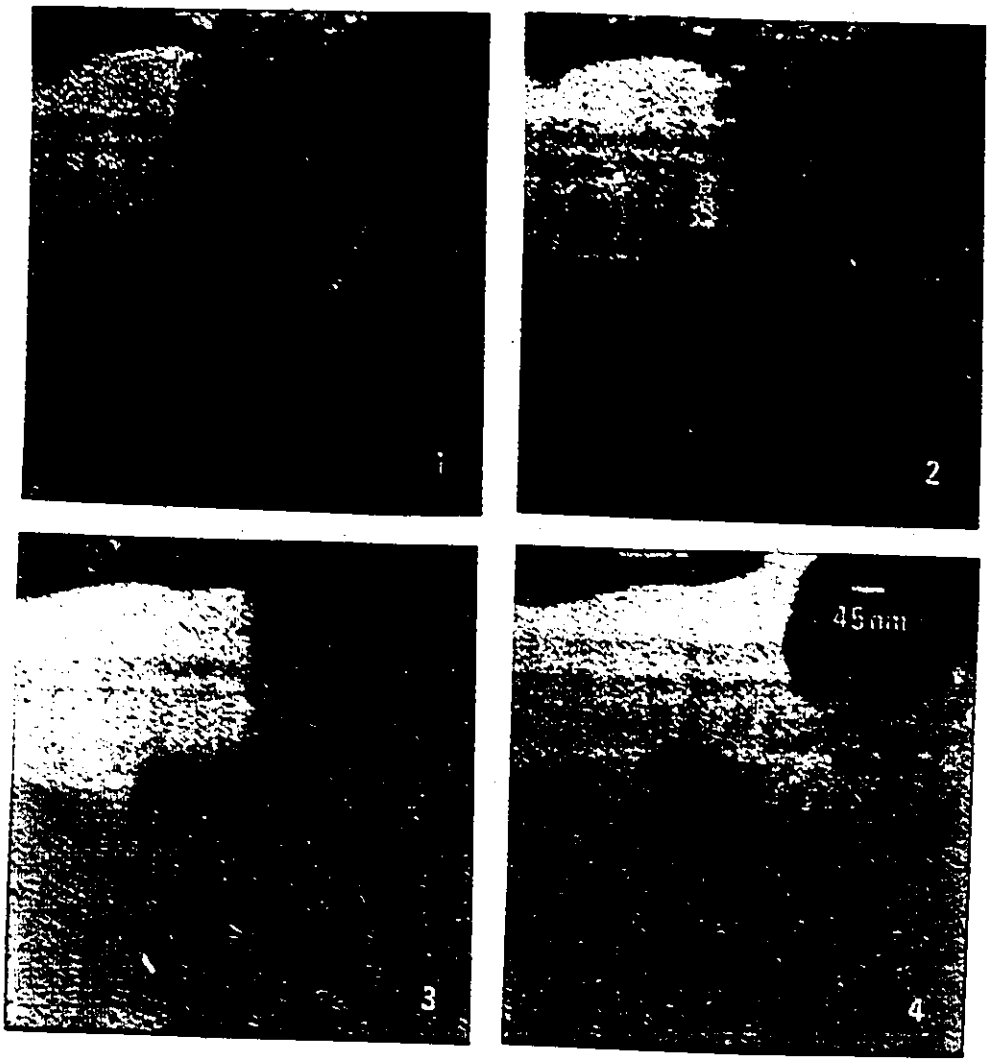

Figure 4.32 Sequence demonstrating the initiation of a precipitate in a 22% Zn-Al alloy (130°C 15-20 sec. interval)

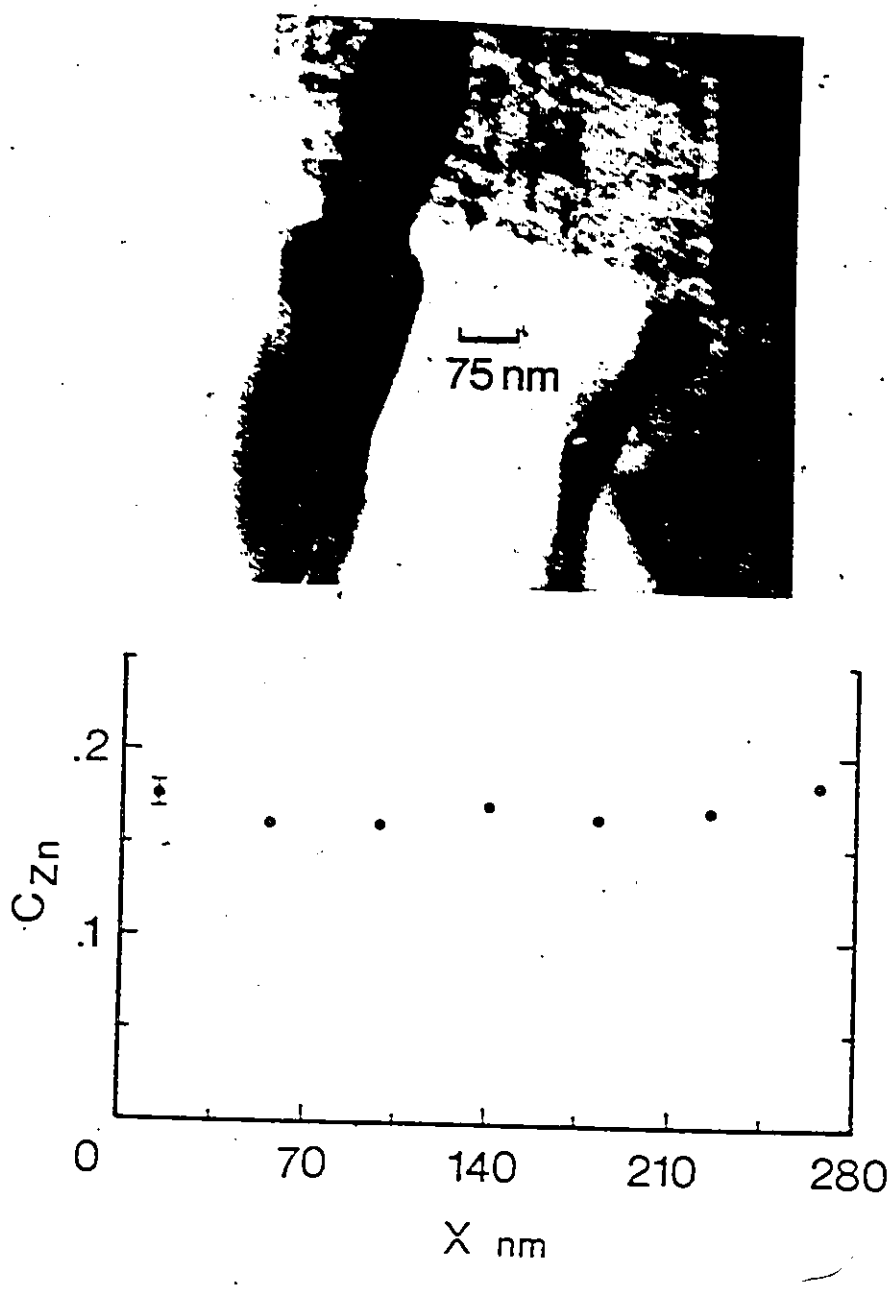

Figure 4.33 Microchemistry and interface profile of alpha lamellae A (130°C v=6.8 nm/s)

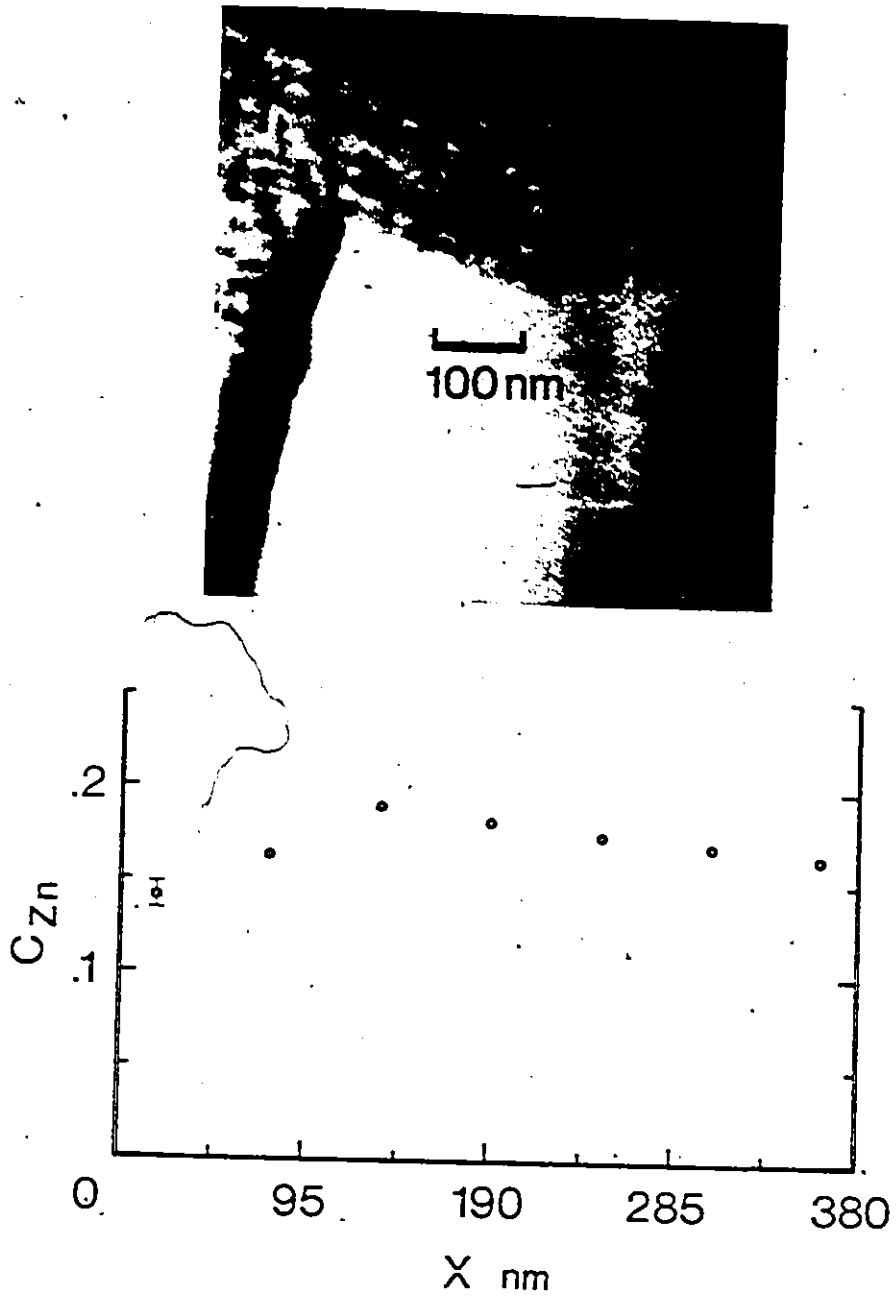

Figure 4.34 Microchemistry and interface profile of alpha lamellae B (130°C v=4.4 nm/s)

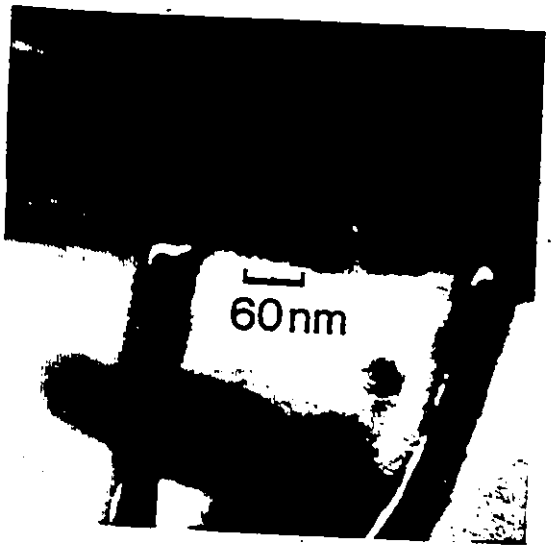

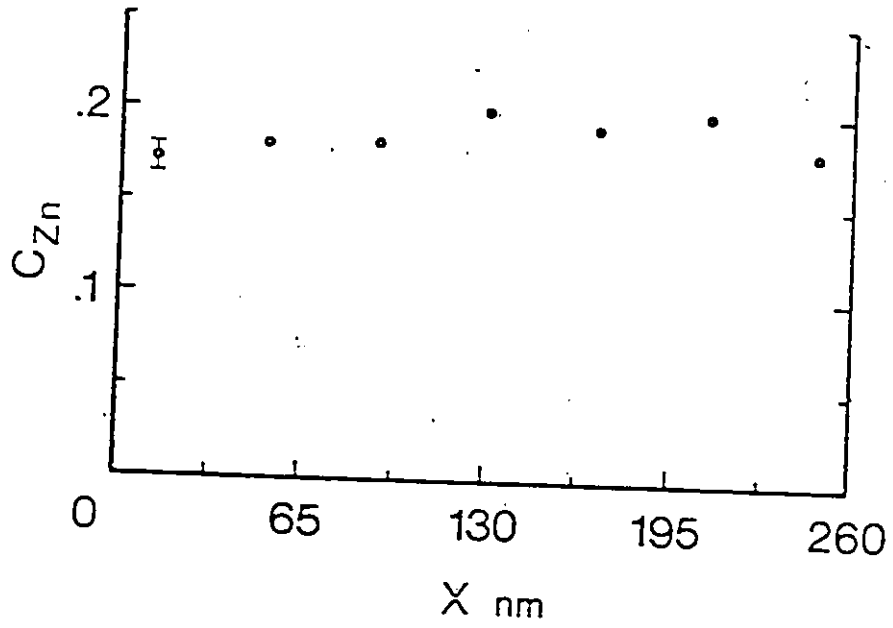

Figure 4.35 Microchemistry and interface profile of alpha lamellae C (130°C v=4.8 nm/s)

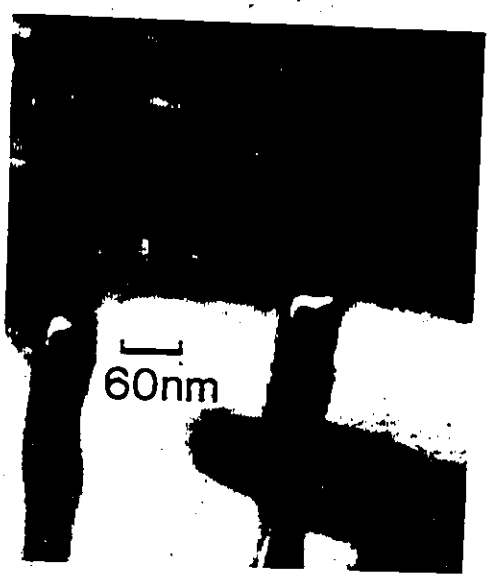

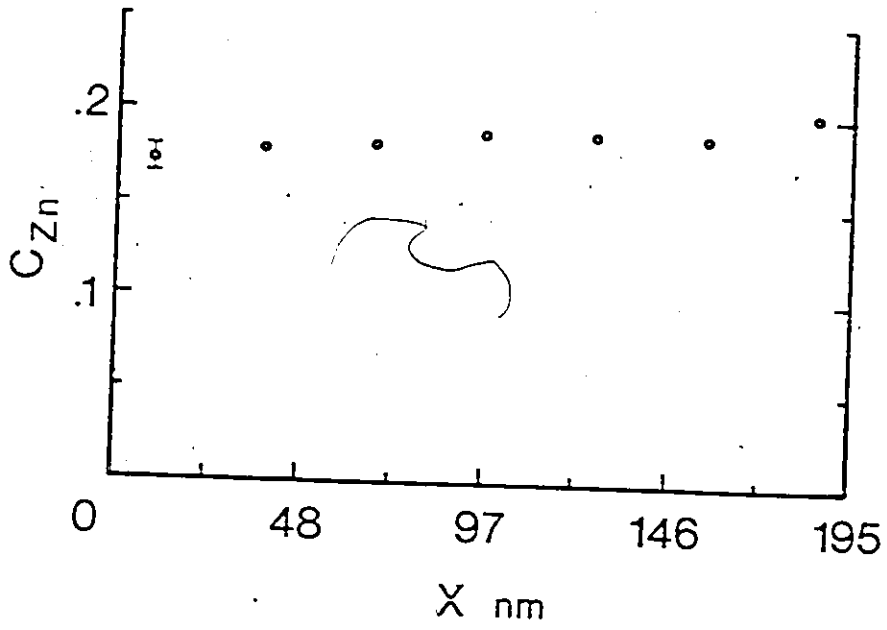

Figure 4.36 Microchemistry and interface profile of alpha lamellae D (130°C v=4.8 nm/s)

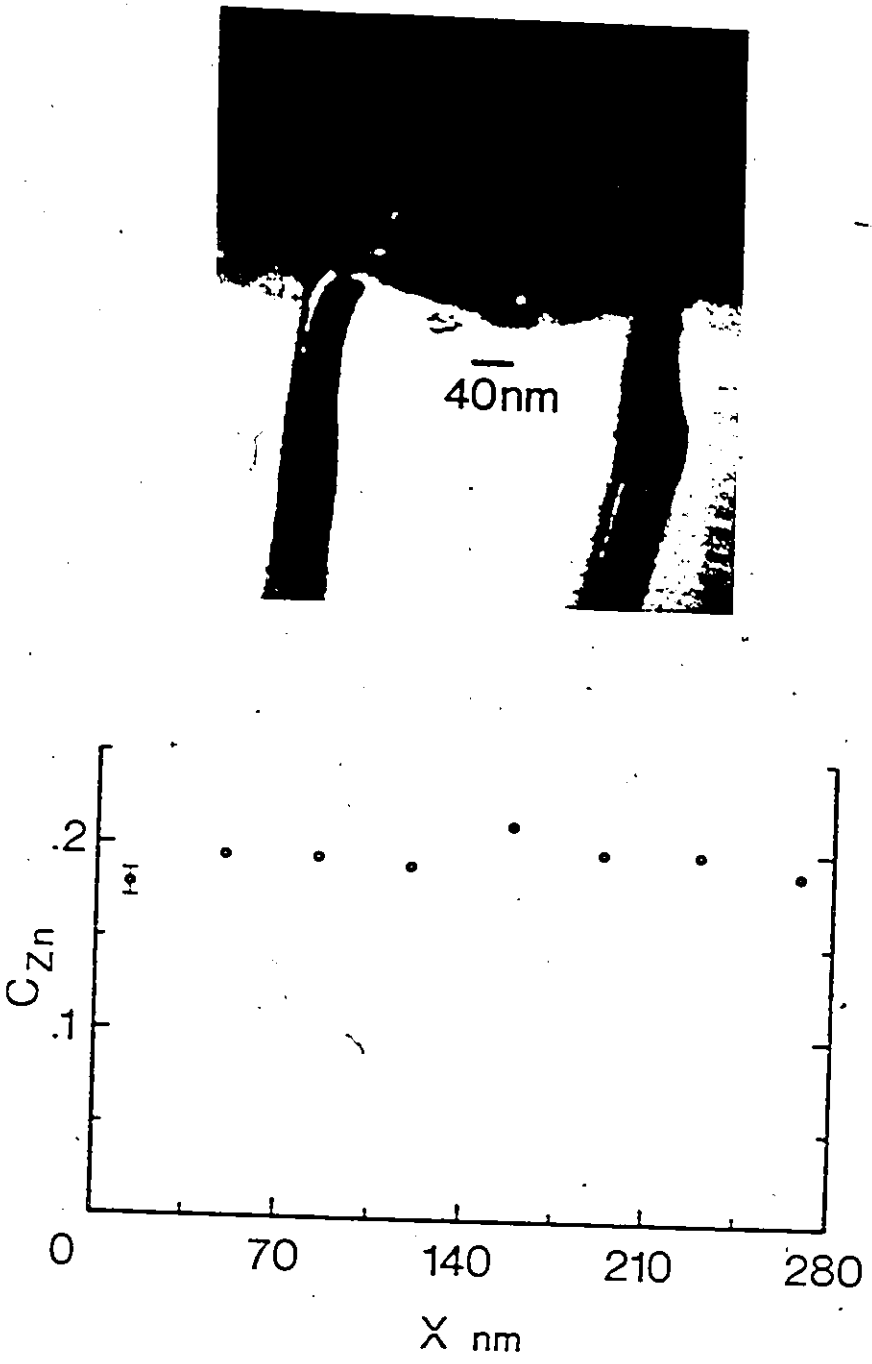

Figure 4.37 Microchemistry and interface profile of alpha lamellae E (130°C v=9.4 nm/s)

4.5 Summary of Experimental Observations

A summary of the experimental observations made in this study are as follows:

<1> CIGM can exist in systems under both a high and low volume diffusion penetration ahead of the migrating boundary.

<2> CIGM cannot be detected (to within experimental limits) in the Ag-Mn system.

<3> The penetration of CIGM into thick samples decreases with increasing temperature whereas migration velocity increases.

<4> A form of CIGM appears on the free surface of aluminum foils with a zinc source.

<5> Surface CIGM in the Al-Zn system appears to possess a higher rate of migration and is foil thickness dependent.

<6> Surface CIGM possesses the ability to break away from surface or sub-surface features which hinder its migration.

<7> The surface features that pin the migrating boundary appear to be created by the boundary and are zinc enriched.

<8> The boundary after migrating for a period may cease migrating altogether.

<9> Experimental evidence suggests that the incubation period before migration may be very small and steady state migration is achieved early in time.

<10> Externally applied tensile stress or the application of a bending moment does not significantly modify the migration of boundaries in the Al-Zn system.

<11> The discontinuous precipitation process competes with continuous

processes such as spinodal decomposition and surface precipitation.

<12> The precipitate formed on the surface of the foil and it affected the discontinuous precipitate interface by slowing it down as it passed underneath.

<13> An interface can double its velocity over a distance of 100-200 nm.

<14> An interface can curve backwards and the microchemistry at that point indicates a greater zinc content than at other points with normal curvature.

CHAPTER 5

DISCUSSION

All the transformations examined in this investigation are characterised by a boundary migrating with simultaneous diffusion along a grain boundary and a compositional step across the boundary. The concept of a grain boundary being driven by a force which is chemical in nature has been the subject of controversy since its inception. It is therefore an objective of this investigation to establish the validity of the chemical nature of boundary migration under conditions studied here.

The experimental observations which have been presented are suggested to illustrate different facets of the same phenomenon, the presence of a chemical driving force which causes a grain boundary to migrate. Migration without the presence of a precipitate at the boundary is suggested to be the purest form of a response to this force and has been examined in the first portion of the experimental observations. However, the presence of a second phase at the grain boundary as in discontinuous precipitation does not diminish the importance of a chemical force in the overall description of the process, as will be demonstrated in the treatment of the second portion of the experimental observations.

Various aspects of grain boundary migration and a chemical force will be examined but the most important and fundamental problems

considered are:

1. The nature of the chemical force which drives pure chemically induced grain boundary migration and the importance of coherency strain energy in the process.
2. How the chemical force can be utilised in describing the alpha interface in discontinuous precipitation.
3. Possible mechanisms for the initiation and cessation of boundary migration.
4. An examination of the problems of uniting present grain boundary structure theories to the macroscopic nature of a chemical force.

Finally, a computer simulation of grain boundary migration employing as many principles concerning the chemical driving force considered in this discussion is developed and compared to experimental observations.

5.1 Chemically Induced Grain Boundary Migration

The first portion of the experimental observations examined different aspects of chemically induced grain boundary migration. Consider the solute behaviour of the new systems investigated in this study first. Shown in Table 4.2 is the D_v/v parameter which indicates the degree of solute penetration from the moving boundary into the unalloyed bulk material ahead of the boundary. If the penetration is less than 0.5 nm, no solute penetration is assumed. As shown in the table, the interface for various systems possesses either a large solute field ahead of it or none. Therefore, the interface is either "fully

relaxed" by volume diffusion with the coherency strain energy effect possibly operating or a large concentration step exists across the boundary. If a chemical force is the dominant force which is operating in both cases, then these conditions must represent extremes in the level of the chemical driving force. Therefore, the magnitude of volume diffusion and boundary velocity will dictate the extent of solute penetration. Thus, the conditions (eg. temperature) which determine the degree of relaxation and therefore the strength of the force will be designated as the low and high chemical force conditions. The definition of the chemical driving forces in each case is demonstrated using free energy diagrams as shown in Figure 5.1. In each case, the driving force is the same in nature and is chemical in origin; what differs is the concentration difference across the boundary which defines the chemical driving force. It was originally suggested that migration could exist for the high force conditions only (C29,C30). However, subsequent migration under low force conditions was found in the aluminum-zinc system by the author (37) and in the Cu-Ni system by den Broeder (C9). The principle that the chemical force is universal would be strengthened if the extremes in the force could be proven to exist in the same system. Systems such as Ag-Pd and Pt-Pd exhibit migration of the grain boundary under both possible extremes of the chemical force. This then raises the question of the transition which may exist between the two force states. The transition range is expected to occur over a small range in temperature and the details of the transition behavior will be considered in a later section.

Assuming that a chemical force is responsible for driving a

grain boundary, then the magnitude of the force must be able to at least predict the presence of boundary migration or not. Fortunately, this has been experimentally substantiated by Yoon et. al. (C46) for liquid films and by this work for the low force conditions. In particular, if the total driving force can be minimised or made to vanish, then migration should also be similiarly influenced. Under these conditions, the driving force is determined mainly by the square of the product of the misfit parameter and the alloy concentration as given by equation 2.46. A comparison of this parameter product for various systems is given in Table 5.1. In both this work and Yoon's, the misfit parameter is very small or is made to vanish which results in the absence of boundary migration.

Table 5.1 Comparison of System Misfit

System	v	Misfit	Temp
	pm/s	1E6	°C
Ag-Cu	18	5.8	500
Ag-Mn	0	0.03-0.1	500
Au-Ni	23	35.0	500
Au-Pd	26	1.1	500
Al-Zn	25	0.5-0.8	195

The table indicates that the available driving force is small for the Ag-Mn system as comparable to other systems. This in itself may be the reason that migration was not observed. However, it might be suggested that this reason alone is inadequate since, there may have also been an initiation barrier to the migration process in both the Ag-Mn system and in those studied by Yoon et. al.

It is necessary to consider all of the possible effects that may be present at a grain boundary in the fully relaxed state. A major effect postulated is the establishment of the coherency force at the boundary. In addition, it has been proposed by Tashiro and Purdy (C37) that migration may be produced by a defect flux which flows normal to the boundary. This defect or vacancy flux to the boundary is a result of a bulk Kirkendall effect ahead of the boundary under relaxed conditions. This flux then is capable of inducing climb of the grain boundary dislocations as described by Balluffi et. al. (C7) to produce migration even under these conditions. Such a mechanism would allow migration by the dislocation mechanism under all conditions. However, this premise was weakened by the observation of CIGM in the Ag-Cu system. The overall migration rates are comparable to those in other systems under fully relaxed conditions but the bulk Kirkendall effect is very small.

This section has been mainly concerned with the existence of a chemical force which arises due to coherency strain effects at a fully relaxed grain boundary. The experimental evidence indicates that this force is applicable and can be used to predict some migration behaviour. However, in order to be complete, other possible reasons for migration to occur under a constrained equilibrium state must also be examined. The effects of a defect flux normal to the boundary has been examined and determined not to be a dominant factor in migration. There exists the distinct possiblity that the coherent strain energy which is used to define the chemical force may also be used to drive the boundary directly.

Generally, there are very few effects or forces which can act

upon a grain boundary under these conditions to produce migration. The chemical force appears to be the most tenable possiblity. However, other possible forces may exist but at this-time, they are not as obvious as the chemical force.

5.1.1 Enhanced Migration at a Free Surface

It has been shown that enhanced migration occurs at the opposite surface to the solute source. It is unknown at this time how this effect is related to the enhanced migration at the solute surface in vapour source experiments or in diffusion induced recrystallization. Examination of the observed behaviour of surface migration suggest that a steady state velocity can be established early and that the incubation time required is very small or non existent. Perhaps one of the more intriguing facets of surface migration is apparent pinning of the boundary near or at the surface as shown in Figure 4.24. The velocity decreases dramatically and as a result the alloy concentration increases. The cause of the boundary velocity reduction has not been determined definitely. It is suggested that this effect is a result of one of the many possible cessation mechanisms operating. These mechanisms are to be considered in a later section.

A possible mechanism for enhanced migration at a free surface also finds its basis in a chemical force derived from a coherency strain energy effect. Apparent enhancement is suggested to be the result of the inhibition of migration in the bulk and not a different driving force present upon the boundary at the surface. It has been shown in previous work by the author (C37) that a misfit dislocation network does not form at the original boundary position as in other CIGM systems. This

suggests that the coherency strain energy of the compositional gradient which forms at the original boundary position has may not have been totally relieved. It is therefore possible that the alloyed grain possesses a residual coherent strain energy which can reduce the overall driving force on the boundary. If the fraction of coherent strain that remains is f(x), which is assumed to be a function of distance along the boundary, then free energy available to drive the boundary is calculated (Appendix D) to be:

$$\Delta G_a = (1-f(x))\ E\ V_m\ \eta^2\ x_d^2/(1-\nu) \qquad (37))$$

The difficulty is determining a reasonable estimate of f(x) which relates the effective retained coherency strain in the daughter phase and most important, the effective relief of strain at the surface.

The greater migration at the free surface is suggested to be a result of the partial relief of strain in the daughter at the surface. Therefore, a large fraction of the coherency derived chemical driving force can operate upon the boundary at the surface. At a free surface, relaxation can occur easily since there are fewer constraints present. Therefore, the coherency strain remaining in the compositional gradient at the original boundary position can be relieved more easily. However, the coherency strain produced by the solute profile ahead of the boundary may may also be relieved by dilatation. Therefore, all the driving force for the migration of the boundary could conceivably be removed.

The situation at the free surface also allows a solute flux along the free surface (actually a metal-oxide interface) and subsequent penetration into the bulk as shown in Figure 5.2. This extra solute

concentration profile is supplied from the moving boundary and is continuously replenished by movement. The extra solute concentration profile produces a strain which is not as easily relieved at the free surface. The concentration gradient produced by solute flow normal to the boundary produces a strain field which can be relieved by one of the possible cessation mechanisms to be considered later and by dilatation normal to the boundary (it is not constrained in that direction). However, the concentration gradient normal to the surface cannot relieve its strains in this manner. Therefore, a larger chemical force derived from a larger coherency strain energy difference is present and can drive the surface boundary to greater displacements.

The presence of the oxide film is suggested to have a limited effect upon migration. The film is expected to provide a barrier to zinc during in situ examination of the foil under vaccuum. Since it is very thin, it is not expected to modify the coherency strain fields extensively when compared to a free surface.

This section has developed the concept that a grain boundary can be driven by only part of the total chemical energy available from a coherency strain field. The concept of retained chemical energy stored in the form of strain energy is not exclusive to chemically induced grain boundary migration but can be found in many other transformations which will be considered in the next section.

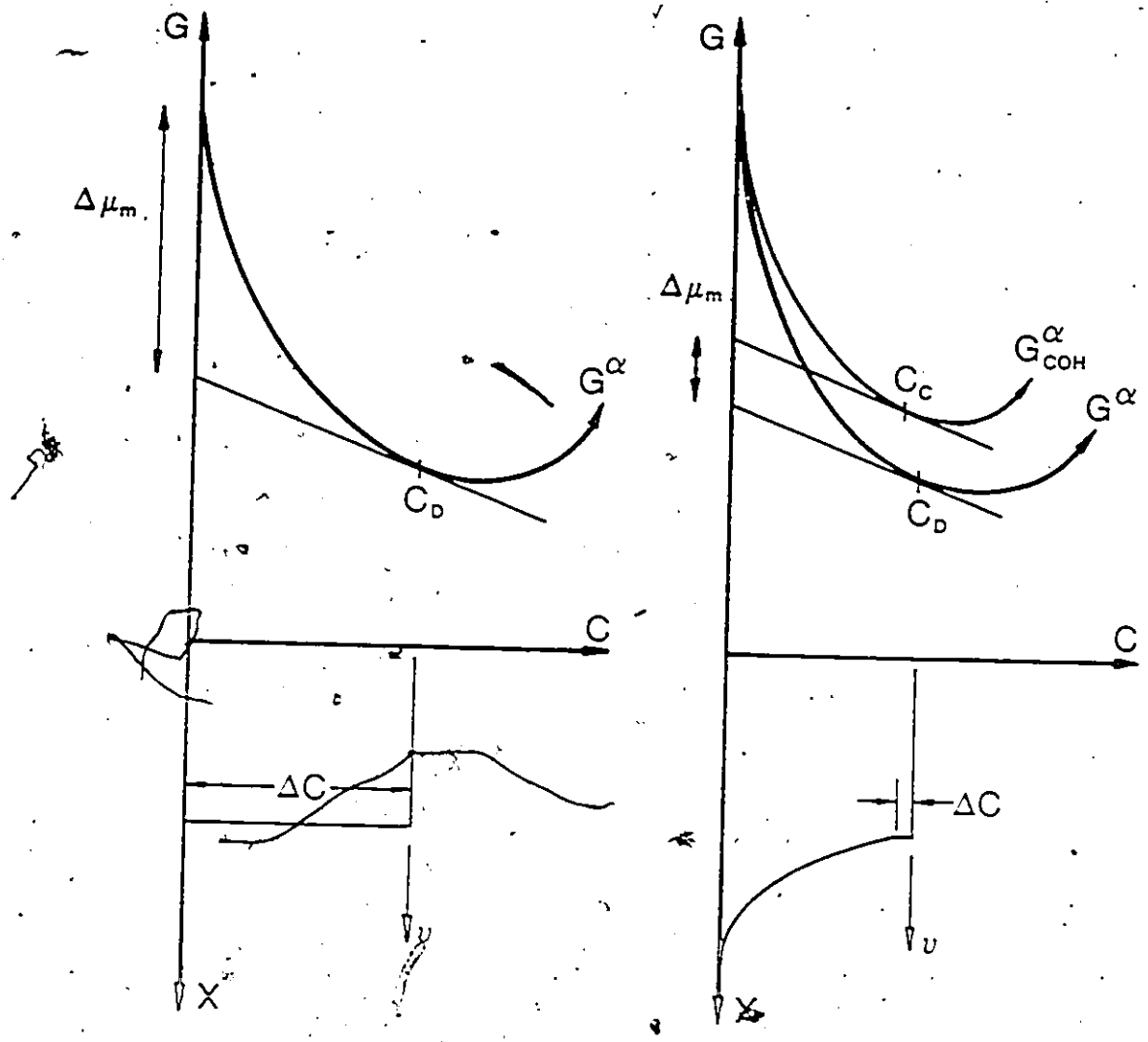

(a) High Chemical Force (b) Low Chemical Force

Figure 5.1 Free energy diagrams illustrating the (a) high and (b) low chemical force. In (a) a large concentration step exists across the boundary and in (b) the step is reduced to a small value as determined by the coherency strain energy.

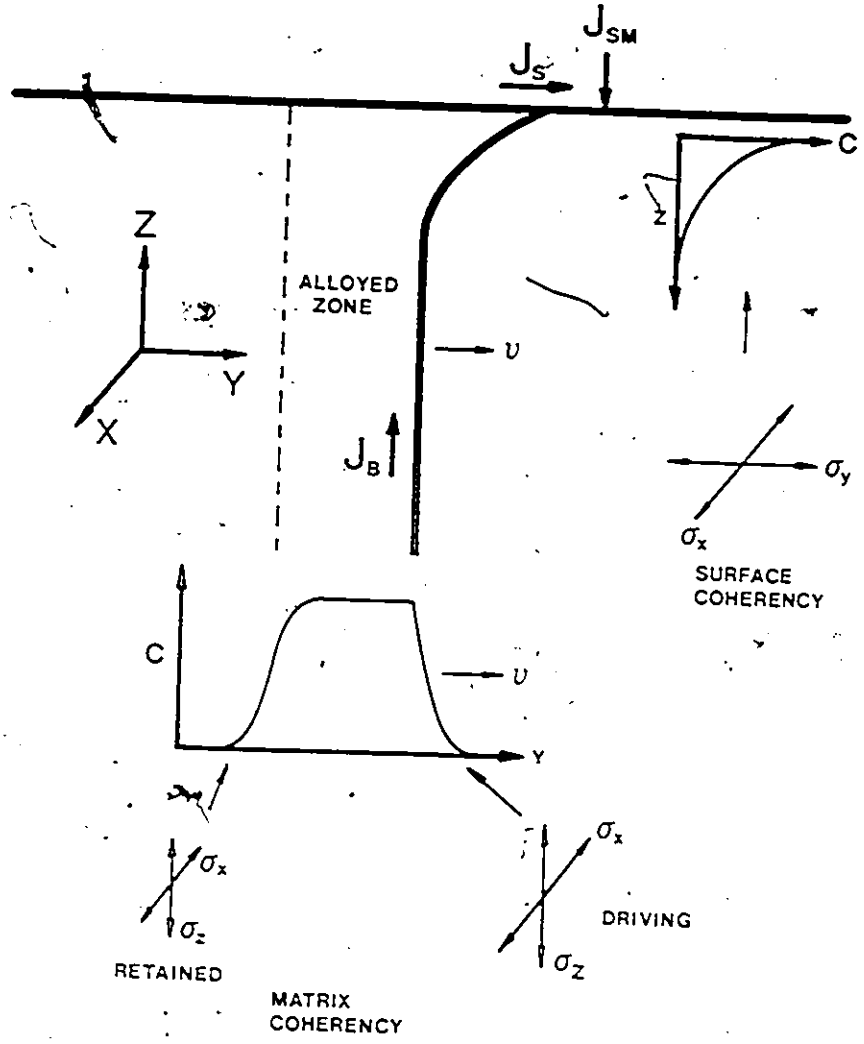

Figure 5.2 Enhanced migration at a free surface. Due to failure to relax all the coherency at the original boundary position concentration profile; a certain amount of coherency strain is retained. However, at the free surface, an additional concentration gradient is produced by surface diffusion (J_S) and subsequent volume diffusion (J_{SM}) from the free surface. This additional concentration gradient also possesses a coherency strain energy which is not totally relieved at the surface. Therefore, the chemical driving force is greater at the surface resulting in a greater displacement of the boundary.

5.2 Chemical Driving Forces in Discontinuous Precipitation

It is generally accepted that a chemical driving force is responsible for the migration of the beta interface, however, this has not been as readily accepted for the alpha interface. This section will assume that a high chemical force operates upon the alpha interface and will attempt to describe how this force interacts with other forces at the interface. In particular, Hillert's premise that local chemical forces on the alpha interface must balance with local capillarity and mobility terms will be examined.

The balance of forces at the interface was suggested by Hillert to manifest itself predominantly in determining the interface shape. If chemical force is balanced only by capillarity at a given point, then the interface will possess a well defined curvature at that point. This curvature (r) is defined as:

$$r = \gamma/\Delta G_c \qquad (5.2)$$

where γ is the surface energy and ΔG_c is the available chemical energy. This relationship must hold over the total alpha interface.

In order to calculate the final interface shape, the chemical driving force along each point of the interface must be determined first. Using thermodynamic data for the Al-Zn system as given by Hultgren and others (D6), the total chemical free energy curve was calculated for both the alpha and beta phases at the temperature of 130°C as shown in Figure 5.3. The beta phase is modified by capillarity as shown in Figure 5.3 which yields a new equilibrium concentration at the alpha beta interface in the discontinuous product. This value was

estimated experimentally by Solorzano et al (B3) and theoretically by Hillert (B2). These values were used as boundary conditions for each end of the alpha interface. The actual amount of chemical free energy available for capillarity balance can be estimated using the following technique. Using the concentrations across the lamellae which were determined by microanalysis and the capillarity modified alpha-beta interface equilibrium concentration (B3), the total chemical free energy available was calculated for a number of points along the interface as illustrated in Figure 5.4. This energy would represent the absolute maximum energy available for the interface. However, not all of this energy is available. Since spinodal decomposition is unavoidable in this alloy system, a portion of this energy is dissipated.

In the process of spinodal decomposition, there are three energy terms which must be considered. These energy terms are:

(1) Chemical free energy lost due to decomposition to the equilibrium state.

(2) Stored coherent strain energy due to the strain field produced by the large compositional changes.

(3) Stored gradient energy which is related to the slope of the compositional gradient.

The sum of these three terms will yield an estimate of the total free energy lost. The chemical free energy loss is estimated by assuming that the system will attain a chemical equilibrium state quickly. This assumption is substantiated by examining isothermal aging characteristics (B11) for similiar Al-Zn alloys. The process is nearly

complete for the temperatures and times used in these observations. The final decomposition product is assumed to possess a nearly square wave profile as shown in Figure 5.5 with the limits being defined by the equilibrium (coherent) points. The coherent strain energy (E_s) and the gradient energy (E_g) terms can be estimated for this profile as given in Appendix E. The chemical free energy loss due to decomposition (G_{C1} ~227J/mole) is shown in Figure 5.6 and produces the chemical phase boundary points. When the coherent strain energy is added, equilibrium is again assumed and in this instance produces the coherent phase boundary points for this temperature. The new energy loss (G_{C2}) is reduced by the coherency strain energy (E_s). Finally, the gradient energy (E_g) term is added to the final result to give the total energy loss as 72 to 122 J/mole.

The final interface shape was calculated by employing linear interpolation for the curvature between the determined points. The final interface shapes for the five observed interfaces are given in Figure 5.7 to 5.11. It can be seen that good agreement concerning interface shape can be attained. However, there is the inconsistency in the amount of chemical energy available for driving the individual interfaces observed. Concerning lamellae A and B, they are measured from the same interface at different positions and lamellae C,D and E are measured from a different interface at different positions and times. Within the same group, there is reasonable agreement in the total chemical energy driving the interface. Lamellae C and D agree well as they are from the same interface and possess the same velocity whereas lamellae E was

measured later but possessed a greater velocity. The variations may be due to spinodal aging effects such as coarsening of the compositional fluctuations. However, the total measurement time was short and therefore, if the energy loss due to the spinodal reaction is assumed constant (and if mobility terms were significant), then variations in the energy removed would be expected between different interfaces and a higher interface velocity would require a smaller amount of energy lost. Therefore, it is possible that interface mobility is playing a role as a free energy sink in this set of experimental observations. Quantification of the mobility would not be significant due to the limited number of observations available and the errors involved in the calculations.

The recessive interfaces or those interfaces whose centre of curvature are ahead of the interface are generally found to be more sensitive to the amount of energy removed during the interface shape matching procedure. Microanalysis of the alpha lamella behind recessive interfaces consistently exhibit greater solute concentrations than their convex counterparts. For these areas to be greater in concentration, the solute flux must be towards the recess centre. It has also been suggested (B7) that the higher solute concentration at these areas provide sufficient solute to nucleate, heterogeneously at the grain boundary, a new beta lamellae. The nucleation event will be controlled by the alpha phase reaching a critical concentration behind the recess. In order to reach this concentration, it is envisioned that the velocity of the boundary must be such that the depth of the recess increases in

order to provide a greater boundary area to supply solute to the recess. It is clear that a considerable amount of drag is placed upon the boundary due to the recess. Once nucleation has taken place, The drag is removed and the interface is expected to move freely and with greater velocity as suggested by the nucleation event of Figure 4.36.

The interface shape calculations also produce the angle of the alpha lamellae from the alpha-beta interface normal. The angle calculated is not consistent among the different interfaces. This may be a calculation artifact since the angles are extremely sensitive to the lamellae width. However, it may also represent the non cooperative nature of the colony observed. It has been assumed that the integrated interface curvature is balanced equally at each end by an arbitrary fraction of the surface tension. This fraction has been termed "L" by Hillert (B1) and is illustrated in Figure 5.12. It is suggested that the surface tension fraction at each end may not be shared equally in a non cooperative colony.

Since the observation of discontinuous precipitation was in a thin film, numerous thin film effects are possible. Generally, it has been found (B3) that the measured lamellar spacing does not seem to differ radically from those measured in the bulk. Therefore, the basic thermodynamics of the process may be only slightly affected. A certain amount of strain relaxation is anticipated but the oxide layer is suggested to minimise this effect. A degree of freedom has been removed from the growth process since the discontinuous product is constrained to a thin sheet. Therefore, preferred growth directions are most likely

not selected. However, the major point of the analysis is a test of an interface force balance relationship which should be valid regardless of the experimental conditions.

Generally, it has been demonstrated that the assumption of a chemical driving force for the alpha interface is viable. The chemical force has been calculated locally and used to predict interface shapes which are within experimental and estimation errors.

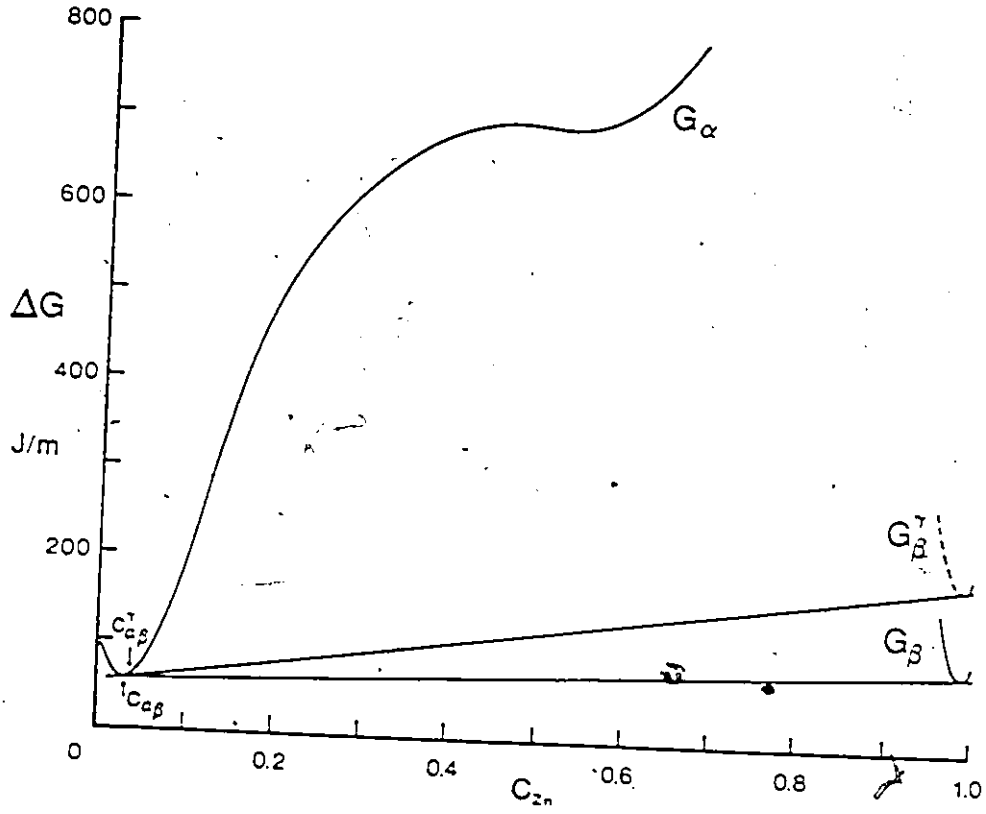

Figure 5.3 Free energy curve for the Al-Zn system at 130°C for the alpha and beta phases. The concentration of the capilliarity modified alpha phase $C_{\alpha\beta}$ is shown as well.

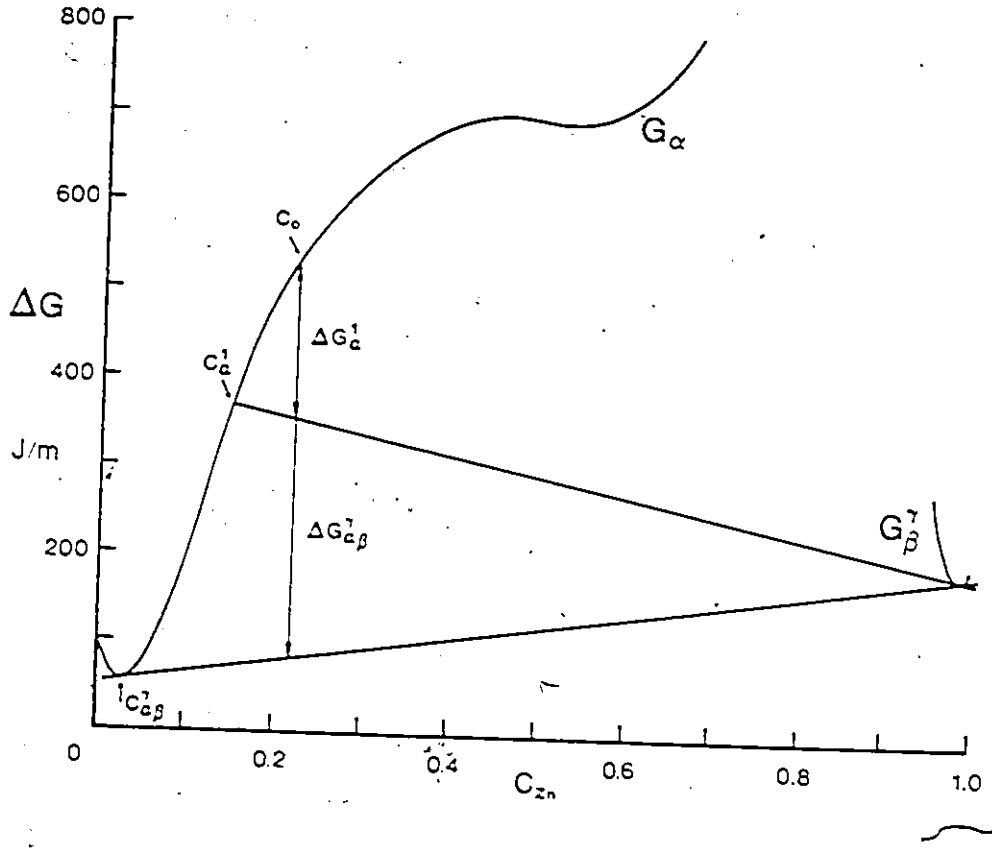

Figure 5.4 Free energy diagram constructions illustrating the determination of the chemical force which is balanced by capillarity forces. Two calculation points are given (a) at the beta lamellae and (b) at an arbitrary midpoint. Co is the average alloy concentration, C_α^1 is the arbitrary midpoint concentration, ΔG_α^1 is the energy available for balancing by capillarity and $\Delta G_{\alpha\beta}^\gamma$ is the stored chemical energy due to supersaturation.

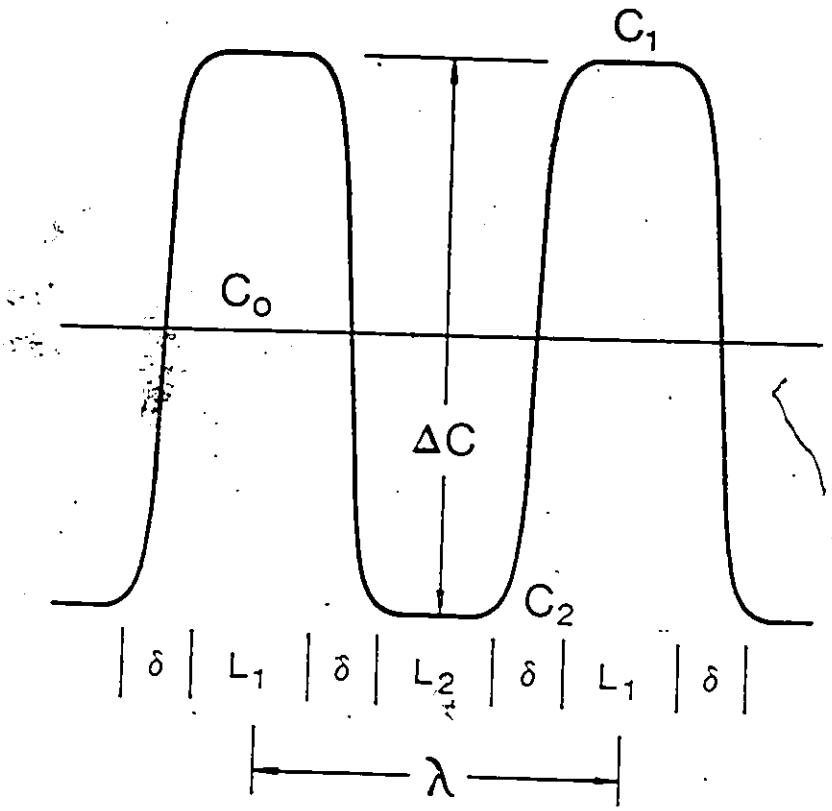

Figure 5.5 Compositional profile for an alloy undergoing spinodal decomposition and its associated model parameters. A square wave profile results as the process nears completion. Further aging results in coarsening of the fluctuations.

λ: characteristic wavelength
δ: interface width
C_1, L_1: highest concentration fluctuation and size
C_2, L_2: lowest concentration fluctuation and size

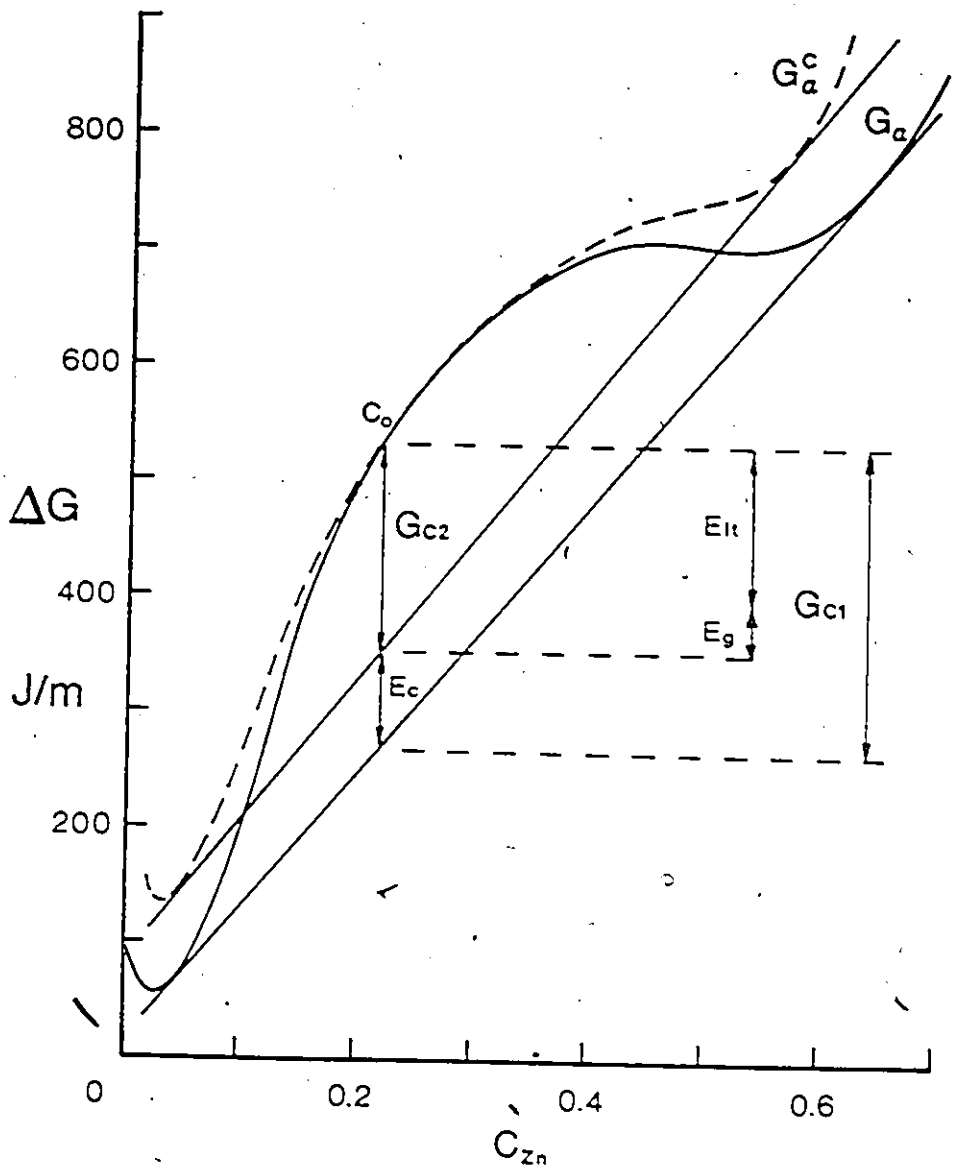

Figure 5.6 Free energy diagram constructions illustrating the determination of the chemical free energy available for driving the interface after spinodal decomposition has been accounted for. G_{C1} is the maximum chemical energy loss due to decomposition. G_{C2} is the loss after coherency is accounted for. E_C is the coherency strain energy and E_g is the gradient energy term calculated in Appendix E.

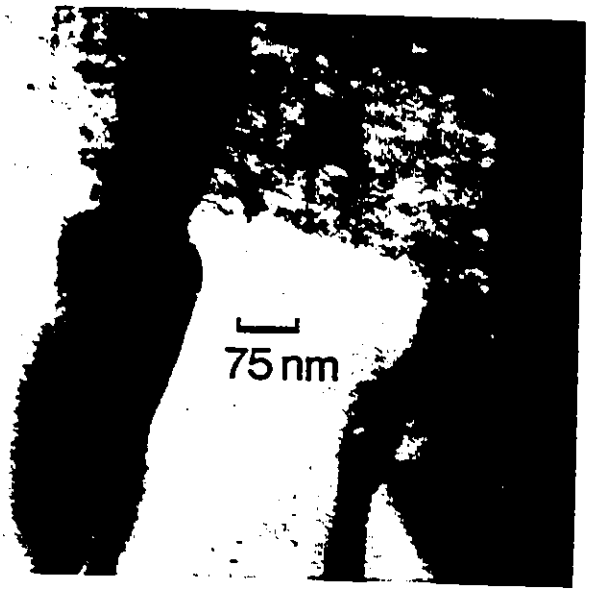

(a)

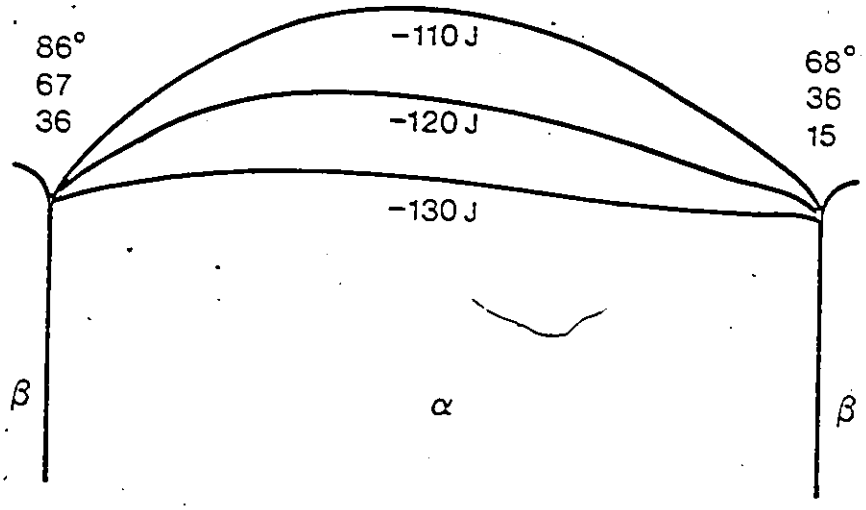

(b)

Figure 5.7 Final calculated interface shape for lamellae A. (a) is the experimentally observed shape and (b) is the calculated shapes. The number associated with each shape indicates the amount of energy removed due to continuous processes. In this particular case, 120 J/mole represents the best fit. (v=6.8 nm/s) (Alpha triple point angle for each end also indicated.)

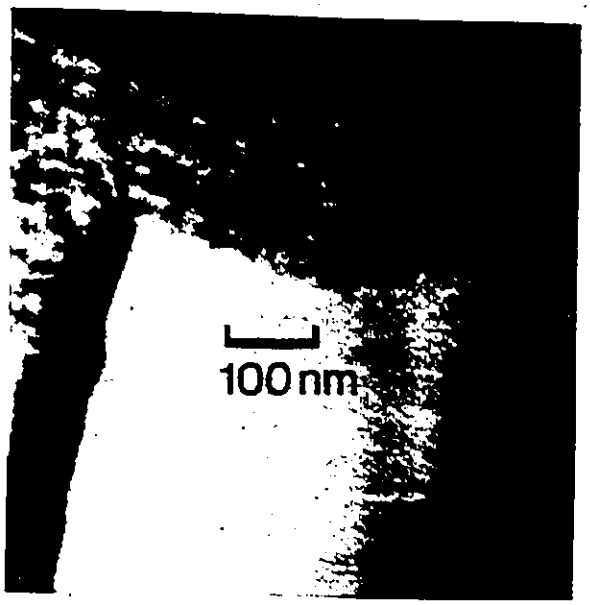

(a)

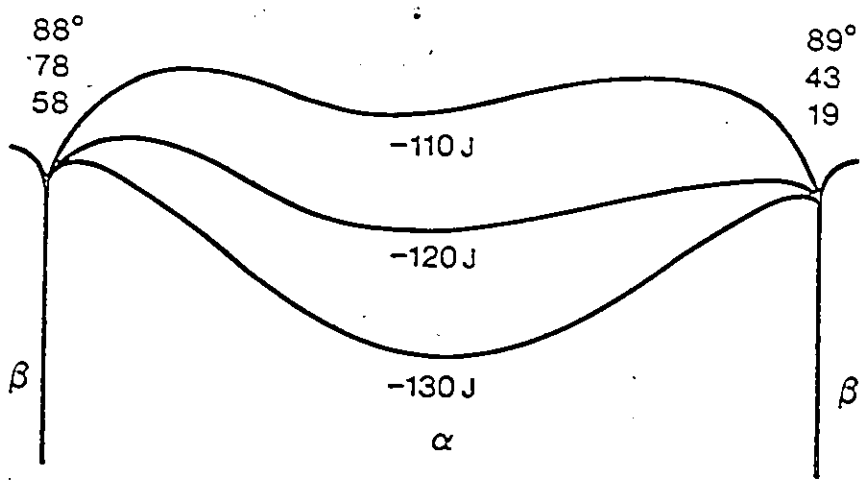

(b)

Figure 5.8 Final calculated interface shape for lamellae B. (a) is the experimentally observed shape and (b) is the calculated shapes. The number associated with each shape indicates the amount of energy removed due to continuous processes. In this particular case, 120 J/mole represents the best fit. (v=4.4 nm/s)

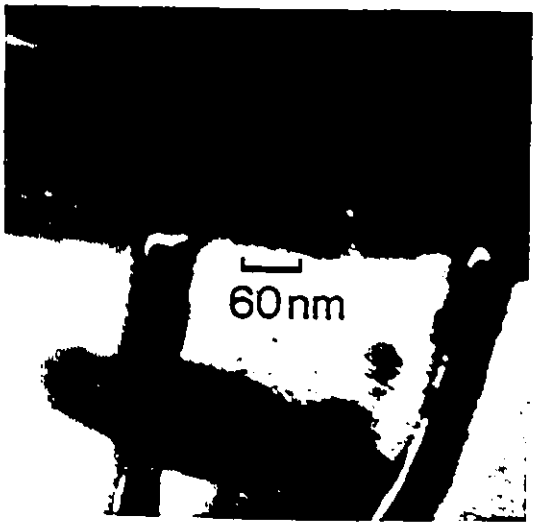

(a)

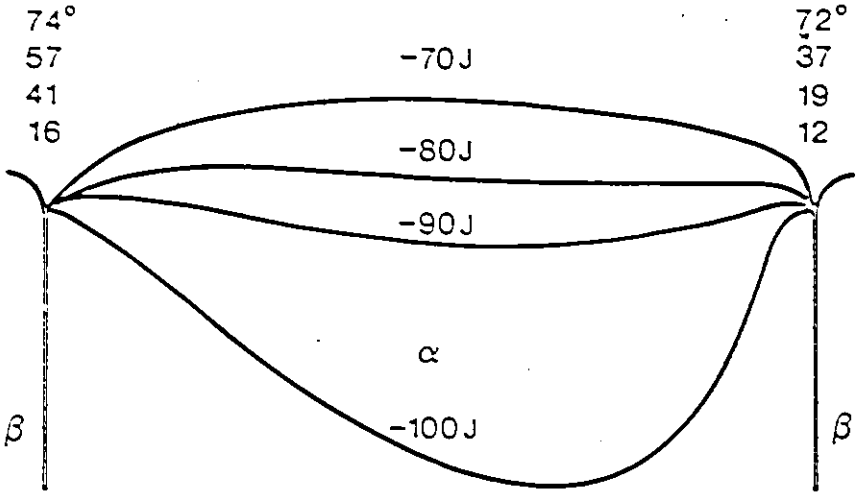

(b)

Figure 5.9 Final calculated interface shape for lamellae C. (a) is the experimentally observed shape and (b) is the calculated shapes. The number associated with each shape indicates the amount of energy removed due to continuous processes. In this particular case, 90 J/mole represents the best fit. (v=4.8 nm/s)

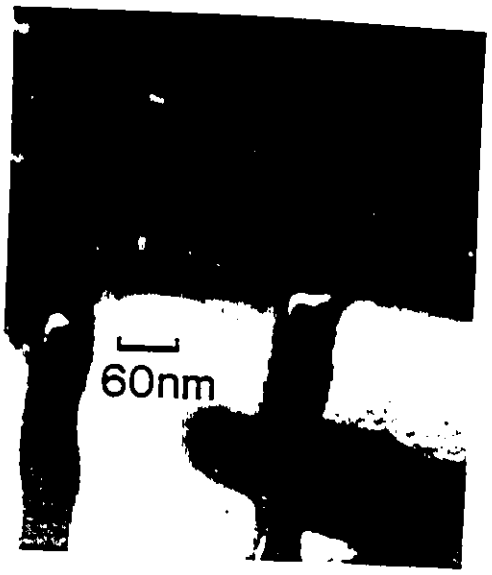

(a)

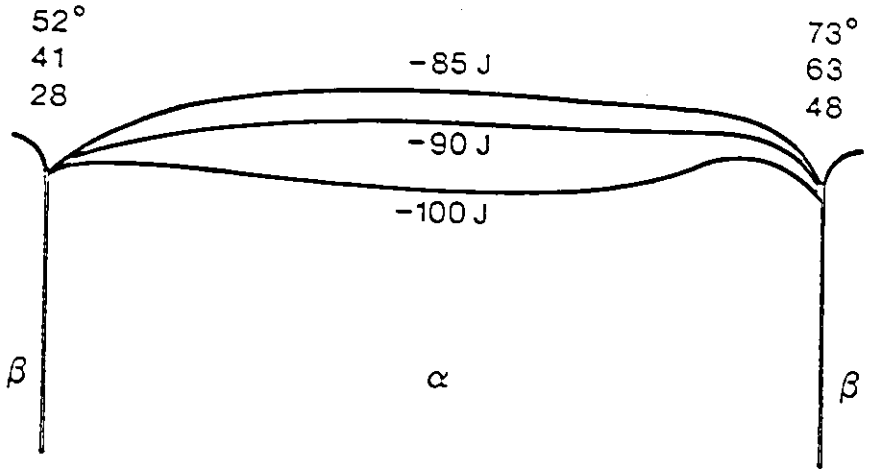

(b)

Figure 5.10 Final calculated interface shape for lamellae D. (a) is the experimentally observed shape and (b) is the calculated shapes. The number associated with each shape indicates the amount of energy removed due to continuous processes. In this particular case, 90 J/mole represents the best fit. (v=4.8 nm/s)

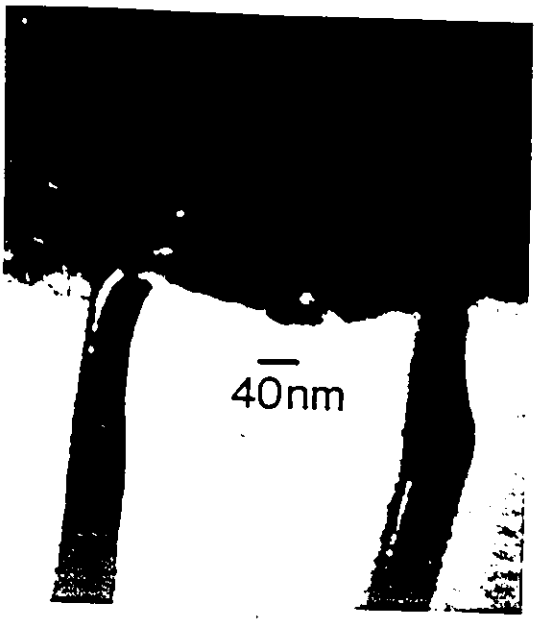

(a)

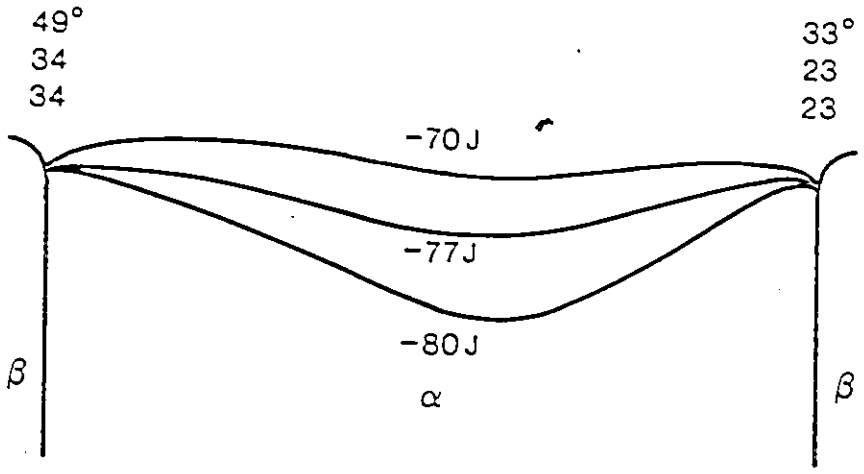

(b)

Figure 5.11 Final calculated interface shape for lamellae E. (a) is the experimentally observed shape and (b) is the calculated shapes. The number associated with each shape indicates the amount of energy removed due to continuous processes. In this particular case, 77 J/mole represents the best fit. (v=9.4 nm/s)

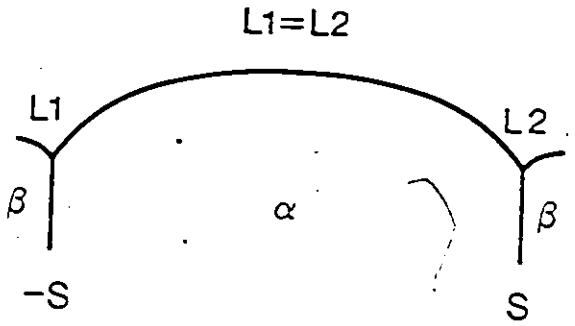

(a)

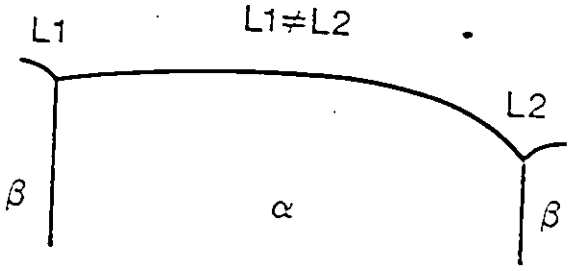

$$\sigma(L1+L2)=\int_{-s}^{s}\Delta G/V_M-\upsilon/M\,dl$$

(b)

Figure 5.12 Surface tension balance at the triple point in a discontinuous product. (a) a cooperative colony in which the balance is equally shared at both ends. (b) a colony which does not share the balance equally.

5.3 Elastic Anisotropy, Initiation and Termination

This section will consider possible mechanisms for the initiation and termination of chemically induced boundary migration. The initiation mechanism developed by D.Yoon et. al. for liquid film migration can be directly applied to the solid state and relies on the penetration of solute from a stationary boundary into the bulk to form the concentration profile as predicted by Fisher (A20) and Whipple (A21). As a result of the concentration gradient, a coherency strain energy results on both sides of the boundary. Since the material is anisotropic, it is assumed that the coherency strain energy is not identical on both sides of the boundary as shown in Figure 5.13. It is possible to calculate the driving force present assuming the orientation given in Figure 5.13 by the equation developed in Appendix D;

$$\Delta G_a = V_m \eta^2 x_d^2 (Y_1 - Y_2)/(1-\nu) \qquad (5.3)$$

using the values of;

$Y1$ <111> = 114 GPa $Y2$ <100> = 99 GPa

$V_m = 10^{-5}$ m^3/mole $\eta = .009$

$x_d = .1$ $\nu = .3$

yields the initiation driving force at 200°C as 0.17 J/mole which after coherency is completely lost in one grain rises to the the value of 1.2 J/mole in the Al-Zn system.

Another possibility which has been suggested (C46) is the grain with the higher amount of coherent strain may lose this strain spontaneously through the nucleation of misfit dislocations. Then, the boundary can progress with the full coherently derived chemical force

acting. Such a process is suggested to be dependent on the thickness of the diffusion profile and therefore would possess a definite incubation time. In the case of CIGM in the Al-Zn system, no dislocations were observed at the original boundary interface which perhaps suggests that the former initiation mechanism is more applicable. Which mechanism operates depends upon the direction of the migrating boundary. If it migrates into the grain with the higher value of Y then the first mechanism operates and if into the lower, the latter mechanism operates.

This mechanism is not limited to the situations where a large amount of solute penetration ahead of the boundary is present. Under conditions where solute penetration is negligible for the moving boundary, the initially stationary boundary can produce a solute field around it, if volume diffusivity is large enough or a sufficient amount of time is allowed. The solute field around the stationary boundary may have a critical size before migration from the prescribed initiation mechanism occurs. In this case, an incubation time may be required before the onset of migration. After initiation, the interface may change from being driven by a low valued chemical force (low force mode) which is derived from coherency strains to a high valued force (high force mode) where a large concentration step exists across the boundary.

Consider another application of the proposed initiation mechanism. It has been stated that a form of CIGM has been observed (B3) as a precursor to discontinuous precipitation in the Al-Zn system. The

initiation of this migration can be easily illustrated in the following manner. At the temperatures used to study discontinuous precipitation, volume diffusion and the formation of zinc rich precipitates are prevalent. Zinc diffuses from the bulk to the boundary and is carried to the precipitates as shown in Figure 5.14. The precipitates are considerably farther apart than the lamellae in the discontinuous product. Concentration gradients are produced in the bulk near the boundary and therefore, a coherency strain energy also. Assuming the first initiation mechanism discussed previously operates, a concentration step is established across the boundary and this produces a driving force for the boundary of the form (Appendix D);

$$\Delta G_a = V_m \eta^2 (x_c - x_o)^2 (\Upsilon_1 - \Upsilon_2)/(1-\nu) \qquad (5.4)$$

where x_o is the original matrix concentration. Measurement of the boundary in the early stages of discontinuous precipitation (83, Fig. 45) yields a velocity of 0.7 to 1.5 nm/s within the first 300 seconds of decomposition at 150°C. This yields a D_v/v value of 1.0 to 2.0 nm. If this initiation mechanism is viable, the boundary has initiated from a low chemical force and has nearly progressed to the high chemical force mode. This is perhaps the only evidence available at this time that a boundary can execute a transition between force modes for the same phase transformation.

It is interesting to examine the migration characteristics of CIGM and discontinuous precipitation in the aluminum zinc system with regard to the penetration parameter D_v/v as shown in Figure 5.15. Two definite branches are present, discontinuous precipitation and CIGM for

both the bulk and surface migration modes. It is interesting to examine the position of the proposed CIGM found in the early processes of discontinuous precipitation. It lies directly between the two main branches which represent the high and low force modes. This may be fortuitous or it may indicate that a transition between the migration modes and forces is possible and perhaps continuous.

The termination of CIGM is a difficult process to envisage. If a boundary is migrating in the high force mode, it may slow down sufficiently as a result of solute source strength depletion or by boundary pinning by defects. The boundary may then make the transition to the low force mode. At this point, migration will cease only if the coherent strain energy difference is lost. This can be accomplished by a number of possible mechanisms. The first mechanism is if the boundary slows down sufficiently to allow the nucleation of misfit dislocations. As stated previously, the diffusion profile width must be great enough to allow the misfit dislocation network to exist. The critical profile width can be estimated by equating the strain energy of a misfit dislocation network with perfect matching between the dislocations to the coherent strain energy. Assuming the diffusion profile behaves similiarly to an epitaxial overgrowth (D5), a steady state diffusion profile and comparable shear moduli for the diffusion profile material and the parent material, the critical velocity can be estimated as:

$$V_c = [2\pi\ (\ln 2)\ D_v\ \eta\ C_c\ (1-2\eta)]/[a\ \ln((2\pi\eta C_c)/(1-\eta)(1+\eta C_c)] \quad (5.5)$$

where Cc is the overgrowth concentration and a is the lattice parameter. Note that this calculated velocity is not a definite limit but simply indicates the energetic limit. The diffusion profile width would be greater in order to nucleate the required dislocation array. Another mechanism relies on the interface interacting with a previously existing dislocation network. The interaction is suggested to relieve the coherency strain in a similiar manner as self nucleated misfit dislocations.

Another mechanism which is accompanied by some experimental evidence indicates that the coherency strain may be relieved by a process which accompanies boundary sliding. As stated in a previous section concerning enhanced migration at a free surface, the coherency strain can be relieved normal to the boundary since it can be considered unconstrained in that direction. This leaves strains parallel to the boundary constrained by both the boundary itself and the matrix ahead of the boundary. If boundary sliding occurs, then lattice dislocations may be nucleated from the boundary which will relieve the coherency strain field ahead of the migrating boundary. Numerous ridges (Figure 4.14 - 4.15) which usually accompany boundary sliding are prevalent within the migration zone on the free surface in typical CIGM experiments in the Al-Zn system. These are suggested to be the result of boundary sliding. The experimental observation of the cessation of migration (Figure 4.21) with the simultaneous formation of one of these ridges substantiates this possible mechanism. The reappearance of migration suggests that total relief of the coherency strain was not achieved or

an initiation process occurred again.

Elastic anisotropy has been utilised to provide a feasible initiation mechanism. Other effects due to elastic anisotropy are possible. Certain growth directions can be preferred under low force modes since the total coherent elastic strain energy can be greater. Less obvious effects are the effects of an externally applied stress upon discontinuous precipitation in the Cu-Cd system as studied by Sulonen (59) and CIGM in the Fe-Zn system (62). In each case, the direction of migration or precipitation has been modified. It is suggested that elastic anisotropy is responsible for these effects. However, such an effect has not been observed in the Al-Zn system in this investigation since this system possesses minimal anisotropy. Whether the effect of anisotropy is dominant in the initiation process or during the growth process or how an external stress and anisotropy interact to modify migration is unknown at this time.

This section has shown that a coherency derived chemical driving force is consistent with the processes of initiation and cessation. The prediction of the coexistence of boundary sliding and cessation of migration by the coherency strain model strengthens the validity of the model.

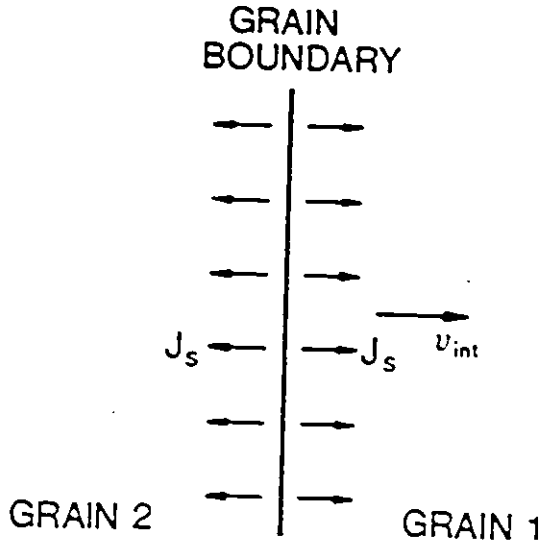

(a)

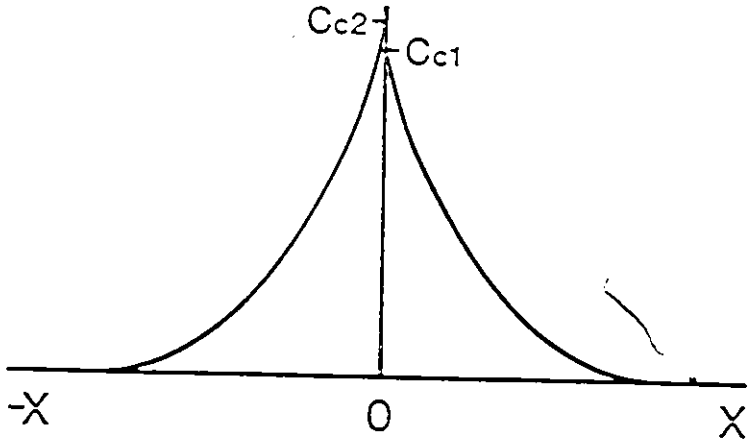

(b)

Figure 5.13 Diagram illustrating the effects of elastic anisotropy. The difference in the coherency strain energy on either side of a boundary produces a concentration step across the boundary (a). The strain energy difference then can produce a driving force across the grain boundary (b)

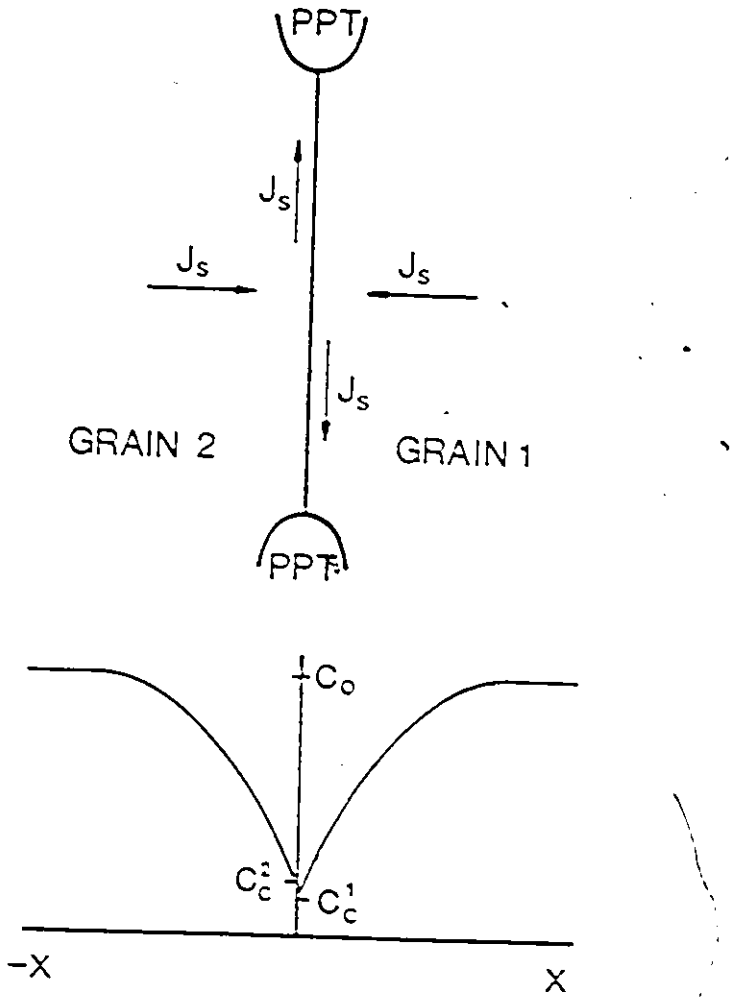

Figure 5.14 Diffusion of zinc during the initial stages of discontinuous precipitation. Precipitate spacing is considerably (83) larger than in the discontinuous product. The bulk is depleted of solute near the boundary producing coherency strains and perhaps a concentration difference across the boundary if the elastic anisotropy is sufficently large.

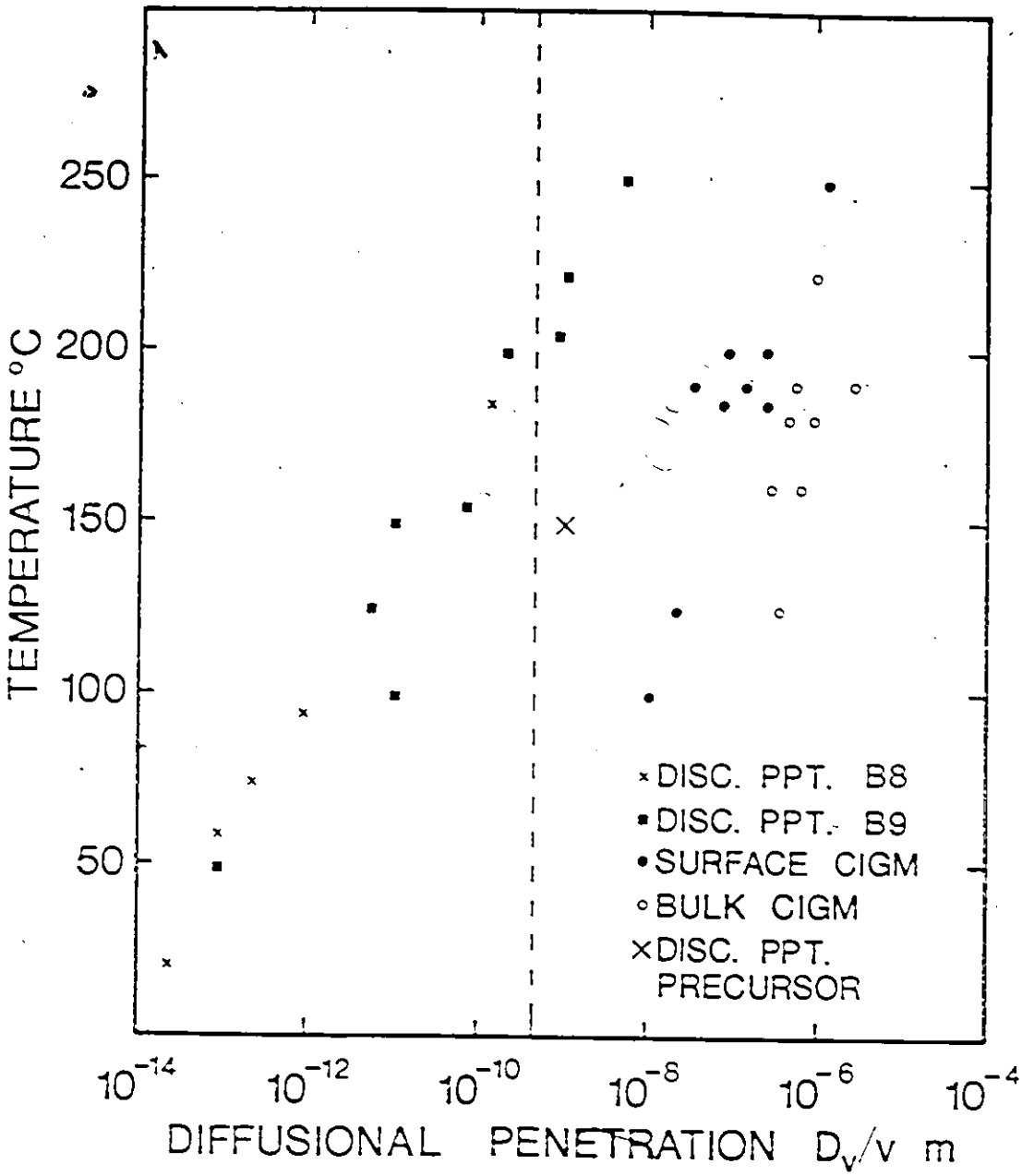

Figure 5.15 Comparison of solute penetration depths for discontinuous precipitation and alloying CIGM in the aluminum zinc system. Note the position of the dealloying CIGM which is found prior to full discontinuous precipitation.

5.4 Chemical Driving Forces and Grain Boundary Structure

Grain boundary structure has not been considered extensively in the overall model of boundary migration driven by a chemical force. The difficulty arises because there is no firm method of establishing the effect of a chemical driving force upon the structural components of a grain boundary which are suggested to be responsible for migration. Since the climb of ledges and step components of grain boundary dislocations result in migration, it seems logical to assign a chemical potential difference across them as suggested by Li (C27). However, the application of such a macroscopic force upon an atomistic structural component is fundamentally questionable. Assuming pure steps are not solely responsible for migration, another difficulty with the model lies in the difficulty in the selection of the dislocations with the Burgers vectors appropriate for climb.

Since the selection of individual dislocations whose movement results in migration only is unlikely, movement of groups of dislocations whose collective glide component is minimised is more viable. The proposed process assumes that the boundary structure is conserved during migration. There is little evidence to support this presumption and indeed, the experimental evidence (such as higher boundary diffusion rates during migration) tends not to support this. If the boundary structure is not conserved then the role of grain boundary dislocations and steps in migration must be reevaluated.

5.5 Computer Simulations of Chemically Driven Boundary Migration

The purpose of the computer simulation presented in this discussion is to model the migration of a grain boundary which is chemically driven. The model is based on the following assumptions:

(1) The boundary is driven by a coherency strain derived chemical force obtained using ideal solution behaviour.

(2) The boundary velocity follows a linear velocity force relationship.

(3) Capillarity is accounted for in this model but as a secondary effect. All the chemical force is not balanced by capillarity but is reduced by it when boundary curvature becomes excessive.

(4) A proportionality relationship exists between the boundary and alloyed grain concentrations.

(5) The trailing edge of the boundary is assumed to be in equilibrium with the growing grain.

(6) The shrinking grain concentration is coherency strain compensated.

(7) Volume diffusion (in two dimensions) is allowed in the growing grain.

(8) Finite difference calculations are performed with a moving reference frame attached to the boundary.

(9) Mobility is estimated from the measured velocity and the estimated coherency derived chemical force.

(10) Migration is assumed to be established early during the diffusion period.

A full description of the derived partial differential equations and program listing is given in Appendix F. The results of the

simulation are shown in Figures 5.16 to 5.17 for the temperature of 130°C. The results indicate that a near steady state is established early within the migration process. The effective depth of penetration calculated by the simulation compares favourably with the measured depth, even though it is a near steady state answer. The final boundary displacement calculated are greater at the surface than those observed experimentally suggesting the surface conditions assumed are too simple for the actual situation.

In situ migration observations as well as comparisons of simulation results and penetration depth measurements suggest that steady state migration can be achieved for a semi-infinite sample early during migration. The steady state solution to the diffusion problem is given in Appendix F and produces equations which relate concentration profiles $C_d(y)$, velocity profiles $v(y)$ and the penetration depth $Y(.01)$ (the depth where the concentration is 1% of the maximum surface concentration) as;

$$C_d(y) = [\ A/2\ y + 1/C_e]^{-1} \tag{5.6}$$

$$v = \frac{M\ E\ V_m\ \eta^2}{1-\nu}\left[\left(\frac{M\ E\ V_m\ \eta^2}{K\ D_b\delta\ (1-\nu)}\right)y^2 + \frac{1}{C_e}\right]^{-2} \tag{5.7}$$

$$Y(0.01) = \frac{99\sqrt{2}\ E\ M\ V_m\ \eta^2}{C_e\ (1-\nu)\ K\ D_b\delta} \tag{5.8}$$

The penetration depth relationship due to its simplicity can yield information concerning the cross and parallel grain boundary diffusivities. Assume that the velocity is simply related to the cross boundary diffusivity $D_\perp$ by;

$$M \simeq D_{\perp} / RT \tag{5.9}$$

and the cross diffusivity $D_{\perp}$, parallel diffusivity $D_{\parallel}$ and the equilibrium concentration C_e can be represented by the appropriate Arrhenius relationship;

$$D_{\perp} = D_{\perp}^{\circ} \exp(-Q_{\perp}/RT) \tag{5.10}$$

$$D_{\parallel} = D_{\parallel}^{\circ} \exp(-Q_{\parallel}/RT) \tag{5.11}$$

$$C_e = C_o \exp(-Q_e/RT) \tag{5.12}$$

Then the temperature dependence should follow the following relationship;

$$f(T) = (1/T) \exp((Q_{\parallel} + Q_e - Q_{\perp})/RT) \tag{5.13}$$

If cross and parallel diffusion processes are similar then their respective activation energies will also be similar. Then the penetration depth Y(.01) will possess an $(\exp(Q_e/RT)/T)$ temperature behaviour. The temperature dependence described by this expression does not agree with the observed decrease in penetration depth. This indicates that the respective activation energies for diffusion parallel and normal (cross) to the boundary plane may not be equal. For the penetration depth to decrease at a greater rate as the temperature rises, then the cross diffusivity term must have a greater activation energy than the parallel term. This is an indication that perhaps the diffusion mechanisms differ depending upon the diffusion direction.

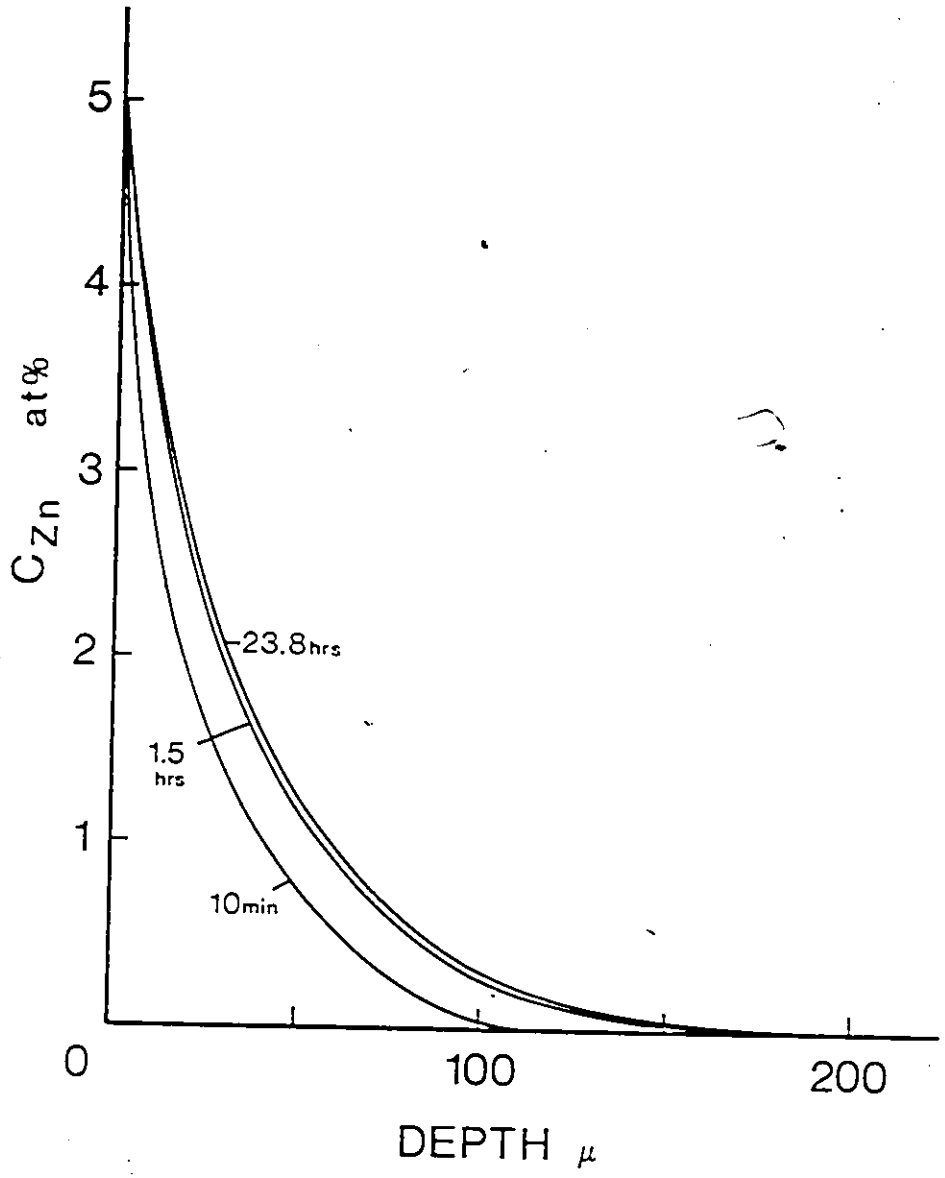

Figure 5.16 Boundary concentration profiles calculated for various times for migration at 130°C assuming a coherency strain derived chemical driving force.

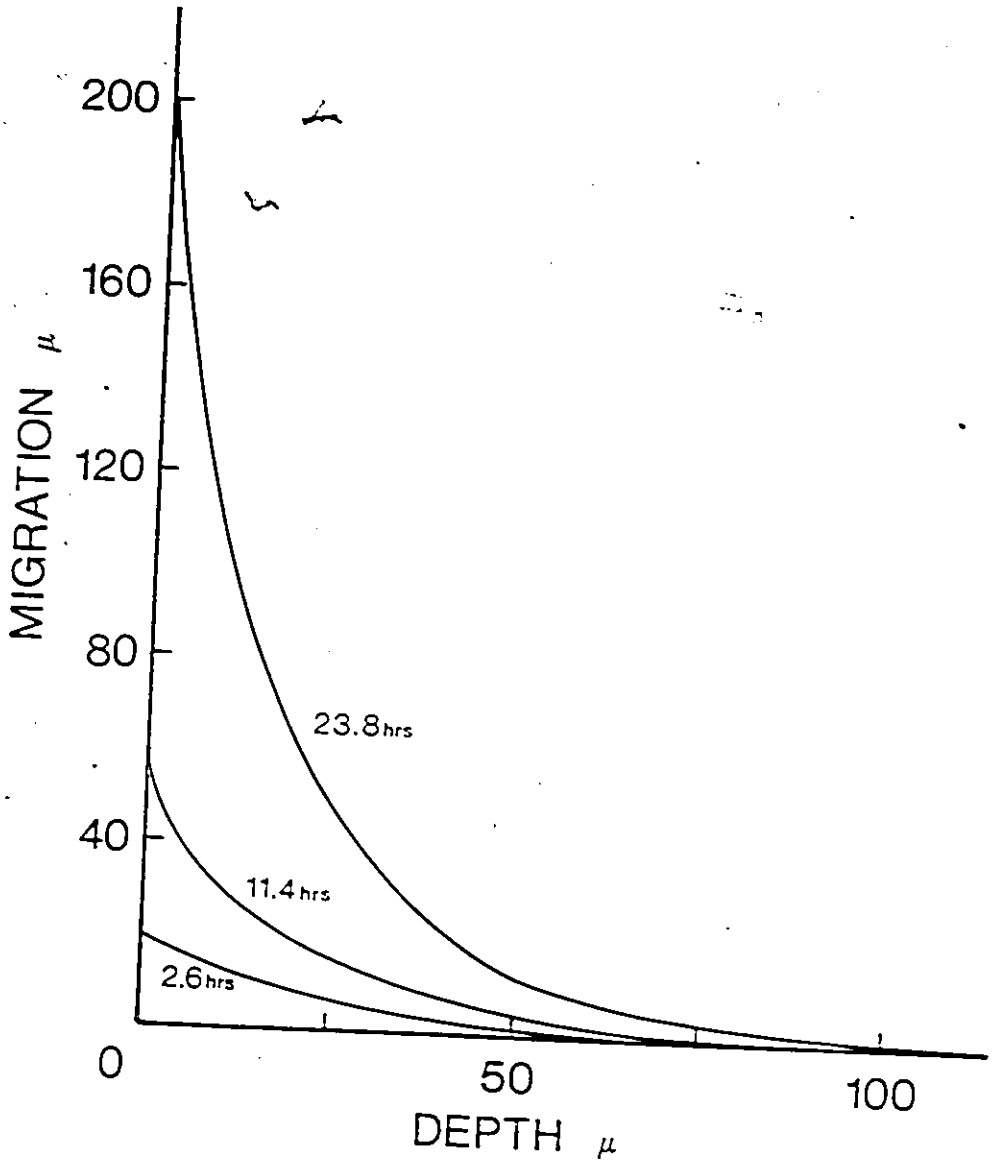

Figure 5.17 Boundary displacement profiles calculated for various times for migration at 130°C assuming a coherency strain derived chemical driving force.

CHAPTER 6

FURTHER WORK

(a) Elastic Anisotropy

In order to test the premise that elastic anisotropy is responsible for migration initiation, a series of experiments which control anisotropy would be necessary. Such an experiment would involve the use of small single crystal balls sintered onto a base single crystal of known orientation (D3, D4). The solute would be introduced by means of a vapour source. The resulting migration should indicate preferred migration orientations which should reflect large anisotropic conditions.

(b) Pure Entropic Driving Forces

This type of driving force for a boundary has been very controversial for many years. This is a chemical driving force in its purest sense. Since misfit does not exist in this system, then the chemical forces which are derived from the coherent strain energy do not exist. Therefore, under the premises already considered, low force CIGM should not exist and initiation would be impossible. It is also necessary to ensure that any other possible driving force be excluded from the experiment. An experiment is possible which isolates entropic driving forces and initiates boundary migration. A single crystal shaped similiar to a funnel is coated with the isotope. Boundary migration is initiated by capillarity forces at the widest portion of the sample. If

migration ceases at the neck where the specimen edges are parallel then entropic forces are not present, however, if migration continues into the straight portion, then these forces may be present.

(c) CIGM in a Ternary System

An experiment of this nature will elucidate the equilibrium conditions at the interface. The second solute is uniformly distributed in the system and the first solute will be diffused into the system at temperatures in which the coherency force may dominate. Varying the second solute concentration will vary the misfit which will experimentally test the validity of a coherency strain derived chemical force in a solid. This effect relies on the second solute redistributing to allow the misfit reduction.

(d) Molecular Dynamics Study

A large scale molecular dynamics study is necessary to determine the role of grain boundary dislocations and steps in grain boundary migration. The question of boundary structure conservation during migration should also be addressed.

CHAPTER 7

CONCLUSIONS

The work represented here has attempted to resolve the validity of a chemical driving force upon a grain boundary. Whereas the work is far from being complete, there are a number of conclusions that may be stated:

(1) The motion of grain boundaries can be driven by a chemical force which is derived from a concentration difference which exists across the boundary.

(2) The magnitude of this force will vary depending upon the velocity of the interface and the extent of volume diffusion penetration which precedes the boundary.

(3) The chemical force is physically limited to two extremes: the high force limit in which the full compositional difference exists across the boundary and the lower limit in which the compositional difference is nearly fully relaxed and placed into a state of constrained equilibrium. It can be shown that this low magnitude force can find its origin in the coherency strain energy in the coherent layer in front of a slow moving, high penetration interface.

(5) A transition between the two extreme chemical force states is

possible for the same boundary but it has not been determined explictly in this investigation whether the transition between the extremes is continuous.

(6) It has been demonstrated that under such a driving force, the initiation, kinetics and cessation of migration can be modelled successfully.

(7) The initiation event is suggested to be a result of anisotropic elastic energy due to volume diffusion from the boundary on either side which produces a concentration gradient across the boundary but unequal strain energies.

(8) The overall kinetics of migration have been modelled assuming a coherency derived chemical driving force. By using such a model, the general characteristics of migration have been simulated and unusual migration behaviour (ie. enhanced migration at free surfaces) has been qualitatively explained using such a model.

(9) The cessation of migration is suggested to be derived from the loss of the coherent strain energy ahead of the migrating boundary and is believed to the due to the nucleation of lattice misfit dislocations.

The principles just described can be applied to a large variety of interfacial reactions. This particular study focussed upon a chemical driving force in its purest form as CIGM and discontinuous precipitation which is complicated by the presence of growing precipitates. The usefulness of employing a chemical force was demonstrated when interfacial shapes were successfully derived from lamellae microchemistry and therefore, from the chemical energy available.

The macroscopic nature of the chemical force makes it useful in

describing a large range of transformations. Unfortunately, the importance of boundary structure in coupling the chemical force to boundary structure components is not explict. It is suggested that the present model of boundary structure components is insufficient to fully resolve the problem of coupling a macroscopic force to atomistic components under the assumption that boundary structure is conserved during migration.

REFERENCES

GRAIN BOUNDARY STRUCTURE, DIFFUSION AND MIGRATION

A1. A.P. Sutton, Int. Metals Rev. 29 (1984) 377.

A2. R.W. Balluffi, "Interfacial Segregation", ASM, Ohio, (1977) 193.

A3. "Grain Boundary Structure and Kinetics", ASM, Ohio, (1979).

A4. R.C. Pond, in ref. A3, (1979) 13.

A5. R. Gronsky, in ref. A3, (1979) 45.

A6. S.L. Sass and P.D. Bristowe, in ref. A3, (1979) 71.

A7. V. Vitek, A.P. Sutton, D.A. Smith and R.C. Pond, in ref. A3, (1979) 115.

A8. H.J. Frost, M.F. Ashby and F. Spaepan, in ref. A3, (1979) 149.

A9. P.J. Goodhew, in ref. A3, (1979) 155.

A10. N.L. Peterson, in ref. A3, (1979) 209.

A11. R.W. Balluffi, in ref. A3, (1979) 297.

A12. D.A. Smith, C.M.F. Rae and C.R.M. Grovenor, in ref. A3, (1979) 337.

A13. P. Lamarre, F. Schmuckle, K. Sickafus and S.L. Sass, Ultramicroscopy 14 (1984) 11.

A14. J.C. Fisher, J. Appl. Phys. 22, (1951) 74.

A15. R.W. Balluffi, Metal. Trans. A 13A (1982) 2069.

A16. G. Martin and B. Peraillon, in ref. A3, (1979) 239.

A17. T. Kwok, P.S. Ho and S. Yip, Phys. Rev. 29 (1984) 5353.

A18. T. Kwok, P.S. Ho and S. Yip, Phys. Rev. 29 (1984) 5363.

A19. T. Kwok, P.S. Ho, S. Yip, R.W. Balluffi, P.D. Bristowe and A. Brokman, Phys. Rev. Let. 47 (1981) 1148.

A20. D. Turnbull, Scr. Trans. AIME 191 (1951) 661.

A21. R.T.P. Whipple, Phil. Mag. 45 (1954) 1225.

A22. K. Shimoda, W. Gottschalk and H. Gleiter, Acta Met. 26 (1978) 1833.

A23. R.C. Pond, "Dislocation Modelling of Physical Systems", Pergamon Press, (1980) 524.

A24. K. Lucke and H.P. Stuwe, Acta Met. 19 (1971) 1087.

A25. M. Hillert and B. Sundman, Acta Met. 24 (1976) 731.

A26. K. Lucke, R. Rixen and F.W. Rosenbaum, "The Nature and Behaviour of Grain Boundaries", Plenum Press, (1972) 245.

A27. J.W. Cahn, Acta Met. 10 (1962) 789.

A28. K. Lucke and G. Gottstein, Acta Met. 29 (1981) 779.

A29. D.A. Porter and K.E. Easterling, "Phase Transformations in Metals and Alloys", Van Nostrand Reinhold, (1980)

A30. M.J. Weins, Phil. Mag. 31 (1972) 138.

A31. V. Vitek, D.A. Smith and R.C. Pond, Phil. Mag. 41 (1980) 649.

A32. M.F. Ashby, F. Spaepan and S. Williams, Acta Met. 26 (1978) 1647.

A33. R. Chang, Scr. Met. 14 (1980) 779.

A34. D.A. Smith, V. Vitek and R.C. Pond, Acta Met. 25 (1977) 475.

A35. D.A. Smith, A.P. Sutton, V. Vitek and R.C. Pond, Phil. Mag. 39 (1979) 213.

A36. R.M.J. Cotterill, T. Leffers and H. Lilholt, Phil. Mag. 30 (1974) 265.

A37. W. Hahn and H. Gleiter, Acta Met. 29 (1981) 601.

A38. P.H. Pumphrey and H. Gleiter, Phil. Mag. 31 (1975) 881.

A39. A.P. Sutton and V. Vitek, Scr. Met. 14 (1980) 563.

A40. C.J. Simpson and K.T. Aust, Surf. Sci. 31 (1972) 479.

A41. W. Bollman, "Crystal Defects and Crystalline Interfaces", Springer Verlag, New York, (1970)

A42. M.F. Ashby, Surf. Sci. 31 (1972) 498.

A43. M.S. Sulonen, Acta. Met. 12 (1964) 749.

ENERGETICS IN PHASE TRANSFORMATIONS

B1. M. Hillert, "The Mechanism of Phase Transformations in Crystalline Solids", The Institute of Metals, London, (1969) 231.

B2. M. Hillert, Metal. Trans. B 3 (1972) 2729.

B3. I.G. Solorzano-Naranjo, Ph.D. Thesis, McMaster University, (1983)

B4. J. Cahn, Acta Met. 9 (1961) 795.

B5. G.R. Purdy, "Solid-Solid Phase Transformations", H.I. Aaronson ed., Metal. Soc. AIME, (1981) 521.

B6. A. Perovic, Ph.D. Thesis, McMaster University, (1983)

B7. B.E. Sunquist, Metal. Trans. B 4 (1973) 1919.

B8. C.P. Ju and R.A. Fournelle, Acta Met. 33 (1985) 71.

B9. W. Gust, M.B. Hintz, R. Lucic and B. Predel, Met. Res. Soc. Symp. Proc. 21 (1984) 513.

B10. K.B. Rundman and J.E. Hilliard, Acta Met. 15 (1967) 1025.

B11. K.K. Rao, L.E. Katz and H. Herman, Mat. Sci. Eng. 1 (1966) 263.

B12. N. Lange and G.R. Purdy, "Decomposition of Alloys; the early stages", Pergamon Press, (1983) 214.

B13. E.C. Ellwood, J. Inst. Phys. 80 (1951) 217.

CHEMICALLY (DIFFUSION) INDUCED GRAIN BOUNDARY MIGRATION

C1. M. Hillert and G.R. Purdy, Acta Met. 26 (1977) 333.

C2. Li Chongmo and M. Hillert, Acta Met. 29 (1981) 1949.

C3. P.G. Shewmon, Acta Met. 29 (1981) 1567.

C4. Zong-sen Yu and P.G. Shewmon, Met. Trans. A 13A (1981) 1567.

C5. D.B. Butrymowicz, T.J. Picone, J.R. Manning and D.E. Newbury, Metallography 16 (1983) 349.

C6. Y.S. Tsai, G. Meyrick and P.G. Shewmon, Metal. Trans. A 15A (1984) 495.

C7. J.D. Pan and R.W. Balluffi, Acta Met. 30 (1982) 861.

C8. C.R.M. Grovenor, Acta Met. 33 (1985) 579.

C9. F.J.A. den Broeder and S. Nakahara, Scr. Met. 17 (1983) 399.

C10. D.B. Butrymowicz, T.J. Picone, J.R. Manning, D.E. Newbury and J.W. Cahn, Scr. Met. 16 (1982) 839.

C11. C.R.M. Grovenor, Scr. Met. 16 (1982) 317.

C12. J.M. Vandenberg, F.J.A. den Broeder and R.A. Hamm, Thin Solid Films 93 (1982) 277.

C13. F.J.A. den Broeder and S. Nakahara, Scr. Met. 17 (1983) 607.

C14. S. Nakahara, J.A. Abys and S.M. Abys, Materials Let. 2 (1983) 155.

C15. E.J. Mittemeijer and A.M. Beers, Thin Solid Films 65 (1980) 125.

C16. M. Klerk, J.M. Vandenberg, F.J.A. den Broeder and R.A. Hamm, Acta Met. 31 (1983) 285.

C17. Li Chongmo, Metallography 16 (1983) 59.

C18. D.B. Butrymowicz, D.E. Newbury, D. Turnbull and J.W. Cahn, Scr. Met. 18 (1984) 1005.

C19. F.J.A. den Broeder, Acta Met. 20 (1972) 319.

C20. K.N. Tu; J. Appl. Phys. 48 (1977) 3400.

C21. F.N. Rhines and A.M. Montgomery, Nature (March 1938) 413.

C22. Li Chongmo, Scand. J. Metal. 11 (1982) 179.

C23. J.W. Cahn J.D. Pan and R.W. Balluffi, Scr. Met. 13 (1979) 503.

C24. M. Hofmann-Amtenbrink, W.A. Kaysser and G. Petzow, Z. Metallkd. 5 (1981) 305.

C25. T.A. Parthasarathy and P.G. Shewmon, Scr. Met. 17 (1983) 943.

C26. T.A. Parthasarathy and P.G. Shewmon, Acta Met. 32 (1984) 29.

C27. J.C.M. Li and B.B. Rath, Scr. Met. 19 (1985) 689.

C28. W. Kim, G. Meyrick and P.G. Shewmon, Scr. Met. 17 (1983) 1435.

C29. R.W. Balluffi and J.W. Cahn, Acta Met. 29 (1981) 493.

C30. D.A. Smith and A.H. King, Phil. Mag. 44 (1981) 333.

C31. A.H. King, Phil. Mag. 48 (1983) L39.

C32. A.H. King, Scr. Met. 15 (1981) 1221.

C33. P.G. Shewmon, G. Meyrick, S. Mishra and T.A. Parthasarathy, Scr. Met. 17 (1983) 1231.

C34. V.K. Garke and A.H. King, Scr. Met. 18 (1984) 1341.

C35. M. Hillert and Li Chongmo, Scand. J. Metal. 10 (1981) 171.

C36. J.E. Blendell, C.A. Handwerker, W.A. Yaysser and G. Petzow, "Surface and Interfaces in Ceramic and Ceramic-Metal Systems", Mat. Sci. Res. V14, Plenum Press, (1981) 217.

C37. K. Tashiro and G.R. Purdy, Scr. Met. 17 (1983) 455.

C38. K. Tashiro and G.R. Purdy, "Interface Migration and Control of Microstructures", ASM, (1985) 47.

C39. C.A. Handwerker, R.L. Coble and J.E. Blendell, "Character of Grain Boundaries", Advances in Ceramics, Amer. Ceram. Soc., Ohio, (1982) 213.

C40. D.N. Yoon and W.J. Huppmann, Acta Met. 27 (1979) 973.

C41. Y. Song and D.N. Yoon, Metal. Trans. A 15A (1984) 1503.

C42. E.P. Butler and A.H. Heuer, J. Am. Ceram. Soc. 68 (1985) 197.

C43. Li Chongmo and M. Hillert, Acta Met. 30 (1982) 1133.

C44. M. Hillert, Scr. Met. 17 (1983) 237.

C45. V.S. Iyer, G. Meyrick and P.G. Shewmon, Scr. Met.19 (1985) 1117.

C46. C. Handwerker, D.N. Yoon, J.E. Blendell, Y.J. Baik and J.W. Cahn, "Interface Migration and Control of Microstructure", ASM, (1985)

C47. Y. Song, S. Ahn and D.N. Yoon, Acta Met. 33 (1985) 1907.

C48. J.D. Pan, Ph.D. Thesis, Cornell University, (1980)

GENERAL

D1. G. Herrmann, H. Gleiter and G. Baro, Acta. Met. 24 (1976) 353.

D2. H. Sautter, H. Gleiter and G. Baro, Acta. Met. 25, (1977) 467.

D3. U. Valdre, J. Sci. Instrum. 42 (1965) 853.

D4. G. Petzow, "Metallographic Etching", ASM, Ohio, (1976)

D5. W.A. Jesser, D. Kuhlmann-Wilsdorf, Phys. Stat. Sol. 19 (1967) 95.

D6. R. Hultgren, R.L. Orr, P.D. Anderson and K.K. Kelly, "Selected Values of Thermodynamic Properties of Binary Alloys", ASM, (1973)

APPENDIX A

PLATING BATH COMPOSITIONS AND CONDITIONS

METAL	COMPONENTS	CONCENTRATION	NOTES
Cu	$CuSO_4$-$5H_2O$	250 g/l	Cu Anode 20 - 30°C
	H_2SO_4	30 ml/l	20 - 100 mA/sq cm
Mn	$MnSO_4$	120 g/l	Stainless Steel Anode
	$(NH_4)_2SO_4$	80 g/l	20 - 30°C
	NH_4CNS	60 g/l	240 mA/sq cm
Ni	$NiSO_4$-$6H_2O$	300 g/l	Ni Anode
	$NiCl_2$-$6H_2O$	45 g/l	30 - 40°C
	H_3BO_4	30 g/l	10 - 60 mA/sq cm
	H_2O_2	5 ml/l	
Pd	$Pd(NH_4)_4(NO_3)_2$	100 g/l	Stainless Steel Anode
			30°C 100 mA/sq cm
Zn	$ZnSO_4$-$7H_2O$	350 g/l	Zinc Anode 40 - 55°C
	$(NH_4)_2SO_4$	30 g/l	100 - 600 mA/sq cm
Zn Strike	NaOH	400 g/l	
	ZnO	100 g/l	

APPENDIX B

ETCHING COMPOSITIONS

SAMPLE	COMPONENTS	CONCENTRATION	NOTES
Ag - Cu Ag - Pd Ag - Mn	NH_4OH H_2O_2 (30%)	50 ml 50 ml	Swab Surface
Al - Zn	NaOH NaF	20 g/l 50 g/l	Immerse for 1-2 min
Au - Ni	HNO_3(1.4)	40 ml	
Au - Pd	HCl (1.19)	60 ml	
Cu - Pd	NH_4OH	25 ml	Swab Surface
Cu - Mn	H_2O H_2O_2 (30%)	25 ml 25 ml	
Pt - Pd	HCl (1.19)	-	Electrolytic Pt Cathode 1-5 VAC

APPENDIX C

HB5 STEM HOT STAGE DESIGN DETAILS

The following details the considerations necessary in order to construct a top loading heating stage. All components which are subjected to elevated temperatures are constructed of AISI 303 stainless steel. This alloy was chosen for its non-magnetic properties and is oxidation resistance. It is not however, the ideal material for X-ray analysis due to the spurious spectral lines which can arise. All sliding components are lubricated with molybdenum disulphide except the pivot screws. The power and thermocouple wires were insulated with fused silica capillary tubing nearest the heater and with teflon tubing where the temperature was lower.

The contact block assemblies were machined from ceramic with the contacts bonded with high vacuum epoxy. The ceramic block is held to the main body with fast setting ceramic adhesives.

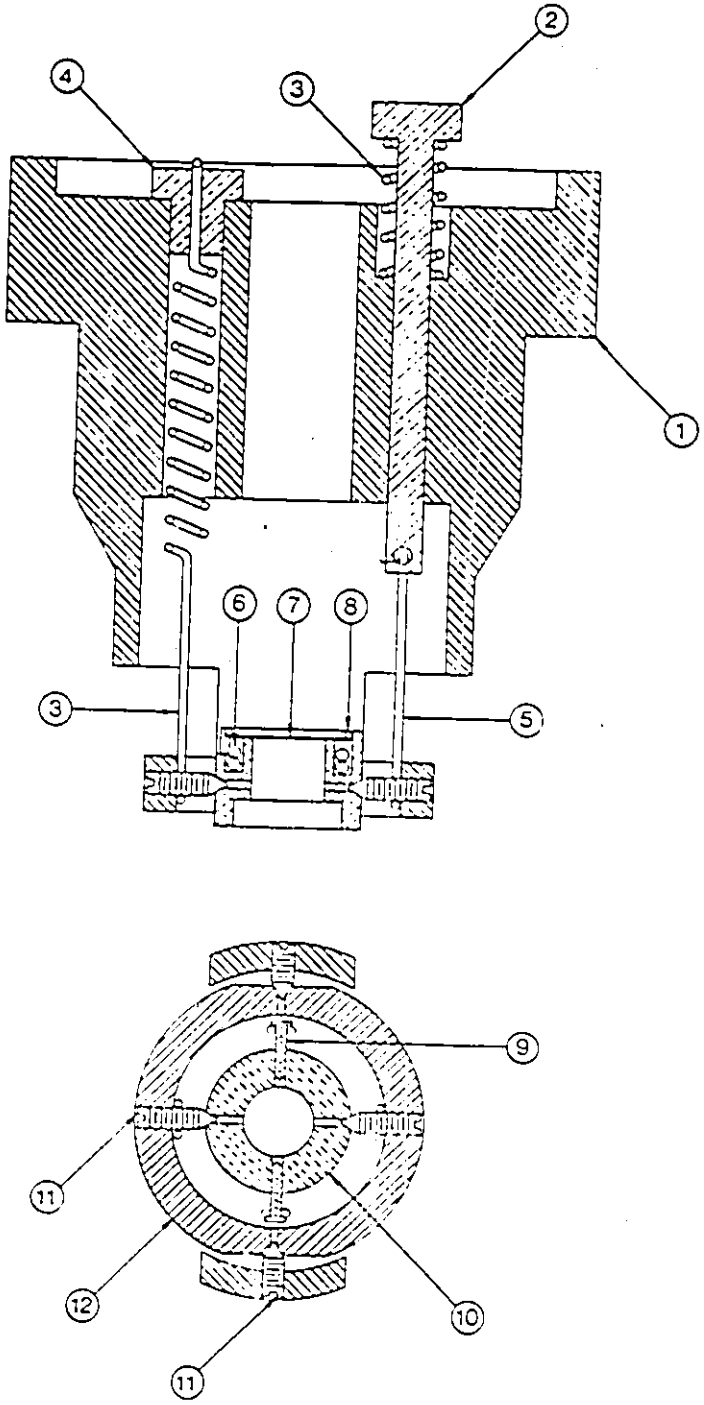

Figure C.1 Assembly Drawing of the Hot Stage Nose Piece

1. Main Support
2. Push Rod
3. Spring
4. Support Block
5. Wire
6. Heater
7. Cover Ring
8. Clip
9. Screw
10. Sample Ring
11. Pivot Screws
12. Gimbal Ring

Appendix D

Calculation of the Chemical Potential Difference Across a Boundary due to Retained Coherency Strain and Elastic Anisotropy

Consider two alpha grains possessing individual coherent strain energy terms due to elastic anisotropy;

$$G_a^1 = (1-x_1)G_a^\circ + x_1 G_b^\circ + RT\,[(1-x_1)\ln(1-x_1) + x_1 \ln x_1] + \gamma_1 x_1^2 \qquad (D1)$$

$$G_a^2 = (1-x_2)G_a^\circ + x_2 G_b^\circ + RT\,[(1-x_2)\ln(1-x_2) + x_2 \ln x_2] + \gamma_2 x_2^2 \qquad (D2)$$

where γ_1, γ_2 are elasticity terms. Equating the chemical potentials for B atoms yields;

$$RT \ln(x_1/x_2) = 2(\gamma_2 x_2 - \gamma_1 x_1) \qquad (D3)$$

if γ_1, γ_2 are small then $x_1 \sim x_2 \sim x_D$ then;

$$RT \ln(x_1/x_2) = 2x_D\,(\gamma_1-\gamma_2) \qquad (D4)$$

$$(x_1/x_2) = 1 - 2x_d\,(\gamma_1-\gamma_2)\,/RT \qquad (D5)$$

The chemical potential difference in A describes the driving force acting at the boundary. Again if $x_1, x_2 \sim x_D$ then;

$$G_a = x_d^2\,(\gamma_1-\gamma_2) \qquad (D6)$$

Nominally, γ is defined as;

$$\gamma = E\,V_m\,\eta^2\,/(1-\nu) \qquad (D7)$$

if anisotropy effects are prevalent then;

$$\Delta G_a = V_m\,\eta^2\,x_d^2\,(E_1-E_2)/(1-\nu) \qquad (D8)$$

This relationship describes the chemical driving forces which are useful

for initiation. Another situation which may occur is when the relaxation occurs asymmetrically. This situation occurs if the daughter alloyed grain retains a portion of the coherency strain energy from the parent grain. If the elastic moduli are equal, then the strain energy in the daughter grain γ_1 is related to the parent grain strain energy γ_2 by:

$$\gamma_1 = \gamma_2 \, f(x) \tag{D9}$$

where, $f(x)$ represents the position dependent retained coherent strain energy fraction. The driving force under these conditions then becomes;

$$\Delta G_a = V_m \, \eta^2 \, x_d^2 \, E \, (1-f(x))/(1-\nu) \tag{D10}$$

Appendix E

Chemical Energy Loss due to Spinodal Decomposition

Three energy terms must be considered in order to estimate the total energy loss due to spinodal decomposition;

(1) Chemical energy loss due to decomposition only. (ΔG_c)

(2) Coherency strain energy (E_c)

(3) Compositional gradient energy (E_g)

The chemical energy term is determined graphically from the free energy diagram and is estimated to be 227±10 J/mole. The next two terms rely on the concentration profile which exists in the decomposed alloy and are defined as;

$$E_c = V_m \int \eta^2 Y (C - C_o)\, dv \qquad \text{(E1)}$$

$$E_g = V_m \int K (\nabla C)^2\, dv \qquad \text{(E2)}$$

where $Y = E/(1-\nu)$. Parameter values are taken from Rundman and Hilliard (B10) and are;

$V_m = 10^{-5} m^3/mole$ $\qquad$ $K = 16 \pm 3 \times 10^{-11}$ J/mole

$\eta = 0.027$ $\qquad$ $Y = 1.22 \pm .2 \times 10^{11}$ J/m

Assuming that decomposition has progressed sufficiently, the concentration profile is assumed to possess the form as shown in Figure E1. Assuming that there are no long range fluctuations, then;

$$\int (C_o - C)\, dv = 0 \qquad \text{(E3)}$$

Using the one dimensional form and a pure square wave profile, then the following relationship concerning the profile is assumed;

$$(\int C_1\, dx + \int C_2\, dx)/(L_1 + L_2) = C_o \qquad \text{(E4)}$$

Asssuming $C_1 = 0.02$ and $C_2 = 0.62$ (coherent chemical equilibrium points) then $L_1 = .651$ and $L_2 = .351$ for $C_o = 0.22$.

With the profile parameters defined, the evaluation of the energy terms is now possible. The energy terms now become;

$$\begin{aligned} E_c &= V_m\, \eta^2\, Y \int (C - C_o)^2\, dv \\ &= V_m\, \eta^2\, Y\, [\int (0.62-0.22)^2 dx + \int (0.02-0.22)^2\, dx]/\lambda \\ &= 0.082\, V_m\, \eta^2\, Y \\ &= 73 \pm 10 \text{ J/mole} \end{aligned} \qquad \text{(E5)}$$

For the gradient energy term;

$$\begin{aligned} E_g &= V_m\, K \int (\nabla C)^2\, dv \qquad \Rightarrow \qquad \nabla C = dC/dX = \Delta C/\delta \\ &= V_m\, K\, [2 \int (\Delta C/\delta)^2\, dx]/\lambda \\ &= V_m\, K\, (\Delta C/\delta)^2\, 2\delta/\lambda \\ &= 2\, V_m\, K\, \Delta C^2/\lambda\delta \end{aligned} \qquad \text{(E6)}$$

(E7)

Estimating λ as 20 nm from the micrographs and assuming δ as 1 nm, then $E_g = 57 \pm 5$ J/mole. The total energy loss is then;

$$\begin{aligned} E_t &= G_c - E_c - E_g \\ &= (227 \pm 10) - (73 \pm 10) - (57 \pm 5) \\ &= 97 \pm 25 \text{ J/mole.} \end{aligned} \qquad \text{(E8)}$$

Therefore, the total range of values for the energy loss is 72 to 122 J/mole which is within the values used for interface profile matching.

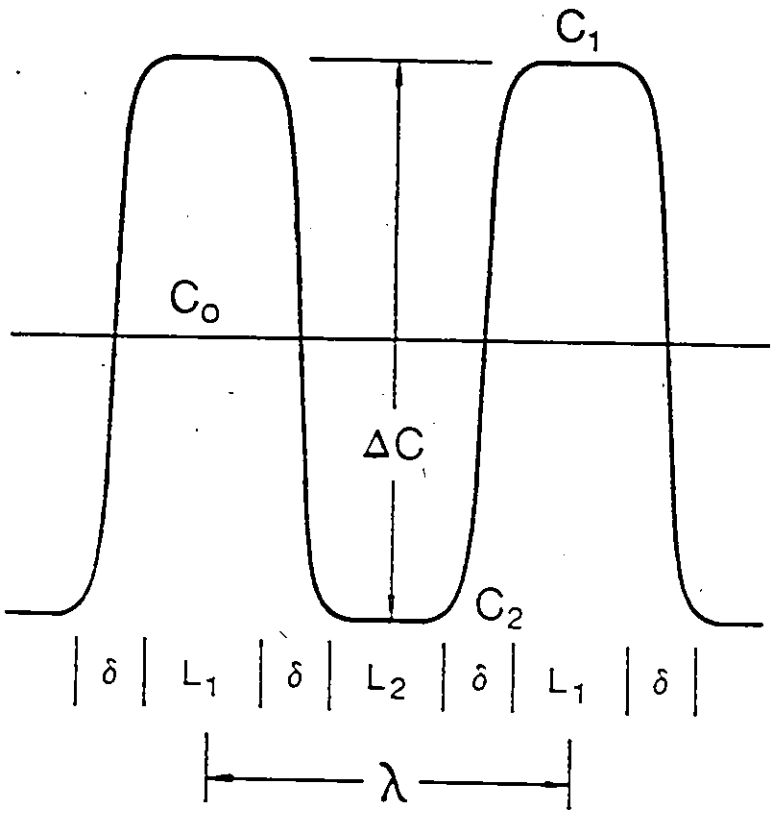

Figure E1 Compositional Profile for a spinodally decomposed alloy.

(Refer to Figure 5.5)

Appendix F

Boundary Diffusion and Migration

For the boundary slab segment as shown in Figure F1, the time dependent diffusion equation is;

$$D_b\delta \frac{\partial^2 C_b}{\partial y^2} - D_v \frac{\partial C_c}{\partial z}\Big|_o - vC_d + vC_c|_o = \frac{\partial C_b}{\partial t} \qquad (F1)$$

Equilibrium between the boundary and the growing grain is assumed and the concentrations are assumed to be proportional according to the relationship;

$$C_b = K\, C_d \qquad (F2)$$

The concentration across the slab is assumed constant and the coherent concentration in the shrinking grain (assuming ideal behavior) is given as;

$$C_c|_o = C_d\,[1 - 2\,C_d\,E\,V_m\,\eta^2/RT(1-\nu)] \qquad (F3)$$

The boundary velocity is assumed to be controlled by a linear force law where the force is a chemical force derived from the coherency strain energy which is reduced by a capillarity term and can be represented as;

$$v = M\,(\Delta G - \gamma\, V_m\, (d\theta/dy)) \qquad (F4)$$

where M is the mobility of the boundary, γ is the surface energy, V_m is the molar volume and $d\theta/dy$ is the boundary curvature. The curvature is estimated as shown in Figure F2, where dd is the difference in length of respective nodes within the boundary. Again assuming ideal solution behavior, the velocity is given as;

$$v = M\,[E\,V_m\,\eta^2 C_d^2/(1-\nu) - \gamma\, V_m(d\theta/dy)] \qquad (F5)$$

Equations F1,F2 and F5 are substituted into F1 to derive the equation

for solution.

Since volume diffusion is prevalent, the time dependent diffusion equation is also required for simultaneous solution. Diffusion in two dimensions is allowed with a velocity term added since the reference frame is moving. The resulting equation is;

$$D_v \frac{\partial^2 C_c}{\partial y^2} + D_v \frac{\partial^2 C_c}{\partial z^2} + v \frac{\partial C_c}{\partial z} = \frac{\partial C_c}{\partial t} \qquad \text{(F6)}$$

The solution is derived by the finite difference method using the appropriate dimensionless parameters substitution. The boundary conditions are as follows,

(1) The boundary node at the surface is maintained at the equilibrium value. ie $C_d/C_{eq} = 1$

(2) The volume surface nodes are maintained at the coherent equilibrium concentration as defined by equation F3.

Steady State Solution

Defining a steady state solution for diffusion into a semi-infinite medium was justified in the text. An analytical solution is possible if the following assumptions are made;

(1) Diffusion in the bulk is only allowed normal to the boundary plane.

(2) Capillarity is neglected.

Under these conditions, the equations for solution become;

$$D_v \frac{\partial^2 C_c}{\partial z^2} + v \frac{\partial C_c}{\partial z} = 0 \qquad \text{(F7)}$$

$$v = M \left[\Sigma V_m n^2 C_d^2 / (1-\nu)\right] \qquad \text{(F8)}$$

$$D_b\delta \frac{\partial^2 C_b}{\partial y^2} - D_v \frac{\partial C_c}{\partial z}_o - vC_d + vC_c|_o = 0 \qquad \text{(F9)}$$

Solution of F7 has the form;

$$C_c(z) = C_c|_o \exp -(vx/D_v) \qquad \text{(F10)}$$

Therefore, the flux from the boundary can be evaluated;

$$D_v(dC_c/dz)_o = -vC_c|_o \qquad \text{(F11)}$$

Substituting F2, F8 and F11 into F9 yields;

$$D_b\delta \frac{\partial^2 C_d}{\partial y^2} - A\, C_d^3 = 0 \qquad \text{(F12)}$$

where;

$$A = (M\ E\ V_m\ \eta^2)/(K\ D_b\delta\ (1-\nu)) \qquad \text{(F13)}$$

employing the substitution;

$$P = (dC_d/dy) \qquad (d^2C_d/dy^2) = P(dP/dC_d) \qquad \text{(F14)}$$

and the conditions;

$$C_d(0) = C_e \qquad (dC_d/dy) < 0 \qquad \text{(F15)}$$

yields the solution as;

$$C_d(y) = [\ A/2\ y + 1/C_e]^{-1} \qquad \text{(F16)}$$

The velocity and the 1% penetration depth Y can be evaluated and are given as;

$$v = \frac{M\ E\ V_m\ \eta^2}{1-\nu}\left[\frac{(M\ E\ V_m\ \eta^2)y^2}{K\ D_b\delta\ (1-\nu)} + \frac{1}{C_e}\right]^{-2} \qquad \text{(F17)}$$

$$Y(0.01) = \frac{99\sqrt{2}\ E\ M\ V_m\ \eta^2}{C_e\ (1-\nu)\ K\ D_b\delta} \qquad \text{(F18)}$$

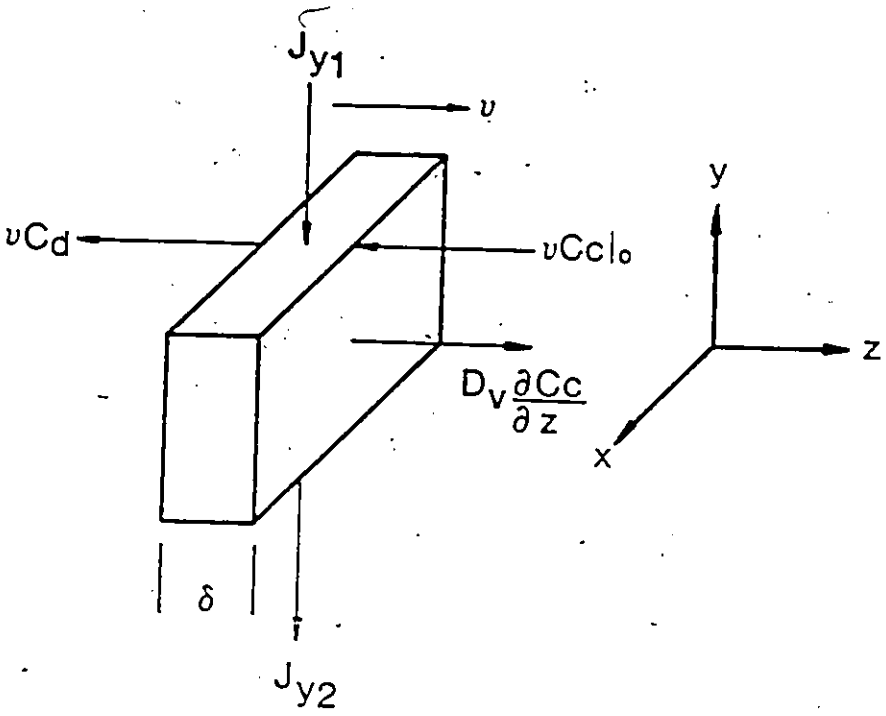

Figure F1 Boundary slab section illustrating solute fluxes and the moving reference frame.

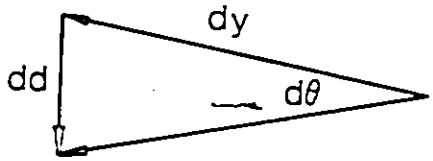

Figure F2 Boundary curvature estimation